creative commons

COMMONS DEED

저작자표시-비영리-변경금지 2.0 대한민국

이용자는 아래의 조건을 따르는 경우에 한하여 자유롭게

- 이 저작물을 복제, 배포, 전송, 전시, 공연 및 방송할 수 있습니다.

다음과 같은 조건을 따라야 합니다:

저작자표시. 귀하는 원저작자를 표시하여야 합니다.

비영리. 귀하는 이 저작물을 영리 목적으로 이용할 수 없습니다.

변경금지. 귀하는 이 저작물을 개작, 변형 또는 가공할 수 없습니다.

- 귀하는, 이 저작물의 재이용이나 배포의 경우, 이 저작물에 적용된 이용허락조건을 명확하게 나타내어야 합니다.
- 저작권자로부터 별도의 허가를 받으면 이러한 조건들은 적용되지 않습니다.

저작권법에 따른 이용자의 권리는 위의 내용에 의하여 영향을 받지 않습니다.

이것은 이용허락규약(Legal Code)을 이해하기 쉽게 요약한 것입니다.

Disclaimer

dCollection

Ph.D. DISSERTATION

Resistive Switching Characteristics of Halide Perovskite Films

Jaeho Choi

August 2018

SEOUL NATIONAL UNIVERSITY

COLLEGE OF ENGINEERING

DEPARTMENT OF MATERIALS SCIENCE AND ENGINEERING

Abstract

With the Information Age, needs for high capacity, high performance storage media has been developed. Also, semiconductor-based storage media have been developed through fine process improvements. However, it has not solved problems, which are a number of critical electrons in the floating gate or capacitor and patterning limitation. To overcome the problems, various next-generation memories have been suggested. Among these, resistive switching (RS) memories are the most promising candidates, which adopt metal oxides as an insulating layer. However, metal oxide-based RS memories have disadvantages, which are high-cost in vacuum fabrication process and poor mechanical flexibility for flexible and wearable devices. Therefore, halide perovskites have received attention to overcome the disadvantages of conventional metal oxide-based RS memories. Halide perovskites, which have received attention as a next-generation semiconductor material, exhibit tunable band gap and control the majority carrier, exhibits high ion mobility and mechanical flexibility.

This thesis presents fabrication of halide perovskite-based RS memories, characterization of electrical properties, and performance enhancement in four chapters. The first chapter focuses on the analysis of resistive switching and conduction characteristics of the most popular halide perovskite, $CH_3NH_3PbI_3$ thin films. The second chapter introduces RS memories with morphologically improved $CH_3NH_3PbI_3$ thin films, which are based on a solution process with hydriodic acid as an additive. With morphology-improved thin films, RS

memories exhibited enhanced endurance and operable low bending radius of 5 mm. While the previous two chapters used $CH_3NH_3PbI_3$ as an insulating layer, the third chapter shows RS memories 2-dimensional BA_2PbI_4 as an insulating layer to improve switching reliability. In the fourth chapter, a fundamental strategy to extend resistive switching performance is provided. A mixture of switchable cubic $CH_3NH_3PbI_3$ and non-switchable orthorhombic $RbPbI_3$ is adopted as an insulating layer of RS memories to control dimension of conducting filaments. Also, PMMA passivation layer is utilized to protect the insulating layer from H_2O and O_2 in ambient atmosphere.

In the first chapter, implement of high-performance halide perovskite memory was introduced. To fabricate uniform $CH_3NH_3PbI_3$ thin films on hydrophobic Pt coated SiO_2/Si wafer, antisolvent dripping is conducted during spin coating for fast and uniform crystallization. Vertical metal-insulator-metal structure device was completed using the electron beam-evaporation of 100 nm-thick Ag, Au, and Ni with a dot patterned shadow mask, respectively. Vertical Ag/$CH_3NH_3PbI_3$/Pt device exhibits ultralow switching voltage, high on/off ratio, 4-multilevel switching, and electro-forming free. However, short endurance of 350 cycles is weakness. With conductive-atomic force microscopy, the $CH_3NH_3PbI_3$ film is conducting regardless of the morphology, suggesting that conducting filaments grow through bulk of grains, not grain boundaries. Based on these results, the first principle calculation was performed to find out the origin of the ultralow E-field resistive switching behavior. As a result, the activation energy of migration for native point defects, iodine vacancies and interstitials, are 4 ~ 10 percent, compared to the activation energy

of oxygen vacancies in the conventional metal oxides. This is related to the Ag/$CH_3NH_3PbI_3$/Pt devices exhibit ultralow switching voltage because the iodine vacancies and interstitials, which have low activation energy for migration, form conducting filaments.

In the second chapter, RS memories with morphologically improved $CH_3NH_3PbI_3$ films are introduced. In the previous study, antisolvent dripping for rapid crystallization of the $CH_3NH_3PbI_3$ films is adopted; however, this method involves a problem, which is a film uniformity deviation according to dissolution and penetration rate of antisolvent to the $CH_3NH_3PbI_3$ films. The $CH_3NH_3PbI_3$ thin film which prepared by the addition of hydriodic acid shows a smaller grain size and reduced uniformity deviation. RS memories with the uniformity-improved $CH_3NH_3PbI_3$ films exhibit enhanced endurance of 1330 cycles. Moreover, the RS memories, fabricated on flexible cyclo-olefin polymer substrate, show equivalent RS performance under low bending radius of 5 mm. To analyze conduction mechanism, current-voltage characteristics are measured under low and high temperature. The RS memories with the uniformity-improved $CH_3NH_3PbI_3$ films reveal the conduction mechanism of Ohmic conduction and thermally assisted hopping in low and high resistance state, respectively.

In the third chapter, switching reliability improved-RS memories are introduced with BA_2PbI_4 as one of the halide perovskites having a 2-dimensional layered structure. $CH_3NH_3PbI_3$, which has 3-dimensional structure, necessarily generates irregular grain boundaries during fabrication processes.

Moreover, the irregular grain boundaries causes the deviation of electrical properties and resistive switching performance. However, RS memories with the two-dimensional layered BA_2PbI_4 films, which are not included grain boundaries, exhibit uniform RS behavior throughout the whole area of the thin film. Also, the crystal structure was stable under continuous external electric field. Particularly noteworthy is that the RS memory with BA_2PbI_4 shows perfect switching reliability during endurance test of 250 cycles. Based on uniform crystal structure and reliable switching performance, RS memories, which are fabricated on a 4-inch wafer, also exhibit equivalent switching performance, compared to the RS memory which is fabricated on a small-size substrate of 1×1 cm^2. Finally, it is possible to operate in high temperature environment of 87 ^oC, showing the possibility of commercialization of next generation memory.

At the last, a fundamental strategy to enhance endurance of RS memories is introduced. A typical degradation process of RS memories is continuous growth and extension of conducting filaments under repeated SET and RESET processes. Finally, it is impossible to rupture the conducting filament with general RESET process. Then, the device is stuck in low resistance state. To prevent the degradation process, mixture of non-switchable orthorhombic $RbPbI_3$ and switchable cubic $CH_3NH_3PbI_3$ is adopted to an insulating layer of RS memories. Since the conducting filaments can't grow through the non-switchable $RbPbI_3$, the dimension of the conducting filaments is controllable by the concentration of $RbPbI_3$ in the insulating layer. Especially, the insulating layer which includes $CH_3NH_3PbI_3$ of 30 wt% and $RbPbI_3$ of 70 wt% exhibit

endurance of 970 cycles. To find out the origin of RS behavior, conductive atomic force microscopy and energy dispersive spectroscopic mapping are conducted to $Rb_{1-x}(CH_3NH_3)_xPbI_3$ films. As a result of energy dispersive spectroscopic mapping with field emission-scanning electron microscopy after applying electric field to the $Rb_{1-x}(CH_3NH_3)_xPbI_3$ films using C-AFM, Ag atoms were prominently detected in the area where electric field was applied. Based on this, the origin of RS behavior is assumed from migration of Ag atoms with external E-field. With the introduced strategies, I expect the advancement of the halide perovskite based RS memories consistently.

Keywords: Halide perovskite, Resistive switching, 2-dimensional and 3-dimensional crystal structure, solution process, flexible memory, resistive switching mechanism, conduction model, conducting filament, the first principle calculation, reliability enhancement

Student Number: 2013-23049

JAEHO CHOI

Table of Contents

Abstract ii
Table of Contents vii
List of Tables ix
List of Figures x
Chapter 1 1
Emergence of Information Age with memory devices 1
1.1. Background 2
1.2. Resistive Switching (RS) memories 7
1.2.1 Introduction to Next-Generation Memories 7
1.2.2 Switching Mechanisms of RS memories 8
1.3. Halide Perovskites 12
1.3.1 Introduction 12
1.3.2 Unique Properties of HPs 14
1.4 References 24
Chapter 2 28
The First High Performance HP-based RS memory. 28
2.1. Introduction 29
2.2. Experimental Procedures 32
2.3. Results and Discussion 35
2.4. Conclusion 55
2.5 References 56
Chapter 3 60
Morphologically enhanced flexible memory 60
3.1. Introduction 61
3.3. Results and Discussion 66
3.5. References 89
Chapter 4 93
Reliable RS memory with 2-dimensional layered HPs 93

4.1. Introduction 94
4.2. Experimental Procedures 98
4.3. Results and Discussion 100
4.5. References 119
Chapter 5 123
A Fundamental Approach for extended RS performance 123
5.1. Introduction 124
5.2. Experimental Procedures 127
5.3. Results and Discussion 129
5.5. References 150
Chapter 6 Summary 155
Acknowledgments 159
List of Publications 161
Curriculum vitae 168

List of Tables

Table 1 Comparison of various characteristics of next generation memories. 8
Table 2 Five $CH_3NH_3PbI_3$ films with different grain sizes by controlling annealing condition. 45
Table 3 Lattice parameters and unit cell volumes of the samples 115

List of Figures

Figure 1 Photographs of Voyager Golden Record. 2
Figure 2 The recent variations in data created or copied annually. The data are from ref. 2. 4
Figure 3 (a) Scaling and technology trend for NAND flash memory.[3] (b) Dependency between device dimension and a number of electrons in floating gate.[4] 5
Figure 4 (a) Schematic and (b) a cross-sectional SEM image of 3D NAND flash memory.[5] 6
Figure 5 Schematic current - voltage characteristics of resistive switching devices.[7] (a) Pt/ZrO_x/Zr valence change memory cell. (b) Ag/Ag-Ge-Se/Pt electrochemical metallization cell..... 10
Figure 6 (a) The first resistive switching device with Al_2O_3.[8] (b) The conventional resistive switching devices with PCMO/SRO and Nb:STO.[9] 11
Figure 7 Various composition of halide perovskites of (a) ABX_4, (b) A_2BX_4,(c) $A_{n+1}B_nX_{4n+1}$, (d) $A_{n+1}B_nX_{3n+1}$, and (e) $A_nB_nX_{3n+1}$. 12
Figure 8 Exotic properties of halide perovskites. Each figure describes tunable bandgap, fast ion migration, facile majority carrier control, and flexibility of halide perovskites, respectively. Reproduced with permission. Copyright 2015, 2016, ACS publications,[21, 14] 2014, AIP publishing LLC,[41] and 2017, Royal Society of Chemistry.[53] 13
Figure 9 A-site molecular rotational motion in a unit cell of $CH_3NH_3PbI_3$. 31
Figure 10 (a) Plane-view and cross-sectional SEM images of a 400 nm-thick $CH_3NH_3PbI_3$ thin film on Pt/Ti/SiO_2/Si substrate. (b) X-ray diffraction pattern of a $CH_3NH_3PbI_3$ film on SiO_2/Si substrate. Red lines are XRD pattern from Ref. 17 35
Figure 11 SEM images of the vertical structure devices. (a-c), Each device has (a) Ag, (b) Ni, (c) Au electrodes. The thickness of $CH_3NH_3PbI_3$ thin film is about 320-400nm. We adopted two types of metals, such as Ag and Ni to the top electrodes to investigate the resistive switching properties. The minimum thickness of the top electrodes is about 50 nm. (d) Schematic of the metal/$CH_3NH_3PbI_3$/metal vertical structure for resistive switching..... 36
Figure 12 Resistive switching properties of Ag/$CH_3NH_3PbI_3$/Pt cells. (a) Typical current-voltage (I-V) characteristic of Ag/$CH_3NH_3PbI_3$/Pt cells.

(b) I-V characteristics of a Ag/$CH_3NH_3PbI_3$/Pt cell from 5 initial voltage sweeps. SET voltage is + 0.15 V and RESET voltage is – 0.15 V. 38
Figure 13 (a) Reversible resistive switching measured with a writing voltage of 0.15 V and a reading voltage of 0.02 V. The pulse width of the writing voltage was 200 ms. (b) High and low resistance states for 50 different cells. The average on/off ratio is calculated to be 1.12 x 10^6.39
Figure 14 Retention characteristics of the Ag/$CH_3NH_3PbI_3$/Pt/SiO_2/Si device. 39
Figure 15 (a) Stoichiometry-dependent X-ray diffraction patterns of a $CH_3NH_3PbI_3$ films by the controlling of the ratio of methylammonium and lead iodide. (Black line-exact stoichiometry, green line-methylammonium iodide rich, blue line-lead iodide rich, red line-Ref 20.). In the blue line, peaks for PbI_2 appear at 12.67, 25.49, 38.59, and 52.33 degrees (Red stars, JCPDS No. 00-007-0235). (b) I-V characteristics of the $CH_3NH_3PbI_3$ thin films are synthesized by the ratio of methylammonium and lead iodide is 1:1. (c) Methylammonium iodide rich and (d) Lead iodide rich. The thickness of the thin films is fixed to 320-350 nm. 40
Figure 16 Dependence of the top electrodes and electrode area. (a) Linear-scale I-V characteristics of the ON (LRS) and OFF states. (b) Dependence of ON and OFF state current levels on the area of Ag top electrodes for Ag/$CH_3NH_3PbI_3$/Pt cells. 41
Figure 17 Dependence of the top electrodes. (a) Ag/$CH_3NH_3PbI_3$/Pt, (b) Ni/$CH_3NH_3PbI_3$/Pt and (c) Au/$CH_3NH_3PbI_3$/Pt cells. The cells adopt (a) Ag, (b) Ni and (c) Au top electrodes show hysteretic I-V curves which are applicable to resistive switching. The cells with Ag top electrodes are switchable in low SET/RESET voltage. With high SET voltage (> 0.25 V), these cells could not be turned off perfectly. The cells adopt Ni and Au top electrodes had relatively higher SET voltages (> 0.3 V)… 42
Figure 18 Scanning probe microscopy images of $CH_3NH_3PbI_3$ thin films. (a) A topological AFM image of the $CH_3NH_3PbI_3$/Ag structure. The scale of bars is 500 nm. The tip moves 3 μm through the blue dotted line to measure the roughness by the distance (down). 43
Figure 19 Scanning probe microscopy images of $CH_3NH_3PbI_3$ thin films. (a), (b) CAFM images of a $CH_3NH_3PbI_3$/Ag structure with platinum coated tip biases of (a) 0.1 V and (b) 1 V. The scale of bars is 500 nm. The tip moves through the blue dotted line to measure the current vs the distance (down). 44
Figure 20 X-ray diffraction patterns and SEM images for $CH_3NH_3PbI_3$ films synthesized using annealing conditions. (a) Sample 1 (100 °C,

40mins, DMF), (b) Sample 2 (100 °C, 40 mins, ambient), (c) Sample 3 (70 °C, 40 mins, ambient), (d) Sample 4 (70 °C, 1 min, ambient), (f) Sample 5 (No heat treatment, ambient). The diffraction peak near 12.6° for PbI_2 (Red star, (a)) is absent. The insets of each XRD pattern are plain-view SEM images of each sample. 46
Figure 21 Number of cycles with ON/OFF ratio over 10^6 from endurance measurements (total 50 number of cycles) for $CH_3NH_3PbI_3$ films with different grain sizes. 47
Figure 22 Comparison with various resistive switching materials. The ON/OFF ratio of resistive switching devices including the $CH_3NH_3PbI_3$–based cells. 48
Figure 23 DFT calculation for native point defects in $CH_3NH_3PbI_3$. (a) Schematic migration paths of $V_I^{\bullet}$ (left) and $I_i^{\prime}$ (right) in the unit cell of $CH_3NH_3PbI_3$. The center of the split interstitial is moved to adjacent I site, and the direction of the split rotates to another [110] direction. (b) DFT calculation about the activation energy for the movements of $V_I^{\bullet}$ and I_i' to the next sites. 49
Figure 24 Schematic of filamentary resistive switching behaviour in Ag/$CH_3NH_3PbI_3$/Pt cells by defect ion migration. (a) Initial state of Ag/$CH_3NH_3PbI_3$/Pt cells with iodine interstitials ($I_i^{\prime}$). (b) Ion migration of iodine interstitials by applying positive electric field (+ 0.15 V). (c) Fully formed conducting filament (ON state). (d, e) Ion migration of iodine interstitials by applying negative electric field (- 0.15 V). (f) Rupture of the conducting filament (OFF state). (g) Corresponding I-V curve. 50
Figure 25 Resistive switching properties of Ag/$CH_3NH_3PbI_3$/Pt cells measured at different temperatures. (a) I-V curves of 20 cells measured at room temperature. (b) The endurance of a cell measured at room temperature. (c) I-V curves of 20 cells measured at 100 K. (d) The endurance of a cell measured at 100 K. (e) I-V curves of 20 cells measured at 150 K. **f**, The endurance of a cell measured at 150 K. 51
Figure 26 Multilevel resistive switching properties. (a) I-V characteristics of Ag/$CH_3NH_3PbI_3$/Pt cells under three different compliance currents (CC=10^{-2} A, 10^{-4} A, 10^{-5} A, 10^{-6} A). (b) Reversible resistive switching over 40 cycles with different current compliances of 10^{-2}, 10^{-4}, 10^{-5}, and 10^{-6} A. The switching pulse duration is fixed to 200 ms, and the switching voltage is ±0.15 V. 52
Figure 27 Dependence of the compliance currents in switching pulses. Switching with various current compliances of (a) 10^{-2} A, (b) 10^{-4} A, (c) 10^{-5} A, and (d) 10^{-6} A. The voltage of the switching pulses is 0.15 V. The

pulse width is fixed to 250 ms. As illustrate in the figure, 10^{-2} A of the current compliance for reversible switching shows the most stable result. When the current compliance of the pulse is under 10^{-6} A, the reversible switching is impossible. With decreasing the current compliance of the switching pulses, a percent, the reversible switching is accurate, is decreasing. It is obvious that the higher current compliance for the reversible switching is applied, the better switching accuracy is performed..... 53
Figure 28 (a), (b) Plane-view SEM images of (a) rough films and (b) smooth $CH_3NH_3PbI_3$ thin films. 66
Figure 29 (a), (b) Cross-sectional SEM images of $CH_3NH_3PbI_3$/Pt/Ti/SiO_2/Si vertical structure with (a) rough films and (b) smooth films 66
Figure 30 X-ray diffraction pattern of a $CH_3NH_3PbI_3$ film on SiO_2/Si substrate. Black lines are XRD pattern of ref. 24. 67
Figure 31 Topological atomic force microscopy images of (a) rough films and (b) smooth films. The scale of bars is 500 nm. The tip moves through the blue and red dotted lines to measure the roughness by the distance (bottom). 68
Figure 32 (a), (b), (c), (d), (e) Plane-view SEM images of $CH_3NH_3PbI_3$ thin film on Pt/Ti/SiO_2/Si substrate. The concentration of hydroiodic acid solution in $CH_3NH_3PbI_3$ solution is (a) 0%, (b) 2%, (c) 4%, (d) 6%, (e) 8%. 70
Figure 33 Cross-sectional SEM image of a fabricated (a) Ag/$MAPbI_3$ (smooth film)/Pt/Ti/SiO_2/Si, (b) Ag/$MAPbI_3$ (rough film)/Pt/Ti/SiO_2/Si, and (c) Au/$MAPbI_3$ (smooth film)/Pt/Ti/SiO_2/Si vertical structure..... 71
Figure 34 (a) Schematic illustration of the resistive switching mechanism of the organolead halide perovskite resistive switching device. (b) Typical current-voltage (I-V) characteristics of Ag/$CH_3NH_3PbI_3$/Pt devices. 72
Figure 35 I-V characteristics of four Ag/$CH_3NH_3PbI_3$/Pt cells from 4 initial voltage sweeps. SET voltage is + 0.3 V and RESET voltage is – 0.3 V. 73
Figure 36 (a) Typical I-V characteristics of Ag/$CH_3NH_3PbI_3$/Pt devices with smooth $CH_3NH_3PbI_3$ thin films. (b) I-V characteristics of Ag/$CH_3NH_3PbI_3$/Pt devices with high voltage (± 1 V) 74
Figure 37 Resistive switching properties of Ag/$CH_3NH_3PbI_3$/Pt devices with rough and smooth $CH_3NH_3PbI_3$ thin films. (a), (b), (c) Reversible resistive switching measured with voltage pulses. 75

Figure 38 (a) Reversible resistive switching measured with SET voltage of + 0.3 V and RESET voltage of – 0.3 V. A reading voltage is + 0.05 V The pulse width of the SET voltage was 50 ms and the RESET voltage was 100 ms. (b) I-V characteristics of Ag/$CH_3NH_3PbI_3$/Pt devices after the device was stuck in low resistance state. 76
Figure 39 Retention characteristics of the Ag/$CH_3NH_3PbI_3$/Pt devices with smooth thin films. 77
Figure 40 I-V characteristics of a Ag/$CH_3NH_3PbI_3$/Pt cell to describe a long term stability. 78
Figure 41 Linear current-voltage (I-V) characteristics of a Ag/$CH_3NH_3PbI_3$/Pt cell in (a) low resistance state, and (b) high resistance state. 79
Figure 42 (a), (b), (c), (d) Typical I-V characteristics of Ag/$CH_3NH_3PbI_3$/Pt devices measured at 223 K, 243 K, 263 K, 283 K, 303 K and 323 K. 81
Figure 43 (a) Typical I-V characteristics of Au/$CH_3NH_3PbI_3$/Pt devices. (b) I-V characteristics of virgin Ag/$CH_3NH_3PbI_3$/Pt cells with negative biases. (c) Current-electric field (I-E) characteristics of a lateral-structure Pt/$CH_3NH_3PbI_3$/Pt device with various scan rates. (d) Linear I-E characteristics of vertical structure Ag/$CH_3NH_3PbI_3$/Pt devices (upper) and lateral structure Pt/$CH_3NH_3PbI_3$/Pt device (bottom). The insets show schematic of the lateral and vertical devices. 82
Figure 44 (a) Current-electric field (I-E) characteristics of a lateral-structure Pt/$CH_3NH_3PbI_3$/Pt device with various scan rates. (b) Linear I-E characteristics of vertical structure Ag/$CH_3NH_3PbI_3$/Pt devices (upper) and lateral structure Pt/$CH_3NH_3PbI_3$/Pt device (bottom). The insets show schematic of the lateral and vertical devices. 84
Figure 45 (a) Photograph of a fabricated organolead halide perovskite resistive switching device on a Pt deposited cyclo-olefin polymer substrate. (b) Photograph showing bended states of device. Bending radii were 5 mm (left) and 7.5 mm (right). (inset: photograph of measuring device with a bent state) 85
Figure 46 Resistive switching performance of flexible device with the smooth $CH_3NH_3PbI_3$ thin film. (a) Typical current-voltage (I-V) characteristics of flexible device with bending stress (a bending radius of 5 mm). Reversible resistive switching measured with SET voltage of + 0.4 V and RESET voltage of – 0.6 V. The pulse widths of the writing voltage were 50 ms (SET) and 100 ms (RESET). Bending radiuses were (b) 7.5 and (c) 5 mm. 86

Figure 47 Comparison of crystalline structures of 2D BA_2PbI_4 and 3D $MAPbI_3$ (BA = $C_4H_9NH_3$ and MA = CH_3NH_3). (a, c) Cross-sectional and (b, d) top view of (a, b) BA_2PbI_4 and (c, d) $MAPbI_3$. 96
Figure 48 (a) Schematic device structure of Ag/$BA_2MA_{n-1}Pb_nI_{3n+1}$/Pt/Ti/SiO_2/Si. (b) SEM images for thin film BA_2PbI_4 on the silicon substrate coated by 100 nm of Pt. 100
Figure 49 Cross-sectional scanning electron microscopy images for (a) BA_2PbI_4, (b) $BA_2MAPb_2I_7$, (c) $BA_2MA_2Pb_3I_{10}$ and (d) $MAPbI_3$. (e) Plane-view scanning electron microscopy image for BA_2PbI_4. The OHP thin films formed on the Pt coated silicon wafer. 101
Figure 50 XRD peaks reveals the perovskite formation in (a) BA_2PbI_4, (b) $BA_2MAPb_2I_7$, (c) $BA_2MA_2Pb_3I_{10}$ and (d) $MAPbI_3$. 102
Figure 51 I-V characteristics of (a) BA_2PbI_4, (b) $BA_2MAPb_2I_7$, (c) $BA_2MA_2Pb_3I_{10}$, (d) $MAPbI_3$. 103
Figure 52 I-V curves for forming process and set process for (a) Ag/BA_2PbI_4/Pt, (b)Ag/BA_2MAPb_2I7/Pt, (c)Ag/$BA_2MA_2Pb_3I_{10}$/Pt. All I-V curves measured at one electrode and showed electroforming-free process. 104
Figure 53 (a) The electric field for SET process was compared, the lowest electric field was observed in BA_2PbI_4. (b) the on/off ratio each material (Reading voltage was 0.02 V). 105
Figure 54 Fitted logarithmic I-V characteristics of (a) BA_2PbI_4, (b) $BA_2MA_1Pb_2I_7$, (c) $BA_2MA_2Pb_3I_{10}$. 106
Figure 55 (a) Energy band diagram and (b) Schottky barrier heights at each metal electrode interface calculated by difference between the Fermi level of $(BA)_2(MA)_{n-1}Pb_nI_{3n+1}$ and work function of metal. 107
Figure 56 Temperature dependent resistance of (a) BA_2PbI_4, (b) $BA_2MA_1Pb_2I_7$, (c) $BA_2MA_2Pb_3I_{10}$. The decreased resistance as temperature increased showed the typical semiconductor property. In insert figure, two distinguish slope was determined from In(I_{off})-1/kT plot. It result as two different dominant conducting mechanism, and highest thermal electronic activation energy was observed in BA_2PbI_4 in range of T>300 K. 108
Figure 57 I-V curve of Au/BA_2PbI_4/Pt device. The electric field was applied from positive sweeping to negative sweeping. 110
Figure 58 Endurance characteristics of Ag/$BA_2MA_{n-1}Pb_nI_{3n+1}$/Pt, (a) BA_2PbI_4, (b) $BA_2MA_1Pb_2I_7$, (c) $BA_2MA_2Pb_3I_{10}$. SET voltage was 0.5 V and RESET voltage was -0.6 V. (The pulse width was 10 ms). Reading voltage was + 0.02 V/- 0.02 V. 111

Figure 59 Retention for LRS of (a)Ag/BA_2PbI_4/Pt, (b) Ag/$BA_2MAPb_2I_7$/Pt and (c) Ag/$BA_2MA_2Pb_3I_{10}$/Pt devices. The measured resistances are 50, 33 and 27 ohm for BA_2PbI_4,$BA_2MAPb_2I_7$, and $BA_2MA_2Pb_3I_{10}$, respectively. 112
Figure 60 XRD patterns of four different samples for (a) BA_2PbI_4 and (b) $MAPbI_3$, where (1) represents the as-prepared perovskite on Pt electrode (Perovskite/Pt), (2) the as-prepared perovskite with Ag electrode (Ag/perovskite/Pt), (3) the sample after 10 cycles of voltage sweeping (bias aged Ag/perovskite/Pt) and (4) a thin film of mixture of AgI and perovskite with 0.8 mmol of AgI with respect to 1 mol of perovskite (mixture perovskite/Pt). The area of Ag was 0.09 cm2 with the thickness of 150 nm. The voltage sweeping cycle was 0.5 V →0 V →-0.5V→0 V. The perovskite phase is marked with orange circles. A indicates metallic Ag, # denotes AgI and S corresponds to peak from silicon wafer.* denotes unknown peak. 114
Figure 61 The unit cell volumes of three different samples mentioned in Figure 56 for (a) BA_2PbI_4, and (b) $MAPbI_3$ calculated by lattice parameters listed in Table 3. 115
Figure 62 Reliable resistive switching properties of Ag/BA_2PbI_4/Pt prepared on a 4 inch wafer. (a) BA_2PbI_4 was spin-coated on a 4 inch wafer, and Ag electrodes were deposited on locations (1) – (5). (b) HRS, (c) LRS, and (d) SET voltage, represented by electric field (E) on (1) – (5). 116
Figure 63 BA_2PbI_4 film deposited on (a) Si wafer and (b) its thickness measured from different part designated in (a). 117
Figure 64 (a) Comparison of I-V characteristics from 5 repeated sweeps at room temperature. (b) Distribution of resistances in HRS and LRS was shown (read at 0.02 V). (c) I-V characteristics measured at 87 ^{o}C. ... 117
Figure 65 Crystal structure of $MAPbI_3$ (a-c, MA=CH_3NH_3) and $RbPbI_3$ (d-f). (a, d) top view, (b, e) 3-dimension view and (c, f) cross-sectional view. 129
Figure 66 X-ray diffraction pattern of the $Rb_{(1-x)}MA_xPbI_3$/Pt substrates. (Orange line - $MAPbI_3$, Red line – $Rb_{0.31}MA_{0.69}PbI_3$, Blue line - $Rb_{0.52}MA_{0.48}PbI_3$, Green line - $Rb_{0.71}MA_{0.29}PbI_3$ and Magenta line - $RbPbI_3$) 131
Figure 67 Cross-sectional view scanning transmission electron microscopy (STEM) image and energy dispersive spectrometer (EDS) mapping of (a) $MAPbI_3$ (b) $Rb_{0.31}MA_{0.69}PbI_3$, (c) $Rb_{0.52}MA_{0.48}PbI_3$, (d) $Rb_{0.71}MA_{0.29}PbI_3$ and (e) $RbPbI_3$ films (White - scanning transmission

electron microscopy dark field image, Yellow - Rb atom and Green- Pb atom by corresponding STEM-EDS) 133
Figure 68 Schematic (left) and optical microscopic image (right) of Ag/PMMA/$Rb_{1-x}MA_xPbI_3$/Pt devices..... 134
Figure 69 Cross-sectional view SEM image of the Ag/PMMA/$Rb_{1-x}MA_xPbI_3$/Pt devices. (a) $MAPbI_3$ (b) $Rb_{0.31}MA_{0.69}PbI_3$, (c) $Rb_{0.52}MA_{0.48}PbI_3$, (d) $Rb_{0.71}MA_{0.29}PbI_3$ and (e) $RbPbI_3$. 135
Figure 70 Plane-view SEM image of (a) $MAPbI_3$ (b) $Rb_{0.31}MA_{0.69}PbI_3$, (c) $Rb_{0.52}MA_{0.48}PbI_3$, (d) $Rb_{0.71}MA_{0.29}PbI_3$ and (e) $RbPbI_3$ films..... 136
Figure 71 Typical current−voltage (I−V) characteristics of Ag/PMMA/$RbPbI_3$ mixed $MAPbI_3$/Pt devices. (a) $MAPbI_3$ and $RbPbI_3$, (b) $Rb_{0.31}MA_{0.69}PbI_3$, (c) $Rb_{0.52}MA_{0.48}PbI_3$, and (d) $Rb_{0.71}MA_{0.29}PbI_3$. 138
Figure 72 Reversible resistive switching behavior measured with the voltage pulses. Pulse width is fixed to 640 μs. (a) $MAPbI_3$, (b) $Rb_{0.31}MA_{0.69}PbI_3$, (c) $Rb_{0.52}MA_{0.48}PbI_3$, and (d) $Rb_{0.71}MA_{0.29}PbI_3$. ... 139
Figure 73 Retention characteristics of the Ag/PMMA/$Rb_{1-x}MA_xPbI_3$/Pt devices. (a) $MAPbI_3$ (b) $Rb_{0.31}MA_{0.69}PbI_3$, (c) $Rb_{0.52}MA_{0.48}PbI_3$, and (d) $Rb_{0.71}MA_{0.29}PbI_3$ 140
Figure 74 Long-term stability of the Ag/PMMA/Rb_1-xMA_xPbI_3/Pt devices. (a) $MAPbI_3$ (b) $Rb_{0.31}MA_{0.69}PbI_3$, (c) $Rb_{0.52}MA_{0.48}PbI_3$, and (d) $Rb_{0.71}MA_{0.29}PbI_3$. 141
Figure 75 Linear I−V characteristics of the Ag/PMMA/$Rb_{1-x}MA_xPbI_3$/Pt devices in low resistance state. 142
Figure 76 Logarithmic I−V characteristics of the Ag/PMMA/$Rb_{1-x}MA_xPbI_3$/Pt devices in (a) low resistance state and (b) high resistance state. 143
Figure 77 The effect of the PMMA layer to prevent chemical reation between Ag top eletrodes and halide perovskite films. (a) PMMA coated, and (b) non-coated $MAPbI_3$ films. 144
Figure 78 Topological atomic force microscopy (AFM) images of the $RbPbI_3$ mixed $MAPbI_3$ films of 10 × 10 μm^2 (left). The roughness is measured by AFM tips moving along the green and red dotted lines by distance (right). 144
Figure 79 Conductive AFM image of the of the $Rb_{1-x}MA_xPbI_3$ films of (a) 10 × 10 μm^2 at bias 0.4 V, (b) 5 × 5 μm^2 (blue are in (a) and (c)) at bias 0.8 V and 10 × 10 μm^2 at bias 0.2 V. The current is measured by AFM tips moving along the green and red dotted lines by distance (bottom). 145

Figure 80 Plane view SEM image and EDS mapping of the $Rb_{0.52}MA_{0.48}PbI_3$ films after CAFM measurement. (SEM image – dark field, yellow – Pb atom, red – I atom, purple – Ag atom and white area is CAFM measurement. 146
Figure 81 Schematic diagram of inhibited growth of Ag bridge with increasing the concentration of $RbPbI_3$ 148

Chapter 1

Emergence of Information Age with memory devices

Quote

Alvin Toffler

"This new civilization brings with it new family styles; changed ways of working, loving, and living; a new economy; new political conflicts; and beyond all this an altered consciousness as well" (1980)

1.1. Background

The human beings has evolved with a record, sharing, and communication. They, human beings, have recorded the present, have shared the record, have communicated through the records, and communicates with the descendants. Furthermore, the human beings have tried to communicate with an unknown civilization in the space through 'Voyager Golden Record – The Sound of Earth' in the twin Voyager 1 and 2 spacecraft (Figure 1).[1] The record, sharing, and communication of human beings have been based on instinctual behavior, such as sexual desire and appetite, not on specific intention. This is the most distinctive part of the human beings from other animal species; moreover, it is a driving force that allowed the human beings to reach the current intellectual level.

Figure 1 Photographs of Voyager Golden Record.

Tracing back to the history of the record, the most primitive form of the record is considered cave painting. The world's oldest cave painting has identified as an artwork in La Pasiega cave, Spain, which have been made 64,000 years ago by Neanderthals. The artwork, which was drawn by red clay, is considered to

an evidence of the symbolic thinking of Neanderthals. In another example, a parietal artwork in the cave of Altamira, which have been drawn around 15,500 years ago, mainly depicted animal hunting. With the artwork in the cave of Altamira, they, ancient human beings, were presumed to communicate with others. Ultimately, it is presumed that they intended to survive through hunting life.

For the advancement in record, sharing, and communications, human beings began to use letters/symbols beyond wall paintings in a cave. The first letter/symbol in the world is presumed to be wedge-shaped cuneiform, which is originated from pictograms in Sumer around the 30th century BC. The Sumerian cuneiform was written on clay tablets made by means of a blunt reed for a stylus. Since then, letters/symbols have evolved and are used today as a perfect way for the record, sharing, and communication. As advancement in languages including characters and symbols, the human beings had thirsted for an effective medium for the record, sharing, and communication. Traditional media, such as stones, bamboo, animal bones or leather, and clay tablets were bulky or heavy and difficult to transport, and were inefficient to record characters and symbols. To overcome the shortcomings of the traditional media, paper was invented. The first paper in the world is papyrus, which is originated from ancient Egypt around 800 B.C.. Additionally, paper is etymological derivation of papyrus. The invention of paper was a revolution in the record, sharing, and communication.

With the advancement of languages and media for the record, sharing, and communication, the civilization of human beings has been consistently developed. In 1980, an American futurist and an associate editor of Fortune magazine, Alvin Toffler published a book, The Third Wave. In the book, The First Wave and the Second Wave are the settled agricultural society and Industrial Age society, respectively. The Third Wave is the post-industrial society, such as Information Age, known as the Computer Age, Digital Age, or New Media Age. The progress of Information Age is i) Library expansion, ii) Information storage, iii) Information transmission, and iv) Computation. These processes have led the society, in which rich information is produced and transmitted in two aspects, quality and quantity. With the progress of Information Age, amount of produced and distributed information has been increased extremely (Figure 2). [2]

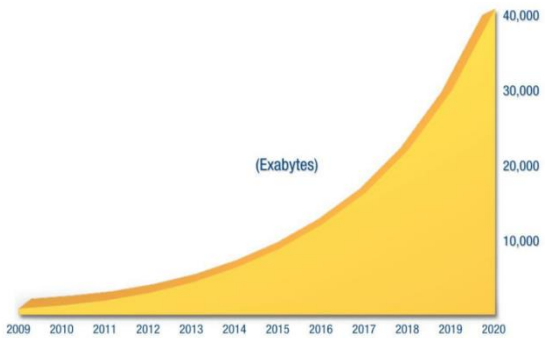

Figure 2 The recent variations in data created or copied annually. The data are from ref. 2.

Even though semiconductor devices have evolved in accordance with Moore's Law and Hwang's Law, the enhancement of semiconductor devices cannot meet the demand, related to the explosion of information production and distribution

by cutting edge trends, which are Internet of Things and Big Data. More and more demands are being made of next-generation devices, particularly in the area of device performance and fabrication, such as increased density, faster data processing, lower power consumption, flexibility, multi-functionality, scalability, cost-effectiveness, and more facile fabrication. However, the developers of conventional silicon-based memory devices have faced scaling problems due to the technology reaching its technical and physical limits. The obstacle of scaling limitation can be divided into two main problems. The first problem is that patterning the channel length of 1x nm is impossible with conventional photolithography technique (Figure 3a).[3] Even if this problem is solved, another problem remains. With down scaling of capacitor in DRAM or floating gate in NAND Flash, a number of charged electrons in the capacitor or floating gate can't be satisfied to a number of critical electrons to memorize data or information (Figure 3b).[4]

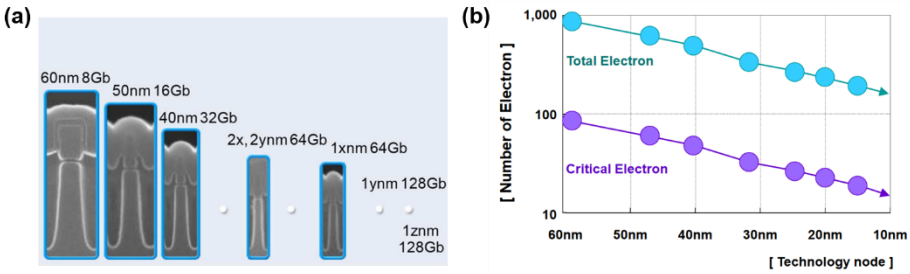

Figure 3 (a) Scaling and technology trend for NAND flash memory.[3] (b) Dependency between device dimension and a number of electrons in floating gate.[4]

Even though 3D stacking structure and high-k dielectric materials are utilized to enhance the capacity and performance, the limitations in down scaling are clear (Figure 4)[5]. Therefore, the next-generation memories have received attention and are actively researched.

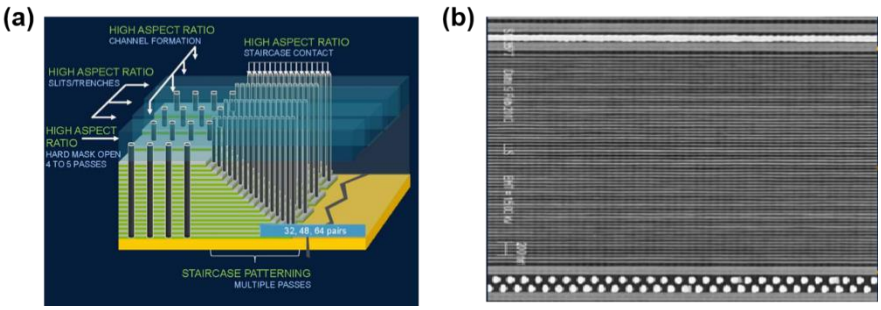

Figure 4 (a) Schematic and (b) a cross-sectional SEM image of 3D NAND flash memory.[5]

1.2. Resistive Switching (RS) memories

1.2.1 Introduction to Next-Generation Memories

Various next-generation memory technologies have been proposed to overcome the scaling limitation of conventional memories. The classification according to the mechanism of storing the data is as follows.

1. Ferroelectric RAM (FeRAM), which adopts a ferroelectric layer instead of a dielectric layer in conventional memory.

2. Magnetoresistive RAM (MRAM and Spin-Transfer Torque MRAM), utilizes an effect in which the orientation of a magnetic layer in a magnetic tunnel junction.

3. Phase-change RAM (PRAM), which is employed in 3D Xpoint memory (Intel), uses a unique behavior of chalcogenide glass which is a transition between amorphous and crystalline state.

4. Resistive RAM (ReRAM) is based on a change of resistance with the formation and rupture of conducting filament.

To compare the performance of the next-generation memories, their performance is summarized in the Table 1.[6]

	Flash	FeRAM	MRAM (STT-MRAM)	PRAM	ReRAM
Writing time	1 ms	10~100 ns	10~50 ns	~20 ns	5 ns
Reading time	100 μs	10~100 ns	10~50 ns	~50 ns	5 ns

Cell size (relative)	1	4.4	4.0	0.9	0.8
Endurance	> 10^5	> 10^{14}	> 10^{16}	> 10^8	> 10^{10}

Table 1 Comparison of various characteristics of next generation memories.[6]

Most of the next-generation memories exhibited enhanced performance than the conventional NAND Flash memory. However, they have a problem which the cell size is rather larger than the conventional flash memory. Scalability is an important factor in the next-generation memory techniques. Basically, these next-generation memories have been proposed technologies to overcome the scaling limitation of the conventional NAND Flash memory. It is difficult to replace the conventional NAND Flash memory without reducing the cell size. Since the ReRAM is the best in terms of performance and scalability, ReRAM has received peculiar attention as a promising candidate of the next-generation memory.

1.2.2 Switching Mechanisms of RS memories

The basic operation concept of resistive-switching memory is analogous to conventional flash memory. When appropriate write voltage pulses are applied to a cell, the cell transitions from a high-resistance state (HRS, equal to unprogrammed in conventional flash memory) to a low-resistance state (LRS, equal to programmed). This is known as the SET process, and the voltage applied for the write operation is the SET voltage. Unlike the SET process, the application of erase voltage pulses leads to the resistance transitioning from LRS to HRS. This is known as the RESET process, in which the applied voltage

is known as the RESET voltage. In addition, most resistive-switching memories have a similar metal-insulator-metal (MIM) sandwich structure. However, redox-based resistive switching behavior can be ascribed to one of two mechanisms, namely, a valence change mechanism (VCM) or electrochemical metallization (ECM).[7] VCM occurs with certain transition metal oxides and involves the migration of anions, which exist in the insulating layer (Figure 5a). This redox reaction leads to a valence change of the cation sublattice. Then, a change in the electronic conductivity in the insulating layer occurs. On the other hand, ECM is slightly different in that it relies on the drift of cations from an electrochemically active electrode (Figure 5b). Typically, ECM memories also have a MIM device structure, although the roles of the electrodes are quite different. The electrodes in VCM memories are independent of the electrochemical activity of the metals. Nevertheless, since ECM is based on the drift of electrochemically active metal cations such as Ag^{+} and Cu^{2+}, one of the two electrodes in an ECM memory device must be electrochemically active. With the application of an external bias or electric field, the drift of the metal cations from the electrochemically active electrode results in the growth and formation of an electrically conductive path (a filament) through an insulating layer.

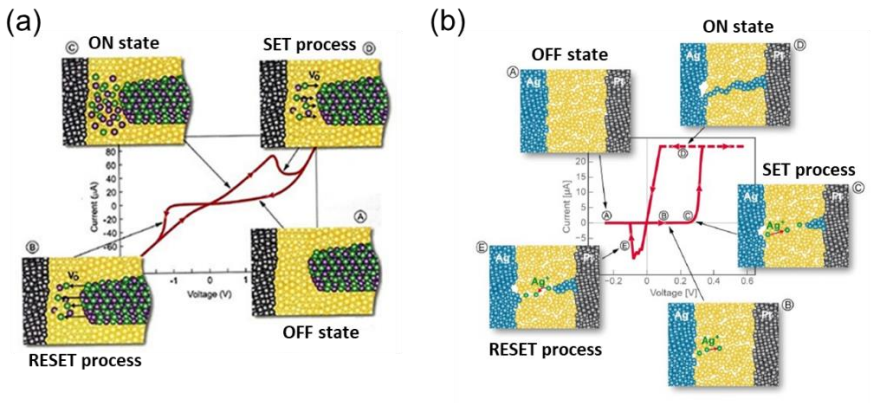

Figure 5 Schematic current - voltage characteristics of resistive switching devices.[7] (a) Pt/ZrO_x/Zr valence change memory cell. (b) Ag/Ag-Ge-Se/Pt electrochemical metallization cell.

As a possible means of overcoming these scaling problems, resistive switching memory based on inorganic materials has been receiving considerable attention. As shown in Figure 6, representative resistive switching devices based on metal oxides, such as Al_2O_3, TiO_2, Ta_2O_{5-x}, $SrTiO_3$, and $Pr_{0.7}Ca_{0.3}MnO_3$, have all been widely studied.[8, 9] Despite continued research into metal-oxide-based resistive switching memories, this technology is subject to shortcomings such as a high power consumption, difficult fabrication, and its unsuitability for flexible/wearable devices.

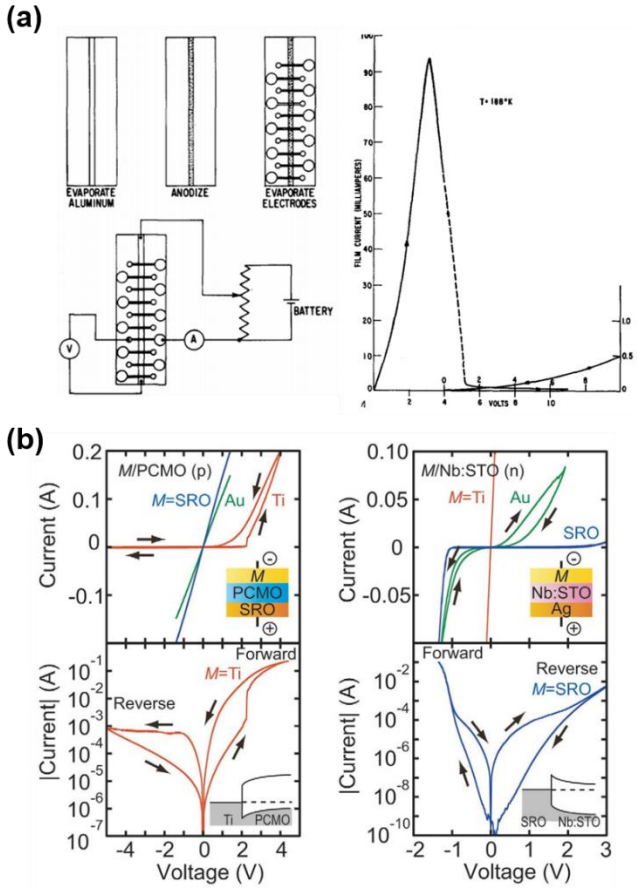

Figure 6 (a) The first resistive switching device with Al_2O_3.[8] (b) The conventional resistive switching devices with PCMO/SRO and Nb:STO.[9]

1.3. Halide Perovskites

1.3.1 Introduction

Halide perovskites (HPs) with the chemical formula ABX_3, ABX_4, A_2BX_4, $A_{n+1}B_n,X_{4n+1}$, and $A_nB_nX_{3n+1}$ consist of a two or three-dimensionally connected network of corner-sharing metal halide octahedral. Representatively, organic cations, such as methylammonium or formamidinium occupy the cubo-octahedral sites, which are each shared by twelve halide anions (Figure 7).

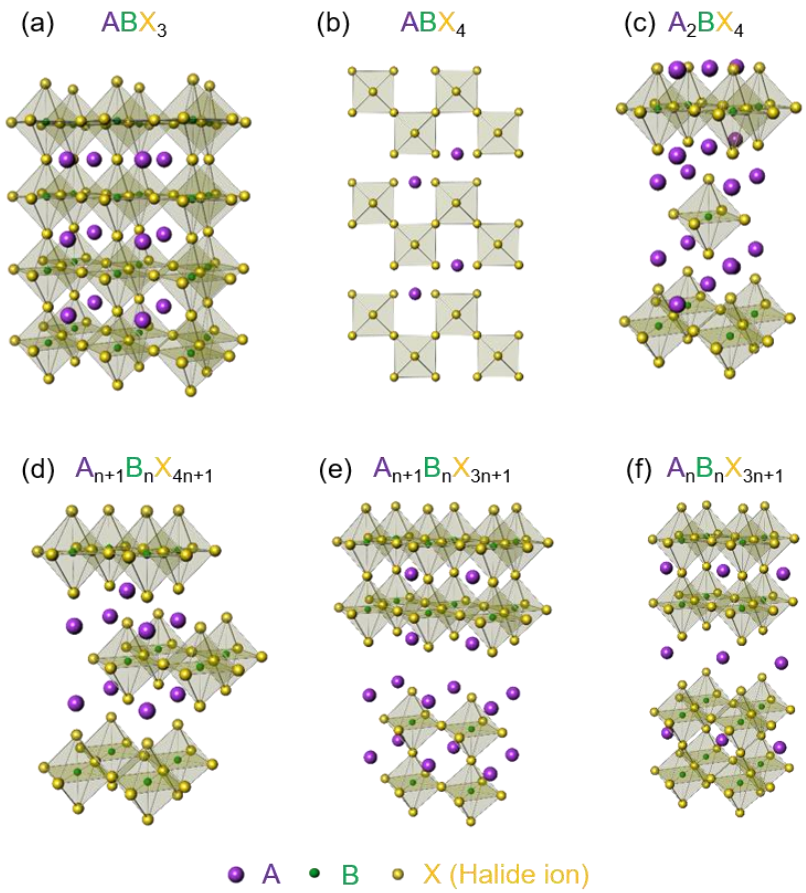

Figure 7 Various composition of halide perovskites of (a) ABX_4, (b) A_2BX_4,(c) $A_{n+1}B_nX_{4n+1}$, (d) $A_{n+1}B_nX_{3n+1}$, and (e) $A_nB_nX_{3n+1}$.

Due to their exotic properties and major advantages in terms of fabrication, HPs are regarded as being a promising candidate for next-generation resistive switching devices. HPs possess exotic properties which have not seen before in other materials: i) a tunable bandgap,[10-12] ii) majority carrier control,[13, 14] iii) fast ion migration,[15-17] and iv) super flexibility[18-20] (Figure 8). The properties of HPs can be adjusted for application to a given device by changing the composition of the HPs through the addition of various substitution elements[12] as well as defect engineering.[13] Current–voltage (*I*–*V*) hysteresis caused by fast ion migration[21], as well as inconsistencies in the forward and reverse scan currents, can be exploited in memristors and artificial synapse devices in which HPs are used for non-optoelectronic applications. The high resilience of HPs to bending deformation originates from their low process temperatures (that are also compatible with flexible substrates) and their constituent elements.

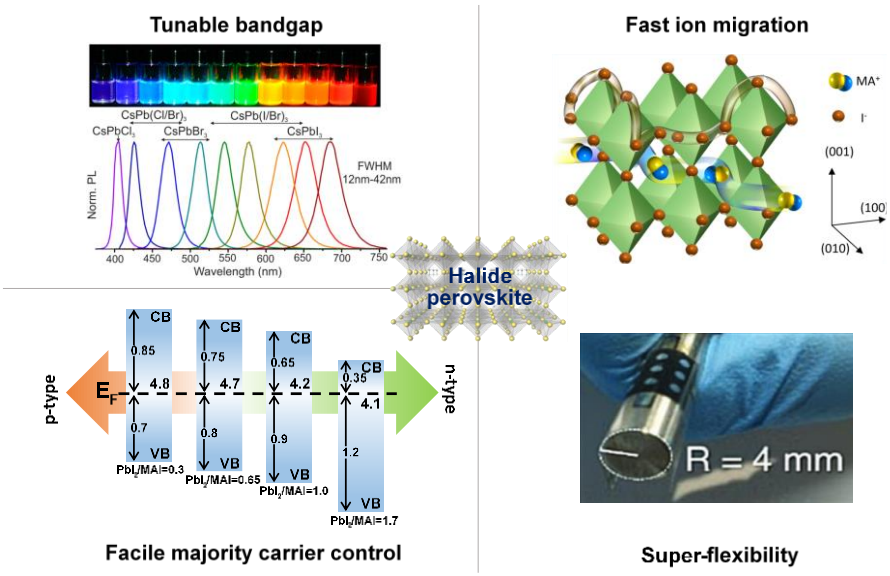

Figure 8 Exotic properties of halide perovskites. Each figure describes tunable bandgap, fast ion migration, facile majority carrier control, and flexibility of

halide perovskites, respectively. Reproduced with permission. Copyright 2015, 2016, ACS publications,[21, 14] 2014, AIP publishing LLC,[41] and 2017, Royal Society of Chemistry.[53]

1.3.2 Unique Properties of HPs

One of the extraordinary properties of HPs is their compositional flexibility, in that HPs can be constituted using various elements. Those HPs with chemical formula ABX3 are mainly composed of a three-dimensional framework of corner-sharing metal halide octahedrals. In the chemical formula ABX_3, where A is an organic cation, B is a metal cation, and X is a halide anion, each A, B, and X site can be substituted by a diverse range of elements. Based on the compositional flexibility of the HPs, the tuning of the bandgap is possible through the substitution of the elements at each site. Moreover, the tuning of the bandgap can be achieved by controlling the crystallite size and the structure of the HPs.

The substitution of the A site cation with other alkylammonium cations is one possible strategy for modifying the bond length between the metal cations in the B site and the halide anions in the C site. In 1990, Calabrese *et al*. reported on layered HPs with $(RNH_3)_2(MeNH_3)_{n-1}Pb_nI_{3n+1}$ and $[Me(CH_2)_8NH_3]_2(MeNH_3)_{n-1}Pb_nBr_{3n+1}$.[22] Due to the length of the alkylammonium cation at the A site, the synthesized HPs exhibited a two-dimensional layered structure, as well as a red shift of the maximum absorption peaks from 390 nm to 450 nm as the length of the A site cation was increased.

Cao *et al*. succeeded in bandgap tuning by changing the layer structure from 2D to 3D by controlling the composition ratio of methylammonium (MA) and butylammonium (BA)[23]. Previous research into 2D HPs had addressed only a complete layered structure. They, however, addressed $(CH_3(CH_2)_3NH_3)_2(CH_3NH_3)_{n-1}Pb_nI_{3n+1}$ while changing n from 1 to 4 and infinity (actually $MAPbI_3$).[24] The bandgap gradually decreased from 2.24 eV to 1.52 eV with a decrease in the value of n. In addition, the conduction and valence bands gradually deteriorated from the vacuum level. The results of calculation-based studies applying density functional theory (DFT) to the 2D and 3D structures of halide perovskites also point to the possibility of applying bandgap tunability according to the A-site cations.[25] Amat *et al*. demonstrated the change in the bandgap of an HP, which can be induced by substituting FA (1.5 eV), MA (1.55 eV), BA (2.24 eV), and Cs (1.73 eV) to the A-site), by DFT calculations.[12]

Another means of bandgap tuning involves the substitution of the metal cation in the B-site to adjust the bonding between the metal cation in the B-site and the halide anion in the C site.[10] Because the band edge of the HPs is determined by the metal cation in the B-site, the substitution of a metal cation provides a means of directly manipulating the valence band maximum and conduction band minimum.[26] For example, Wang *et al*. reported that both tin (Sn) and lead (Pb) can be applied as a substitute at the metal sites.[27] Due to the change of the metal cation at B-site, the bandgap of $MASnI_3$ (1.17 eV) is smaller than that of $MAPbI_3$ (1.55 eV).[28]

Moreover, the calculated bandgaps of $MAPbI_3$ and $MASnI_3$ were reported. The DFT calculation slightly underestimates the bandgap of the HPs even though the DFT calculation produces reliable structure and stability values. The GW calculation provides a precise estimation of the bandgap of the HPs.[29] The calculation produced bandgap values of 1.67 eV ($MAPbI_3$) and 1.10 eV ($MASnI_3$) which are very close to the experimental values.

In the case of the C sites, the substitution of halide elements such as Cl, Br, and I was approached mainly by adjusting the ratio of the halide elements.[30, 31] In addition to the DFT calculation, HP films were fabricated to observe the color change.[32] As the bandgap of the HP film was increased, the color of the film changed from black in the case of $MAPbI_3$ (1.5 eV) to yellow for $MAPbBr_3$ (2.2 eV).[33, 34]

As other strategies, bond angle control related to the cation steric size, structural distortion, and halogen–hydrogen bonding at the organic-inorganic interface, have also been reported as a means of engineering the bandgaps of HPs.[35-38] Using these methods, the optical bandgap of the HPs could be continuously controlled from the mid-infrared to the visible range.

The above approach involved altering the composition of the perovskite to control the bandgap. However, the bandgap can also be tuned by controlling the crystallite size of the thin film.[11] The time-resolved PL was measured after preparing samples with $MAPbI_3$ crystallite sizes from 200 nm to 4000 nm. As a result, the PL spectral position increased from 760 nm to 780 nm, respectively. It is also assumed that the bandgap decreases slightly.

To control the carrier concentration of general silicon-based semiconductors, several complex processes are employed to activate the carriers, including ion showers, implantation, and thermal activation. In this case, a doped extrinsic semiconductor does not adopt an n- or p-type electric property according to the concentration of the dopants (impurities). However, the doping technique applied to HPs is slightly different. One of the most interesting characteristics of HP is that the type of the majority carrier is determined by the cations and their point defects at the A- and B-sites.[13] For example, the defect formation energy of $MAPbI_3$, as obtained by DFT calculation, revealed that the dominant native defects are V_{Pb} and MA_i, given that both defect species have the lowest defect formation energies (0.29 eV and 0.20 eV, respectively). Since the defect species that form deep-level traps, such as I_{Pb}, I_{MA}, Pb_i, and Pb_I, have high formation energies (1.53 eV, 1.96 eV, 1.85 eV and 1.97 eV, respectively), this prevents the formation of these deep-level traps. Schottky defects, such as MAI and PbI_2, are also prevented from forming any traps in the bandgap. However, the formation of elemental defects, which are derived from Frenkel defects such as Pb, I, and MA vacancies, is possible.[39] The results of the DFT calculations revealed that the semiconducting type of $MAPbI_3$ is determined by the concentrations of p-type V_{Pb} and n-type MA_i, both of which have low defect-formation energies. However, only p-type doping is allowed for $MAPbBr_3$.[40] Since the lattice parameter of $MAPbBr_3$ is smaller than that of $MAPbI_3$, the formation energy of MA_i is high, such that the MA_i acts as an n-type dopant. Therefore, $MAPbBr_3$ only forms shallow traps near the valence band.

Manipulating the defect concentration of the HP in the synthesis process is also accomplished by adjusting the mixing ratios of the organic and inorganic precursors.[41] Both n-type and p-type doping are possible in the HPs. In practical experiments, the Fermi level was found to change according to the concentration of the MA cations used for defect engineering. The methylammonium iodide (MAI) concentration, which was volatile at high temperatures (> 100 ˚C), was adjusted by thermal annealing of the $MAPbI_3$ films. The change in the Fermi level of the $MAPbI_3$ films was demonstrated by Hall effect measurements and X-ray photoemission spectroscopy/ultraviolet photoelectron spectroscopy (XPS/UPS) measurements. As the ratio of the PbI_2/MAI increased as a result of the thermal annealing, the $MAPbI_3$ films were converted from p-type to heavily n-type, while the bandgaps of the $MAPbI_3$ films were maintained during thermal annealing.[14]

Another means of controlling the majority carrier concentration involves utilizing the drift of native point defects, which have low formation energies in MAPbI3. Due to the inherent properties of the HPs, charge defects or ions easily migrate under the influence of external biases. In a device with a metal-$MAPbI_3$-metal structure, the drift of the charged $V_I^{\bullet}$, $V_{Pb}^{'}$, and $V_{MA}^{'}$, close to the contacts, causes band bending and the formation of a p-i-n or n-i-p structure, which is temporarily induced by applying an electric field.[42]

Previous research, related to the modulation of the electric properties of silicon-based semiconductors, has established a means of controlling the majority carrier concentration by adding dopants (impurities). Since the

approaches involving doping and synthesis in HPs differ from those for silicon-based semiconductors, further studies are required to determine suitable doping techniques for HPs.

Recently, ion migration in HP has been intensively investigated in terms of the photocurrent hysteresis.[43] The polarity of solar cells can be switched under external bias regardless of the device configuration, type of HP material, and electrode materials[15]. This indicates that ion migration is a general and intrinsic property of HPs. Ion migration occurs easily and quickly in HPs due to the low formation energy of the defective ion species and low activation energy required for ion migration.[17,44] Several elements can contribute to ion migration, including constituent ions such as I^-, Pb^{2+}, and MA^+ in $MAPbI_3$, defects such as vacancies, interstitials, and antisites, and other species such as the H^+ induced by material decomposition or contamination.[15, 17, 44, 45] Even though ion migration in HPs has a detrimental effect on the photo-conversion efficiency, HPs exhibit excellent physical and chemical properties which originate from the fast ion migration, such as current−voltage (*I*–*V*) hysteresis,[21, 48] a switchable photovoltaic effect,[42] giant dielectric constant,[47] photo-induced phase separation,[48] and a photo-induced self-poling effect.[15, 49] These numerous phenomena are very interesting and point to the wide range of possibilities of the HP-based electronic devices.

The constitutent ions in HP can contribute to ion migration through schottky defects given their low activation energy (E_A) for migration.[15] The E_A of ion migration indicates how easily ions move in a solid material. In $MAPbI_3$, I^- ions

are the most mobile ions due to their being closer to the neighboring I^- vacancies (around 4.46 Å) than either the MA^+ or Pb^{2+} ions (around 6.28 Å).[17] Several first-principle calculations on E_A for $MAPbI_3$ have been reported allowing a comparison of the E_A values required for the migration of I^-, Pb^{2+}, and MA^+ ions in $MAPbI_3$.[44, 50] Although there are subtle differences in the E_A values, all the results showed that the I^- ions are more mobile than either the MA^+ and Pb^{2+} ions due to the smallest E_A values of the I^- ions. Eames *et al*. demonstrated the calculated E_A values for I^-, Pb^{2+}, and MA^+ ions in $MAPbI_3$.[17] They showed that the I^- ions had the lowest E_A values of 0.58 eV, which are migrating along the iodine edges of the PbI_6 octahedron. MA^+ and Pb^{2+} ions had E_A values of 0.84 eV and 2.31 eV, respectively.

The high ionicity of HP can be caused by unsual defect property. The defects, such as vacancies, interstitials, and antisites, are mobile species which can participate in ion migration under external bias. There are no significant differences in the calculation of the formation energies of the interstitial defects and the activation energies required for ion migration for the I^- (0.23-0.83 eV, 0.58 eV) and MA^+ ions (0.20-0.93 eV, 0.84 eV).[13] Thus, the ion migration through Frenkel defects should be considered. Additional species, such as H^+ ions, can also affect ion migration through Frenkel defects, given that they are the smallest in size. Low E_A value of H^+ ion migration along a transient hydrogen bond between two equatorial iodides was calculated about to be 0.29 eV.[45]

The rotation of organic cation sites may contribute to the *I*–*V* hysteresis caused by ion migration. The electric polarization can be tuned by modifying the organic cations. The relationship between the rotation of organic cation sites and ferroelectricity under electric field was analyzed according to the organic cation sites (NH^{4+}, MA, FA) through DFT calculations.[51] In the relaxed state, the organic cation is tilted through 30˚ in the lattice and can be aligned under external bias. The rotation of the organic cation sites can occur easily with a low required energy of about 0.37 eV.[52]

As HPs are good ionic conductors, they can exhibit fast ion migration. Various factors, such as constitution ions, defects, and cation rotation, can affect the ion migration. This fast ion migration, which is suppressed in solar cells, enable the application of the material to memristors and artificial synapse devices beyond optoelectronics.

As wearable devices are set to become a major electronics platform, there is an increasing demand for flexibility as a required material property. Moreover, it must be possible to synthesize the active materials of flexible devices at low temperatures, since polymer substrates, which are commonly used in flexible devices, cannot withstand high-temperature processes. HPs offer a significant advantage in this respect. The mechanical flexibility of the material itself and the low temperature of the process together enable the application of the material to flexible devices.

Typical HPs such as $MAPbI_3$ have mechanically organic characteristics due to their organic cation elements which have weak interactions between organic

elements. Moreover, the annealing temperature of HPs usually does not exceed 150 ˚C. Therefore, a highly flexible polymer substrate with a lower process temperature than metal foil or thin flexible glass can be used for the HP-based flexible devices.

There have been many studies involving repeated bending test on the HP-based solar cells and memory devices, exhibiting the outstanding mechanical flexibility of the materials. By Yoon *et al*., high-efficiency HP-based solar cells were demonstrated to have excellent electrical reliability and mechanical stability against bending test.[53] By using graphene as the conducting anode instead of indium-tin-oxide, the devices exhibited an extremely stable electrical reliability that over 85% of initial efficiency was maintained even after 5000 bending cycles with a bending radius of 2 mm. In addition, no significant cracks or variations in the sheet resistance were observed with the graphene-based solar cells during the bending tests. For other electronic devices, Gu *et al*. reported on a flexible HP-based resistive switching memory devices, formed on a plastic substrate.[54] The electrical properties of the memory devices were maintained over 100 bending cycles with a bending radius of 1.5 cm. Thus, excellent mechanical stability as well as electrical reliability can also be seen in a HP-based memory devices.

Super-flexibility can be realized in HP-based electronic devices, which is impossible with conventional semiconductors. Mechanical flexibility and low-temprerature process of the HPs allow various types of substrates including polymer, mainly used for flexible devices. Recently, HP-based electronic

devices, solar cells and resistive switching memory devices, were demonstrated with excellent mechanical stability as well as electrical reliability. Thus, HP-based electronic devices are expected to be applied to many flexible and wearable devices in the near future.

1.4 References

1. Jet Propulsion Laboratory, NASA, https://voyager.jpl.nasa.gov/golden-record
2. J. Gantz, D. Reinsel, The Digital Universe In 2020: Big Data, Bigger Digital Shadows, and Biggest Growth in the Far East, http://www.emc.com/collateral/analyst-reports/idc-the-digital-universe-in-2020.pdf
3. K.-T. Park et. al. *J. Solid-State Circuits* **2015**, 50, 204.
4. S. W. Park, Prospect for New Memory Technology, 2012 Flash Memory Summit, https://www.flashmemorysummit.com/English/Collaterals/Proceedings/2012/20120821_Keynote2_Park.pdf
5. S. Ver-Bruggen, 3D NAND: To 10nm and beyond, 2014 Semiconductor Manufacturing and Design, http://semimd.com/blog/tag/3d-dram/
6. International Technology Roadmap for Semiconductors(ITRS), KIPO, KISTI, ITRS, IEDM.
7. Waser, R., Nanoelectronics and Information Technology : Advanced Electronic Materials and Novel Devices. 3rd ed. *Wiley-VCH: Weinheim*, **2012**, 696-700 .
8. T. W. Hickmott, *J. Appl. Phys.* **1962**, 33, 2669.
9. A. Sawa, *Mater. Today.* **2008**, 11, 28-36.
10. A. Walsh, *J. Phys. Chem. C* **2015**, 119, 5755.
11. V. D'Innocenzo, A. R. Srimath Kandada, M. De Bastiani, M. Gandini, A. Petrozza, *J. Am. Chem. Soc.* **2014**, 136, 17730.
12. A. Amat, E. Mosconi, E. Ronca, C. Quarti, P. Umari, M. K. Nazeeruddin, M. Gratzel, F. De Angelis, *Nano. Lett.* **2014**, 14, 3608.
13. W.-J. Yin, T. Shi, Y. Yan, *Appl. Phys. Lett.* **2014**, 104, 063903.
14. C. Bi, Y. Shao, Y. Yuan, Z. Xiao, C. Wang, Y. Gao, J. Huang, *J. Mater. Chem. A* **2014**, 2, 18508.
15. Y. Yuan, J. Huang, *Acc. Chem. Res.* **2016**, 49, 286.
16. A. M. Leguy, J. M. Frost, A. P. McMahon, V. G. Sakai, W. Kochelmann, C. Law, X. Li, F. Foglia, A. Walsh, B. C. O'regan, *Nat. Commun.* **2015**, 6, 7124.

17. C. Eames, J. M. Frost, P. R. Barnes, B. C. O'Regan, A. Walsh, M. S. Islam, *Nat. Commun.* **2015**, 6, 7497.

18. P. Docampo, J. M. Ball, M. Darwich, G. E. Eperon, H. J. Snaith, *Nat. Commun.* **2013**, 4, 2761.

19. J. You, Z. Hong, Y. M. Yang, Q. Chen, M. Cai, T.-B. Song, C.-C. Chen, S. Lu, Y. Liu, H. Zhou, *ACS Nano* **2014**, 8, 1674.

20. B. J. Kim, D. H. Kim, Y.-Y. Lee, H.-W. Shin, G. S. Han, J. S. Hong, K. Mahmood, T. K. Ahn, Y.-C. Joo, K. S. Hong, N.-G. Park, S. Lee, H. S. Jung, *Energy Environ. Sci.* **2015**, 8, 916.

21. H. J. Snaith, A. Abate, J. M. Ball, G. E. Eperon, T. Leijtens, N. K. Noel, S. D. Stranks, J. T. Wang, K. Wojciechowski, W. Zhang, *J. Phys. Chem. Lett.* **2014**, 5, 1511.

22. J. Calabrese, N. Jones, R. Harlow, N. Herron, D. Thorn, Y. Wang, *J. Am. Chem. Soc.* **1991**, 113, 2328.

23. D. H. Cao, C. C. Stoumpos, O. K. Farha, J. T. Hupp, M. G. Kanatzidis, *J. Am. Chem. Soc.* **2015**, 137, 7843.

24. C. C. Stoumpos, D. H. Cao, D. J. Clark, J. Young, J. M. Rondinelli, J. I. Jang, J. T. Hupp, M. G. Kanatzidis, *Chem. Mater*. **2016**, 28, 2852.

25. T. Umebayashi, K. Asai, T. Kondo, A. Nakao, *Phys. Rev. B* **2003**, 67, 155405.

26. F. Hao, C. C. Stoumpos, R. P. Chang, M. G. Kanatzidis, *J. Am. Chem. Soc.* **2014**, 136, 8094.

27. S. Wang, D. B. Mitzi, C. A. Feild, A. Guloy, *J. Am. Chem. Soc.* **1995**, 117, 5297.

28. C. C. Stoumpos, C. D. Malliakas, M. G. Kanatzidis, *Inorg. Chem.* **2013**, 52, 9019.

29. P. Umari, E. Mosconi, F. De Angelis, *Sci. Rep.* **2014**, 4, 4467.

30. D. M. Jang, K. Park, D. H. Kim, J. Park, F. Shojaei, H. S. Kang, J. P. Ahn, J. W. Lee, J. K. Song, *Nano Lett.* **2015**, 15, 5191.

31. E. Mosconi, A. Amat, M. K. Nazeeruddin, M. Grätzel, F. De Angelis, *J. Phys. Chem. C* **2013**, 117, 13902.

32. J. Even, L. Pedesseau, J.-M. Jancu, C. Katan, *J. Phys. Chem. Lett.* **2013**, 4, 2999.

33. J. H. Noh, S. H. Im, J. H. Heo, T. N. Mandal, S. I. Seok, *Nano. Lett.* **2013**, 13, 1764.

34. S. A. Kulkarni, T. Baikie, P. P. Boix, N. Yantara, N. Mathews, S. Mhaisalkar, *J. Mater. Chem. A.* **2014**, 2, 9221.

35. M. R. Filip, G. E. Eperon, H. J. Snaith, F. Giustino, *Nat. Commun.* **2014**, 5, 5757.

36. J. L. Knutson, J. D. Martin, D. B. Mitzi, *Inorg. Chem.* **2005**, 44, 4699.

37. S. Sourisseau, N. Louvain, W. Bi, N. Mercier, D. Rondeau, F. Boucher, J.-Y. Buzaré, C. Legein, *Chem. Mater.* **2007**, 19, 600.

38. N. Mercier, S. Poiroux, A. Riou, P. Batail, *Inorg. Chem.* **2004**, 43, 8361.

39. J. Kim, S. H. Lee, J. H. Lee, K. H. Hong, *J. Phys. Chem. Lett.* **2014**, 5, 1312.

40. T. Shi, W.-J. Yin, F. Hong, K. Zhu, Y. Yan, *Appl. Phys. Lett.* **2015**, 106, 103902.

41. Q. Wang, Y. Shao, H. Xie, L. Lyu, X. Liu, Y. Gao, J. Huang, *Appl. Phys. Lett.* **2014**, 105, 163508.

42. Z. Xiao, Y. Yuan, Y. Shao, Q. Wang, Q. Dong, C. Bi, P. Sharma, A. Gruverman, J. Huang, *Nat. Mater.* **2015**, 14, 193.

43. Y. Shao, Z. Xiao, C. Bi, Y. Yuan, J. Huang, *Nat. Commun.* **2014**, 5, 5784.

44. J. Haruyama, K. Sodeyama, L. Han, Y. Tateyama, *J. Am. Chem. Soc.* **2015**, 137, 10048.

45. D. A. Egger, L. Kronik, A. M. Rappe, *Angew. Chem. Int. Ed.* **2015**, 54, 12437.

46. E. L. Unger, E. T. Hoke, C. D. Bailie, W. H. Nguyen, A. R. Bowring, T. Heumüller, M. G. Christoforo, M. D. McGehee, *Energy Environ. Sci.* **2014**, 7, 3690.

47. E. J. Juarez-Perez, R. S. Sanchez, L. Badia, G. Garcia-Belmonte, Y. S. Kang, I. Mora-Sero, J. Bisquert, *J. Phys. Chem. Lett.* **2014**, 5, 2390.

48. C. G. Bischak, C. L. Hetherington, H. Wu, S. Aloni, D. F. Ogletree, D. T. Limmer, N. S. Ginsberg, *Nano Lett.* **2017**, 17, 1028.

49. W. Zhang, V. M. Burlakov, D. J. Graham, T. Leijtens, A. Osherov, V. Bulović, H. J. Snaith, D. S. Ginger, S. D. Stranks, *Nat. Commun.* **2016**, 7, 11683.

50. J. M. Azpiroz, E. Mosconi, J. Bisquert, F. De Angelis, *Energy Environ. Sci.* **2015**, 8, 2118.

51. J. M. Frost, K. T. Butler, F. Brivio, C. H. Hendon, M. Van Schilfgaarde, A. Walsh, *Nano. Lett.* **2014**, 14, 2584.

52. R. Gottesman, E. Haltzi, L. Gouda, S. Tirosh, Y. Bouhadana, A. Zaban, E. Mosconi, F. De Angelis, *J. Phys. Chem. Lett.* **2014**, 5, 2662.

53. J. Yoon, H. Sung, G. Lee, W. Cho, N. Ahn, H. S. Jung, M. Choi, *Energy Environ. Sci.* **2017**, 10, 337.

54. C. Gu, J. S. Lee, *ACS Nano* **2016**, 10, 5413.

Chapter 2

The First High Performance HP-based RS memory

Quote

Aristotle "Everything that is in motion must be moved by something.”

2.1. Introduction

Organolead halide perovskites (OHPs) with the chemical formula ABX_3 consist of a three-dimensionally connected network of corner-sharing lead halide octahedral. Organic cations, such as methylammonium or formamidinium occupy the cubo-octahedral sites, which are each shared by twelve halide anions. Due to their inherent hybrid structure, OHPs show unusual electrical and optical properties such as high light absorption and structural and compositional flexibility[1-4]. Mixed ionic–electronic conduction behavior is found in OHPs, suggesting ion migration plays a role in devices based on the materials. Methylammonium lead iodide ($CH_3NH_3PbI_3$) has received attention as a light absorber[5-7] and charge transport[8,9] material for solar cells. Its superior properties, such as a large light absorption coefficient, a small exciton binding energy[10] and a balanced long-range charge diffusion length[11] make the material ideal for photovoltaic applications.

Here, we report an ultralow electric field and high ON/OFF ratio resistive switching behavior of solution-processed OHP films, which is exploited for multilevel data storage. Ag/$CH_3NH_3PbI_3$/Pt cells exhibit electroforming-free resistive switching at an electric field of 3.25×10^3 V/cm for distinguishable four ON-state resistance levels. Density functional theory calculations show that the migration of iodine interstitials and vacancies with low activation energies is responsible for the low electric field resistive switching via filament formation and annihilation.

One of the interesting phenomena that inspired this study is the hysteretic current-voltage characteristics exhibited by $CH_3NH_3PbI_3$ due to the build-up of space charges close to the contacts originating from ionic displacement.[12,13] Xiao *et al.*[12] showed that photocurrent direction in $CH_3NH_3PbI_3$ films could be switched repeatedly by applying a small electric field of < 1 V/μm, which was explained by the formation of reversible *p–i–n* structures induced by ion drift in the perovskite layer. Although the exact defect nature is still elusive, recent studies have shown that negatively charged Pb and CH_3NH_3 vacancies and positively charged I vacancies are the predominant ionic species.[14, 15] More excitingly, the rotational motion of the A-site organic cation can provide structural flexibility and even ferroelectric behavior on the nanoscale.[16, 17] Figure 9 depicts the rotational motion of the CH_3NH_3 cation in the unit cell of $CH_3NH_3PbI_3$. Unlike the spherical Pb cation and I anion, the MA cation is asymmetric dumbbell-shaped. At the ground state, the CH_3NH_3 cation tilts toward the diagonal direction by ~30°.[17,18] Since the molecule is polar, the CH_3NH_3 cation may rotate with an external electric field. Especially, when the external electric filed is applied along the c-axis, the CH_3NH_3 cation can rotate and align with the external bias. For the room temperature cubic phase of $CH_3NH_3PbI_3$, the fast rotational dynamics of the CH_3NH_3 cations in picosecond time scale was predicted.[19, 20] Such a molecular rotational motion can lead to lowering the barrier for the migration of point defects including vacancies and interstitials. This unique nature of $CH_3NH_3PbI_3$ motivated us to explore whether the OHP can be used as a resistive switching material, where the

electrochemical motion of the charged ions and/or the structural phase transition play a role.[21-25]

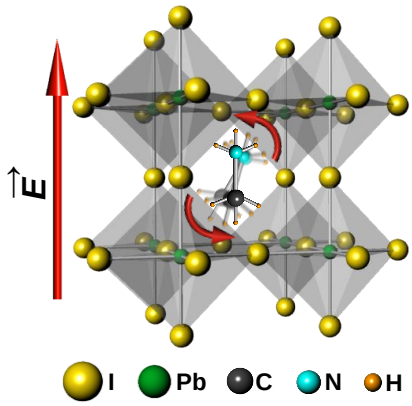

Figure 9 A-site molecular rotational motion in a unit cell of $CH_3NH_3PbI_3$.

In this chapter, I report extraordinary resistive switching behavior of organic-inorganic hybrid perovskite thin films under extremely low electric fields. Typical *I–V* characteristics of solution-processed 400-nm-thick $CH_3NH_3PbI_3$ thin films sandwiched with Ag top and Pt bottom electrodes exhibit resistive switching with ON/OFF ratio more greater than 10^6 and SET voltages below 0.15 V, leading to demonstrating four-level resistance states for multilevel data storage. We performed first-principles calculations to describe that the ultralow electric field bipolar resistive switching properties of the $CH_3NH_3PbI_3$ thin films.

2.2. Experimental Procedures

Materials preparation: Methylammonium iodide (CH_3NH_3I) was prepared by reacting methylamine (7.46 mL, 40% in methanol, TCI) and hydriodic acid (10 mL, 55% in water, ACROS ORGANICS). Reacting solution was stirred at 0℃ for 2h. The solvent was removed by rotary evaporation at 50℃ for 1h. The precipitate (CH_3NH_3I) was dissolved in ethanol and mixing diethyl ether (Daejung Chemicals) for recrystallization. This recrystallization process was repeated twice. After recrystallization, product (CH_3NH_3I) dried in vacuum oven at 60℃ for 24 h.

Film Formation and MIM cell fabrication: Pt/Ti-coated substrates were prepared by electron beam evaporation. Firstly, a 20-nm-thick Ti thin film was deposited on SiO_2 substrates using e-beam evaporator for the better adhesion of the Pt layer and a 50-nm-thick Pt thin film was sequently deposited on the substrates. The Pt-coated substrates were washed by acetone, isopropanol, deionized water under ultrasonication and then treated by air plasma cleaner for 5 min just prior to the synthesis of $CH_3NH_3PbI_3$ films on the substrates. $CH_3NH_3PbI_3$ films were synthesized on Pt/Ti/SiO_2/Si substrates. The perovskite precursor solution was prepared by mixing methylammonium iodide (MAI) powders and PbI_2 in various molar ratios (MAI/ PbI_2 ratios from 0.9 to 1.1) in anhydrous N,N-dimethylformamide (DMF) for overall concentration of 40 wt%. To deposit $CH_3NH_3PbI_3$ perovskite film, the resulting solution was spin-coated on Pt/Ti/SiO_2/Si and glass substrates at 4000 rpm for 60 s. During the spin coating (5 s after spinning), anhydrous toluene was dropped onto the

center of the substrate for better morphology of $CH_3NH_3PbI_3$ perovskite film. After spin coating, film was annealed on a hot plate at 70℃ for 30 min. Ag, Ni and Au were selected as top electrodes of resistive switching device. 50 μm × 50 μm, 200 μm × 200 μm and 400 μm × 400 μm of top electrodes were deposited on $CH_3NH_3PbI_3$ perovskite film by e-beam evaporation method with the shadow mask. The evaporation was performed at 1×10^{-6} Torr of pressure and room temperature.

Device characterization: For XRD measurements, a $CH_3NH_3PbI_3$ perovskite film was coated on a glass substrate. The XRD pattern was obtained from X-Ray Diffractometer (BRUKER MILLER Co., D8-Advance) with Cu Kα radiation (λ = 1.54056 Å). XRD data was recorded at room temperature in the range of 10−60° of 2θ range with a step size of 0.02° and scan speed of 2 degree per minute. The surface and cross sectional images were obtained from Field Emission Scanning Electron Microscope (ZEISS, MERLIN Compact). Images were obtained with an in-lens secondary electron detector at 1kV accelerating voltage. The $I-V$ characteristics were measured by Agilent 4156C semiconductor analyzer with direct current (DC) voltage sweeping mode. Resistive switching by alternating voltage pulses were measured by the Agilent 4156C semiconductor analyzer. All of the electrical properties were measured in a vacuum chamber (6×10^{-2} Torr). To observe conduction mechanism in the $CH_3NH_3PbI_3$ films, the conductance of $CH_3NH_3PbI_3$ films coated on Ag/Ti/SiO_2/Si substrate at room temperature was measured by CAFM (Park

systems XE100) in a glovebox, which was Ar atmosphere. A platinum coated STM-type tip was used to substitute platinum counter electrodes.

DFT calculation: The first-principles density functional theory (DFT) calculations based on the projected augmented wave (PAW) pseudopotential were performed using the Vienna Ab-initio simulation package (VASP) code. The nudged elastic band (NEB) method was employed in computing the activation energy along the migration path. As the present DFT study assumes the zero Kelvin temperature condition, the orthorhombic phase of the $CH_3NH_3PbI_3$ was used for the calculation. The supercell include 48 atoms (orthorhombic unit cell) for the iodine vacancy and 182 atoms ($2 \times 2 \times 1$ orthorhombic cell) for the interstitial iodine. The cutoff energy for plane-wave basis set was chosen to be 550 eV and the gamma point was sampled in the Brillouin-zone integration. Atomic positions were relaxed until the forces were reduced below 0.02 eV/Å.

2.3. Results and Discussion

The $CH_3NH_3PbI_3$ thin films used for this study were 400-nm-thick and the average grain size was approximately 133 nm. Despite a large variation in grain size, the $CH_3NH_3PbI_3$ thin films were uniformly spin-coated on Pt/Ti/SiO_2/Si substrates. Figure 10 shows that the $CH_3NH_3PbI_3$ thin film is polycrystalline and of a single-phase organolead halide as shown in the X-ray diffraction pattern in Figure 10.[17]

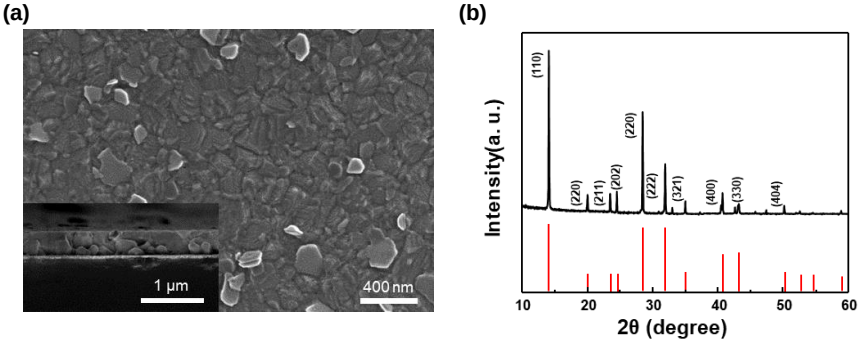

Figure 10 (a) Plane-view and cross-sectional SEM images of a 400 nm-thick $CH_3NH_3PbI_3$ thin film on Pt/Ti/SiO_2/Si substrate. (b) X-ray diffraction pattern of a $CH_3NH_3PbI_3$ film on SiO_2/Si substrate. Red lines are XRD pattern from Ref. 17

After spin-coating and annealing of the $CH_3NH_3PbI_3$ thin film, MIM vertical structure cells were fabricated by depositing 50 μm × 50 μm top metal electrodes such Ag, Ni and Au using a shadow mask and an electron beam evaporator. To achieve pinhole-free $CH_3NH_3PbI_3$ films with uniform thicknesses we used a rapid crystallization method using N,N-dimethylformamide and toluene as the solvent for the OHP precursors (CH_3NH_3I and PbI_2). Because $CH_3NH_3PbI_3$ and the precursors are minimally

soluble in toluene, the addition of toluene significantly reduced the solubility of $CH_3NH_3PbI_3$ in the mixed solution and rapid crystallization occurred. As a result of the rapid crystallization, we obtained uniform and pinhole-free $CH_3NH_3PbI_3$ films.[26] Using the pinhole-free MIM cells (Figure 11), we succeeded in measuring insulating ground states from the solution-processed $CH_3NH_3PbI_3$ films.

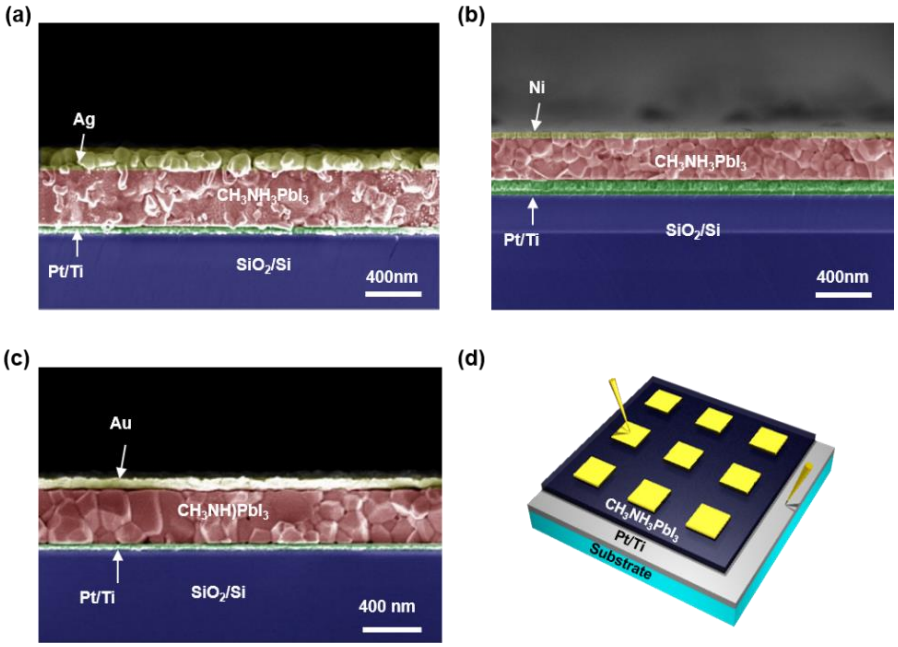

Figure 11 SEM images of the vertical structure devices. (a-c), Each device has (a) Ag, (b) Ni, (c) Au electrodes. The thickness of $CH_3NH_3PbI_3$ thin film is about 320-400nm. We adopted two types of metals, such as Ag and Ni to the top electrodes to investigate the resistive switching properties. The minimum thickness of the top electrodes is about 50 nm. (d) Schematic of the metal/$CH_3NH_3PbI_3$/metal vertical structure for resistive switching.

A typical *I–V* curve of the Ag/$CH_3NH_3PbI_3$/Pt cells is shown in Figure 12a. With the applied voltage sweep of 0 V → + 0.15 V → 0 V → - 0.15 V → 0 V,

the measured current values were plotted on a logarithmic scale. The hysteresis loop indicates that the device exhibits bipolar switching.[21,27] Initially, the device was in an insulating (high resistance) state (HRS) with current levels of 10^{-10}–10^{-9} A. The current increased abruptly when the applied voltage was approximately 0.13 V. Then, the device retained a conducting (low resistance) state (LRS) with current levels near 10^{-3} A. It should be noted that the current density for the LRS state is over hundreds of times higher than the photocurrent densities of the $CH_3NH_3PbI_3$ films studied for photovoltaic applications. The equivalent electric field for the onset of the low resistance state is 3.25×10^3 V/cm for the 400-nm-thick $CH_3NH_3PbI_3$ film. The transition between HRS (OFF state) and LRS (ON state) is switchable and the ON/OFF ratio is as high as ~10^6. The $CH_3NH_3PbI_3$ devices do not require electroforming, even though the thickness of the $CH_3NH_3PbI_3$ thin film is approximately 400 nm. In Figure 12b, The *I*–*V* curves do not show remarkable variation in the SET voltages, indicating the electroforming-free characteristic of the $CH_3NH_3PbI_3$-based MIM cells. It is interesting that the operation electric field (3.75×10^3 V/cm) is comparable to the applied electric field for the switchable photovoltaic effect in $CH_3NH_3PbI_3$–based devices (1.2×10^4 V/cm), where the electrical programming with optical reading out was explained by the migration of defect ions.

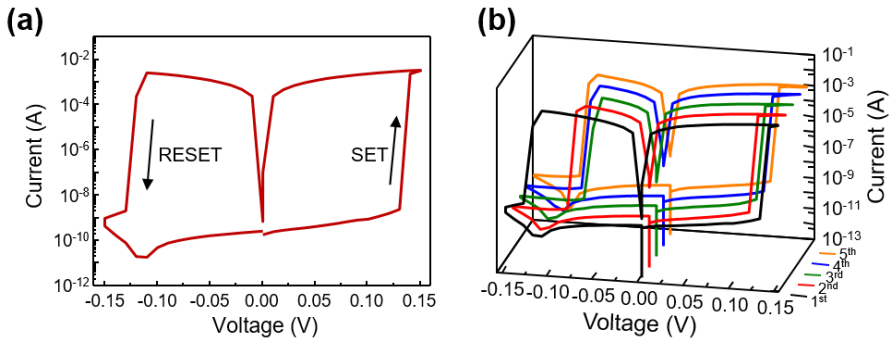

Figure 12 Resistive switching properties of Ag/$CH_3NH_3PbI_3$/Pt cells. (a) Typical current-voltage (*I-V*) characteristic of Ag/$CH_3NH_3PbI_3$/Pt cells. (b) *I-V* characteristics of a Ag/$CH_3NH_3PbI_3$/Pt cell from 5 initial voltage sweeps. SET voltage is + 0.15 V and RESET voltage is – 0.15 V.

Resistive switching with voltage pulses is also possible for the device (Figure 13a). At voltages of ± 0.15 V (200-ms pulse width), the $CH_3NH_3PbI_3$-based MIM cell showed reproducible resistive switching with ON/OFF ratios above 10^6 over 350 cycles. We measured 50 Ag/$CH_3NH_3PbI_3$/Pt cells for resistive switching with writing voltages of ± 0.15 V (250-ms pulse width). As plotted in Figure 13b, the 50 electrodes showed an average ON/OFF ratio of 1.12×10^6 without considerable deviations.

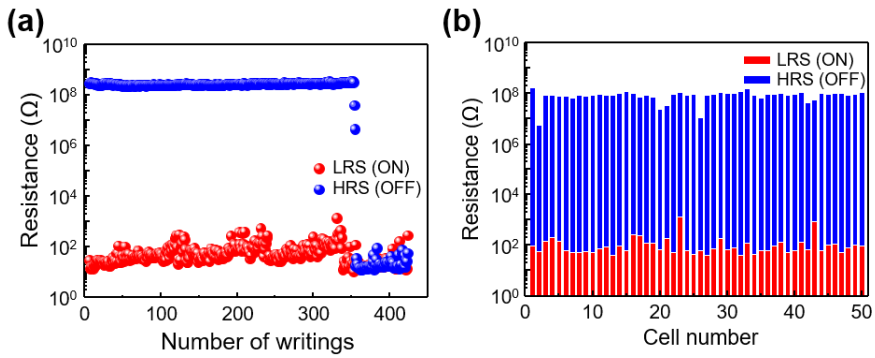

Figure 13 (a) Reversible resistive switching measured with a writing voltage of 0.15 V and a reading voltage of 0.02 V. The pulse width of the writing voltage was 200 ms. (b) High and low resistance states for 50 different cells. The average on/off ratio is calculated to be 1.12 x 10^6.

The reproducibility of the uniform HRS and LRS levels of many cells indicates that the $CH_3NH_3PbI_3$-based MIM cells are feasible for reliably high ON/OFF ratio resistive switching with a low electric field. The typical retention characteristics of the ON and OFF states for an Ag/$CH_3NH_3PbI_3$/Pt cell showed that the ON state is stable up to 11000 s (Figure 14).

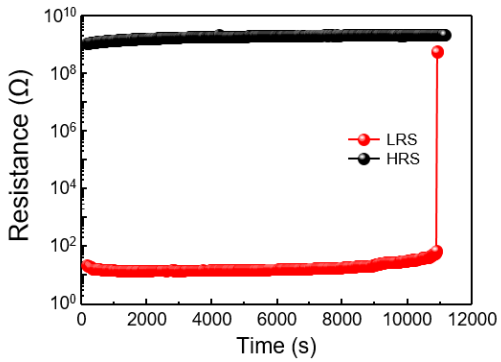

Figure 14 Retention characteristics of the Ag/$CH_3NH_3PbI_3$/Pt/SiO_2/Si device.

The SET and RESET voltages of the $CH_3NH_3PbI_3$ devices depends on the ratio of methylammonium iodide (MAI) and lead iodide (PbI_2) precursors. The

operation voltage is less than ± 0.15 V when the MAI/ PbI_2 ratio is 1. When the MAI/ PbI_2 ratio is 1.1 or 0.9, the $CH_3NH_3PbI_3$ thin films are metallic and hysteretic *I-V* characteristics cannot be obtained (Figure 15).

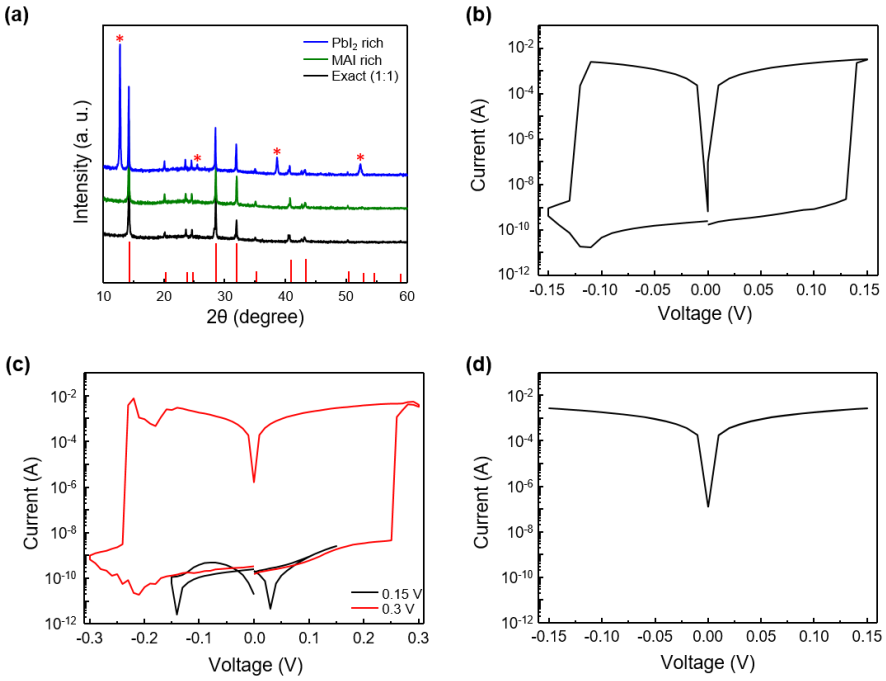

Figure 15 (a) Stoichiometry-dependent X-ray diffraction patterns of a $CH_3NH_3PbI_3$ films by the controlling of the ratio of methylammonium and lead iodide. (Black line-exact stoichiometry, green line-methylammonium iodide rich, blue line-lead iodide rich, red line-Ref 20.). In the blue line, peaks for PbI_2 appear at 12.67, 25.49, 38.59, and 52.33 degrees (Red stars, JCPDS No. 00-007-0235). (b) *I-V* characteristics of the $CH_3NH_3PbI_3$ thin films are synthesized by the ratio of methylammonium and lead iodide is 1:1. (c) Methylammonium iodide rich and (d) Lead iodide rich. The thickness of the thin films is fixed to 320-350 nm.

To understand the current conduction mechanism at the interface between the top electrode and the $CH_3NH_3PbI_3$ layer, we highlighted the *I–V* curves for the ON and OFF states of the Ag/$CH_3NH_3PbI_3$/Pt and Ni/$CH_3NH_3PbI_3$/Pt cells (Figure 15a). For both cells which adopted Ag and Ni top electrodes, the OFF state *I–V* curves show linear and non-linear regions, indicating that space-charge limited conduction is dominant. The ON state *I–V* curves exhibit perfectly ohmic behavior, suggesting the formation of highly conducting paths between the top and bottom electrodes. The dependence of the current levels for the ON and OFF states of Ag/$CH_3NH_3PbI_3$/Pt cells on the area of the top electrode was investigated (Figure 15b). Although the area of the top electrode was increased 64 fold, the current levels for the ON states did not increase, whereas the current levels for the OFF states varied considerably at the nA scale. This result indicates that the conducting paths for the ON states are localized, namely, filamentary.[21, 22, 28,29]

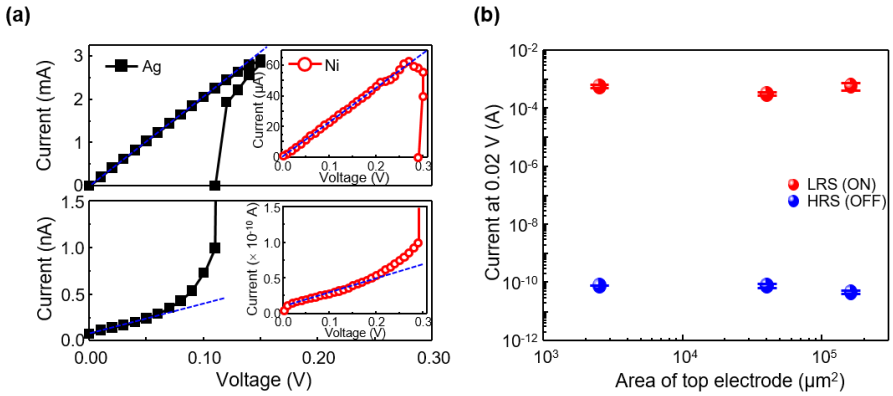

Figure 16 Dependence of the top electrodes and electrode area. (a) Linear-scale *I-V* characteristics of the ON (LRS) and OFF states. (b) Dependence of ON and

OFF state current levels on the area of Ag top electrodes for Ag/$CH_3NH_3PbI_3$/Pt cells.

Ag is known to be relatively active metal than Ni and Au. MIM cells with Ag top electrodes showed operation voltages less than ± 0.14 V (Figure 17a), whereas cells with Ni and Au top electrodes showed higher operation voltages over ± 0.4 V (Figure 17b and c). It is suggested that the electrochemical activity of the top electrode plays a role in triggering the abrupt resistive switching behavior.

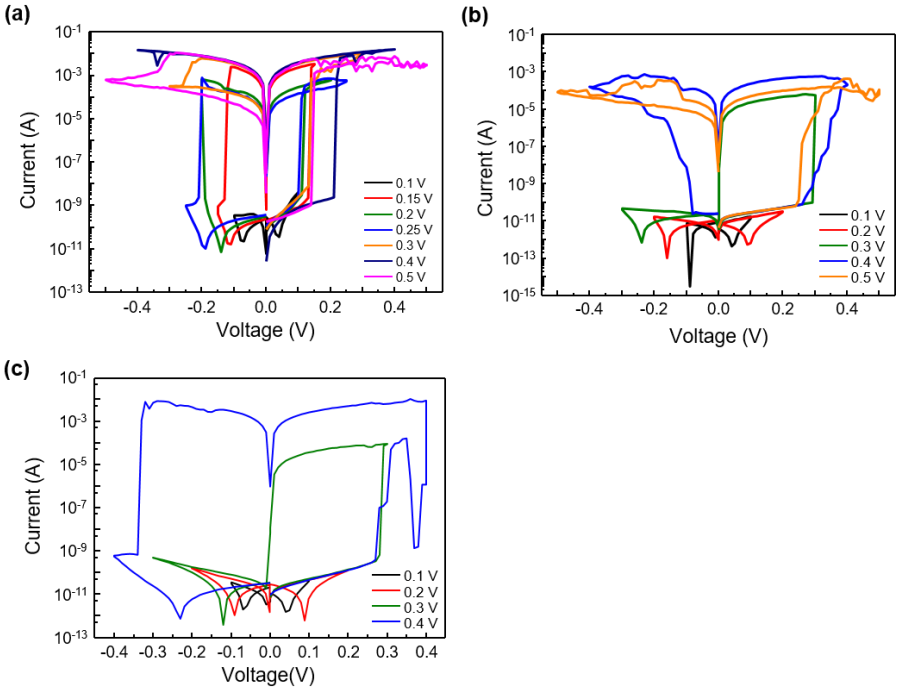

Figure 17 Dependence of the top electrodes. (a) Ag/$CH_3NH_3PbI_3$/Pt, (b) Ni/$CH_3NH_3PbI_3$/Pt and (c) Au/$CH_3NH_3PbI_3$/Pt cells. The cells adopt (a) Ag, (b) Ni and (c) Au top electrodes show hysteretic I-V curves which are applicable to resistive switching. The cells with Ag top electrodes are switchable in low

SET/RESET voltage. With high SET voltage (> 0.25 V), these cells could not be turned off perfectly. The cells adopt Ni and Au top electrodes had relatively higher SET voltages (> 0.3 V).

We performed conducting atomic force microscopy (CAFM) on a $CH_3NH_3PbI_3$ film on Ag/Ti/SiO_2 substrate in order to determine whether the pre-existing grain boundaries or non-uniformity in the thickness play a role in forming conducting filaments for the ON states. The 400-nm-thick film was granular. The grain size varied from 300 nm to 1000 nm and the rms roughness is about 40 nm with a maximum peak-to-valley depth of 60 nm, as shown in Figure 18.

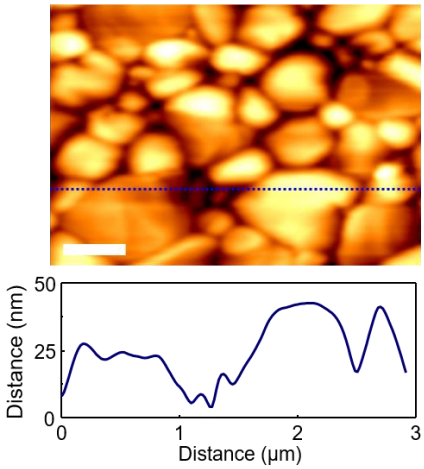

Figure 18 Scanning probe microscopy images of $CH_3NH_3PbI_3$ thin films. (a) A topological AFM image of the $CH_3NH_3PbI_3$/Ag structure. The scale of bars is 500 nm. The tip moves 3 μm through the blue dotted line to measure the roughness by the distance (down).

At a bias of 0.1 V on the probe tip, the $CH_3NH_3PbI_3$ film was uniformly insulating with current levels of several tens of nA (Figure 19a). The film became conducting with current levels of ~50 μA at a bias of 1 V (Figure 19b). The whole area of the film was conducting regardless of the morphology, suggesting that conducting filaments which could not be visualized with the AFM tip of ~50 nm radius were formed through the $CH_3NH_3PbI_3$ film under an external bias.

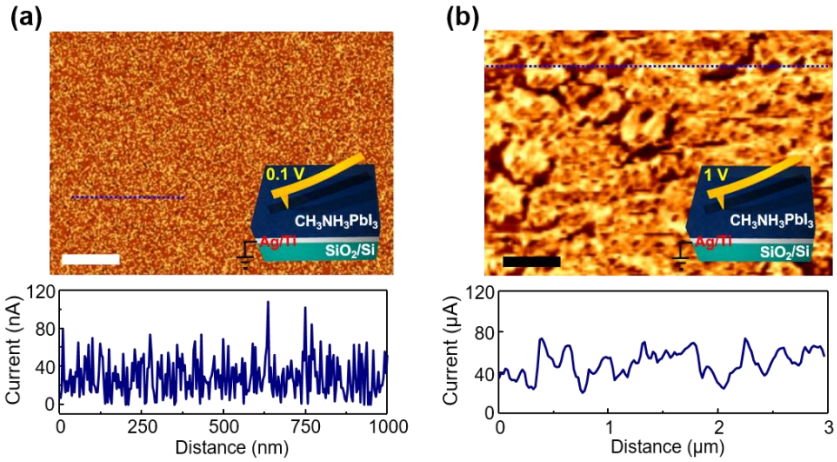

Figure 19 Scanning probe microscopy images of $CH_3NH_3PbI_3$ thin films. (a), (b) CAFM images of a $CH_3NH_3PbI_3$/Ag structure with platinum coated tip biases of (a) 0.1 V and (b) 1 V. The scale of bars is 500 nm. The tip moves through the blue dotted line to measure the current vs the distance (down).

We could vary the grain size in the $CH_3NH_3PbI_3$ film from 70 nm to 600 nm by controlling the annealing condition of the film (Table 2).

	Annealing temperature (°C)	Time (min)	Annealing atmosphere	Average grain size (nm)	Standard deviation of grain size (nm)	Endurance (cycles)
Sample 1	100	40	DMF	601.30	±74.17	0
Sample 2	100	40	Ambient	147.06	±22.86	4
Sample 3	70	40	Ambient	103.35	±10.47	50
Sample 4	70	1	Ambient	89.45	±6.75	38
Sample 5	No annealing	N/A	Ambient	71.15	±5.39	17

Table 2 Five $CH_3NH_3PbI_3$ films with different grain sizes by controlling annealing condition.

Combined with X-ray diffraction data, endurance measurements revealed that obtaining the films with the constitute composition without secondary phases is more important than tailoring the grain size (Figure 20 and 21).

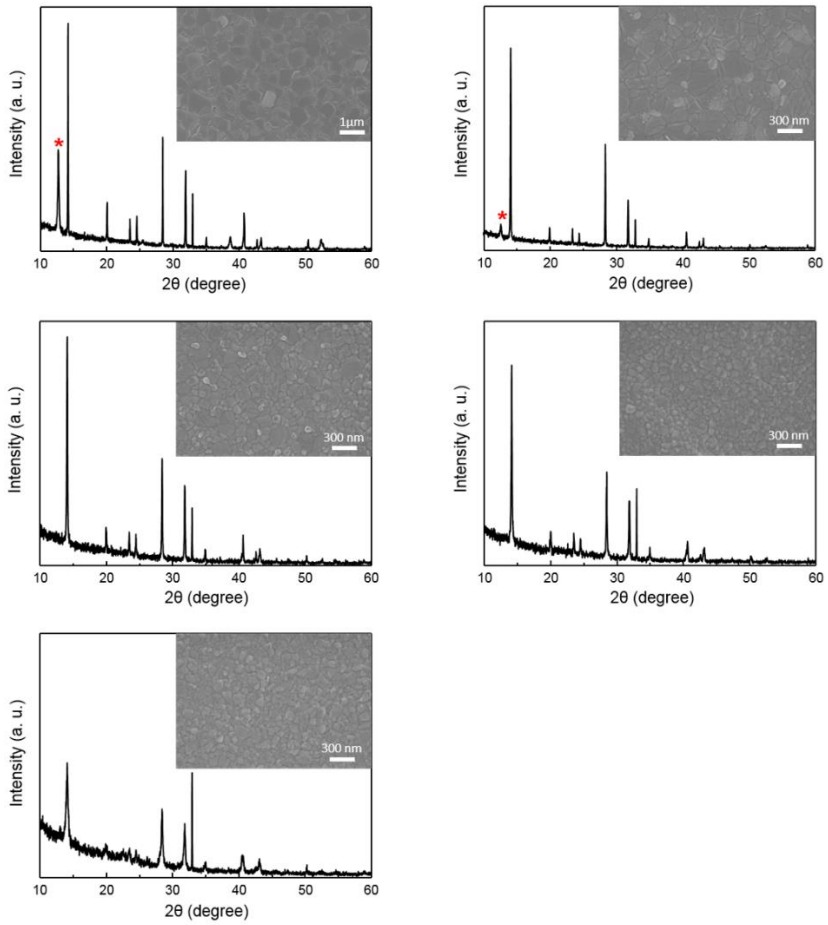

Figure 20 X-ray diffraction patterns and SEM images for $CH_3NH_3PbI_3$ films synthesized using annealing conditions. (a) Sample 1 (100 °C, 40mins, DMF), (b) Sample 2 (100 °C, 40 mins, ambient), (c) Sample 3 (70 °C, 40 mins, ambient), (d) Sample 4 (70 °C, 1 min, ambient), (f) Sample 5 (No heat treatment, ambient). The diffraction peak near 12.6° for PbI_2 (Red star, (a)) is absent. The insets of each XRD pattern are plain-view SEM images of each sample.

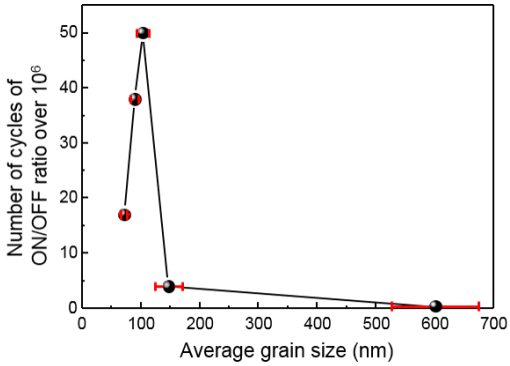

Figure 21 Number of cycles with ON/OFF ratio over 10^6 from endurance measurements (total 50 number of cycles) for $CH_3NH_3PbI_3$ films with different grain sizes.

To compare the extraordinary resistive switching properties of the $CH_3NH_3PbI_3$-based devices with those of conventional resistive switching devices, we plotted the ON/OFF ratio vs. the reciprocal of the electric field for SET ($1/E_{SET}$) in Figure 21.[20,29-46] Binary transition metal oxides, such TiO_2 and TaO_x, the most widely studied materials for resistive switching, show varied ON/OFF ratios and relatively low $1/E_{SET}$ values ($< 1 \times 10^{-5}$ cm/V). Inorganic perovskites, such as $SrTiO_3$, exhibit low $1/E_{SET}$ values near ~10^{-5} cm/V with relatively low ON/OFF ratios. Organic materials demonstrate the lowest $1/E_{SET}$ values, showing large variations in the ON/OFF ratios. The OHP $CH_3NH_3PbI_3$ has a relatively high ON/OFF ratio of $> 10^6$ and the highest $1/E_{SET}$ value, which is one order of magnitude higher than those of chalcogenides.

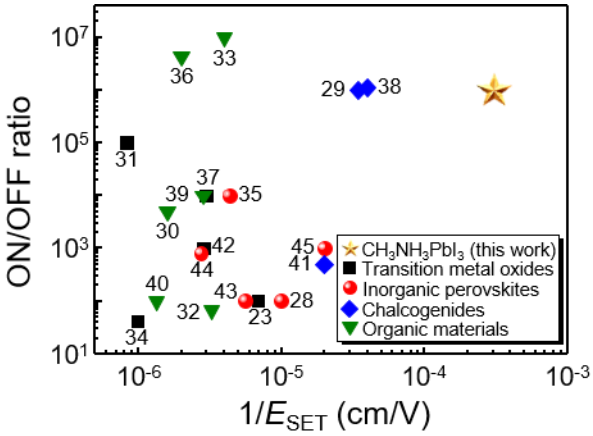

Figure 22 Comparison with various resistive switching materials. The ON/OFF ratio of resistive switching devices including the $CH_3NH_3PbI_3$–based cells.

We note that the formation of conducting filaments by Ag migration though the 400-nm-thick $CH_3NH_3PbI_3$ film is rare for a SET voltage as low as 0.13 V, which corresponds to 3.25×10^3 V/cm. Conventional Ag migration resistive switching memories typically require much higher electric fields for SET (> 1×10^5 V/cm) and undergo electroforming under even higher electric fields.[21] This suggests that charged defect ions (point defects) in the film itself rather metal ions are responsible for the ultralow electric field resistive switching.[21,22,24] To reveal the origin of the resistive switching in the $CH_3NH_3PbI_3$-based cells, we studied the migration energies of representative point defects in $CH_3NH_3PbI_3$ with density functional theory (DFT) calculations, assuming that the hysteretic *I*–*V* characteristics are caused by the migration of charged point defects.[47-51] $CH_3NH_3PbI_3$ has abundant, intrinsic, shallow point defects. We consider two point defects, $V_I^{\bullet}$ and i_I' (split interstitial), which are thermodynamically stable and likely to be highly mobile.[8,9,12,17,52] The

generalized gradient approximation functional is adopted and the migration barrier is calculated using the nudged elastic band method. As shown in Figure 23, $V_I^{\bullet}$ and $i_I^{\prime}$ can migrate with low activation energies of 0.25 eV and 0.15 eV, respectively. These energies are significantly lower than the migration barriers of $V_O^{\bullet\bullet}$ in TiO_2 (1.15 eV) and $SrTiO_3$ (1.22 eV) which are widely used in resistive switching devices.[53,54] Therefore, we suggest that the low switching voltages of the $CH_3NH_3PbI_3$ cells are due to the small migration barriers of the charged anion defects.

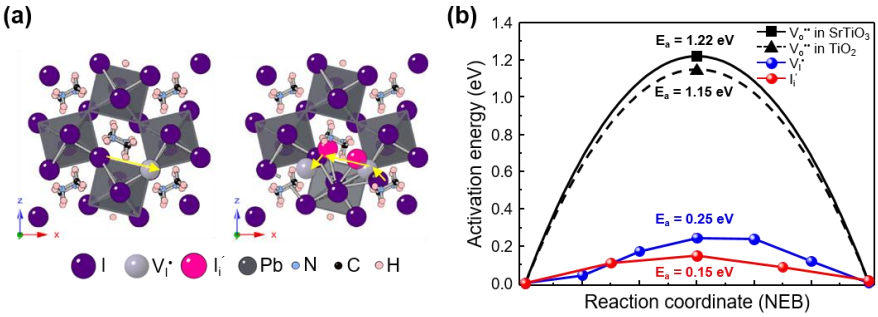

Figure 23 DFT calculation for native point defects in $CH_3NH_3PbI_3$. (a) Schematic migration paths of $V_I^{\bullet}$ (left) and $I_i^{\prime}$ (right) in the unit cell of $CH_3NH_3PbI_3$. The center of the split interstitial is moved to adjacent I site, and the direction of the split rotates to another [110] direction. (b) DFT calculation about the activation energy for the movements of $V_I^{\bullet}$ and $I_i^{\prime}$ to the next sites.

To provide plausible explanation for the resistive switching in the Ag/$CH_3NH_3PbI_3$/Pt cells, we illustrated the procedure of filament formation and annihilation due to the migration of $i_I^{\prime}$ (Figure 24).

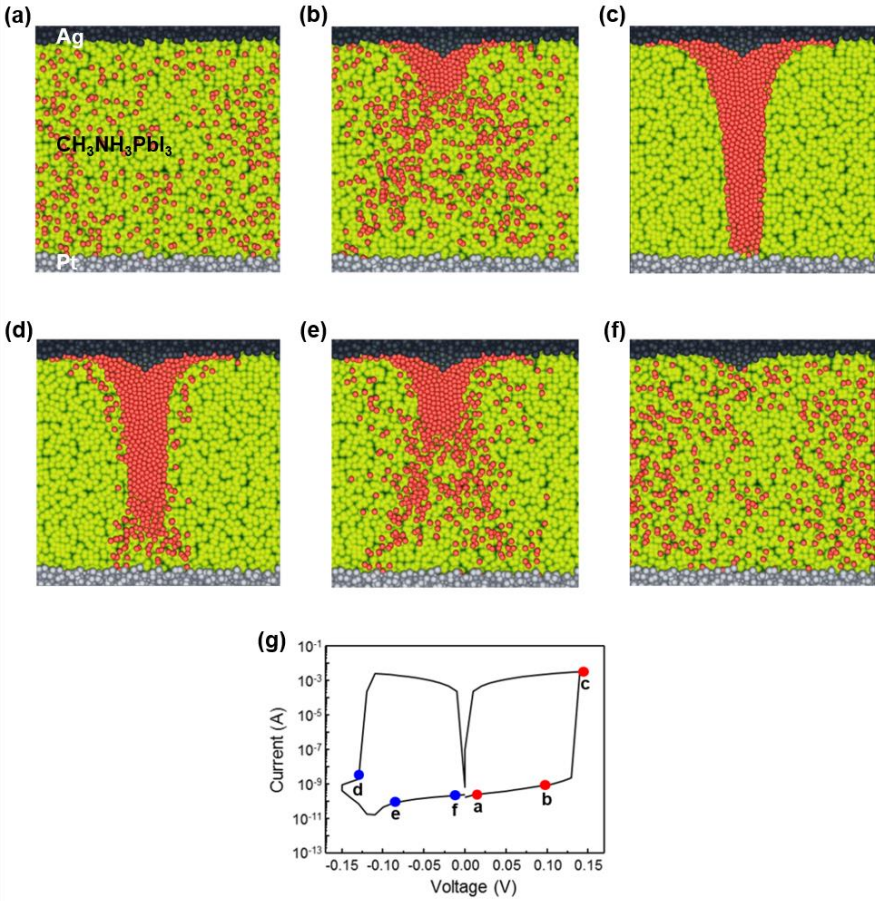

Figure 24 Schematic of filamentary resistive switching behaviour in Ag/$CH_3NH_3PbI_3$/Pt cells by defect ion migration. (a) Initial state of Ag/$CH_3NH_3PbI_3$/Pt cells with iodine interstitials ($I_i^{'}$). (b) Ion migration of iodine interstitials by applying positive electric field (+ 0.15 V). (c) Fully formed conducting filament (ON state). (d, e) Ion migration of iodine interstitials by applying negative electric field (- 0.15 V). (f) Rupture of the conducting filament (OFF state). (g) Corresponding *I-V* curve.

Since $i_I^{'}$ and $V_i^{\bullet}$ are oppositely charged each other, the unintentional migration of $V_i^{\bullet}$ can rupture the conducting filaments which was form by the aggregation of $i_I^{'}$. Thus, obtaining $CH_3NH_3PbI_3$ films with similarly charged point defects is

expected to be critical for reliable resistive switching performance for long-term operation. Since the migration of the defect ions could be much slowed down at lower temperatures, the filamentary resistance switching behavior deteriorated significantly at 150 K and 100 K (Figure 25).

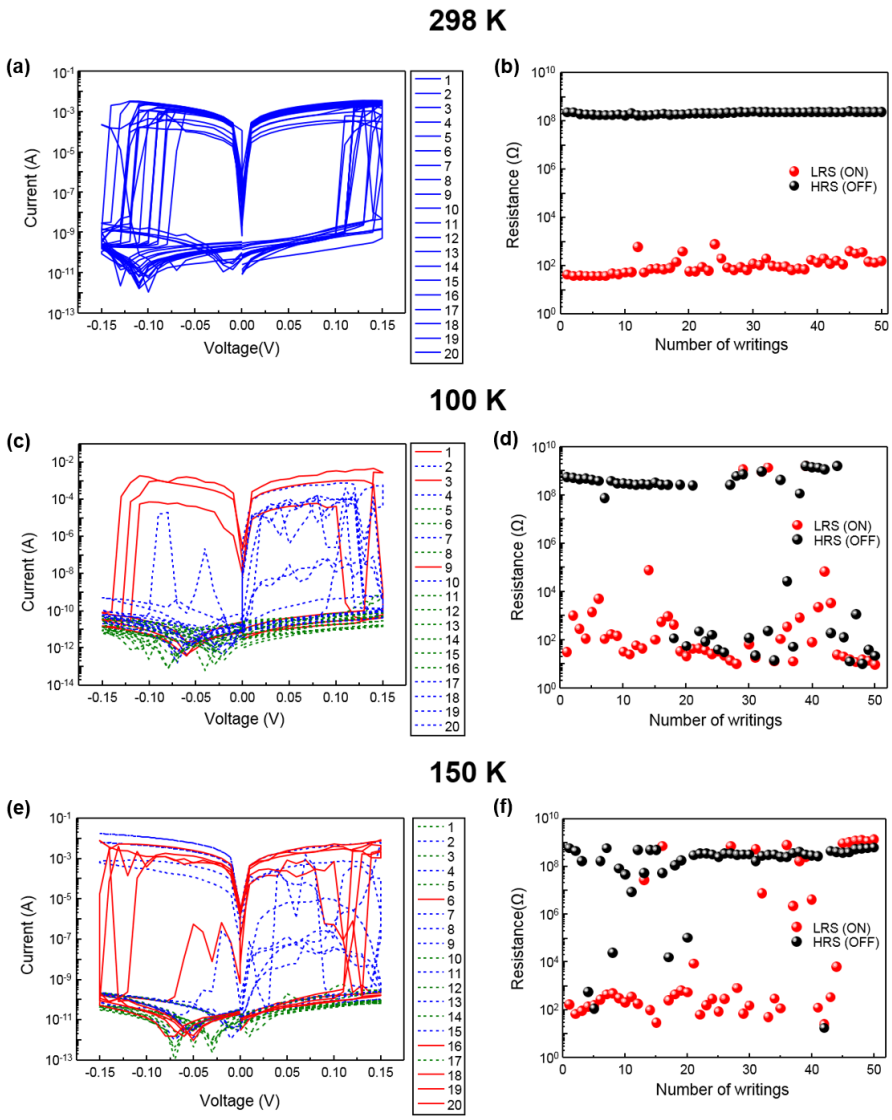

Figure 25 Resistive switching properties of Ag/$CH_3NH_3PbI_3$/Pt cells measured at different temperatures. (a) I-V curves of 20 cells measured at room temperature. (b) The endurance of a cell measured at room temperature. (c) I-

V curves of 20 cells measured at 100 K. (d) The endurance of a cell measured at 100 K. (e) I-V curves of 20 cells measured at 150 K. **f**, The endurance of a cell measured at 150 K.

Since the high ON/OFF ratio is giant and abrupt, multilevel resistive switching could be exploited for the $CH_3NH_3PbI_3$ devices. *I–V* characteristics of the Ag/$CH_3NH_3PbI_3$/Pt cells under different compliance currents are shown in Figure 26a. The distribution of multilevel ON states upon a number of writing cycles is shown in Figure 26b.

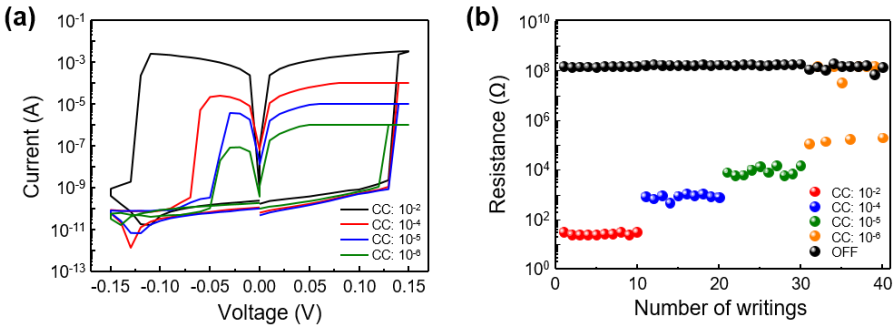

Figure 26 Multilevel resistive switching properties. (a) I-V characteristics of Ag/$CH_3NH_3PbI_3$/Pt cells under three different compliance currents (CC=10^{-2} A, 10^{-4} A, 10^{-5} A, 10^{-6} A). (b) Reversible resistive switching over 40 cycles with different current compliances of 10^{-2}, 10^{-4}, 10^{-5}, and 10^{-6} A. The switching pulse duration is fixed to 200 ms, and the switching voltage is ±0.15 V.

Distinguishably different resistance states can be found for compliance currents of 10^{-2} A, 10^{-4} A and 10^{-5} A. However, the endurance for resistive switching with the compliance current of 10^{-6} A is relatively poor. With the lower compliance current, the endurance for reversible resistance switching is deteriorated (Figure 27).

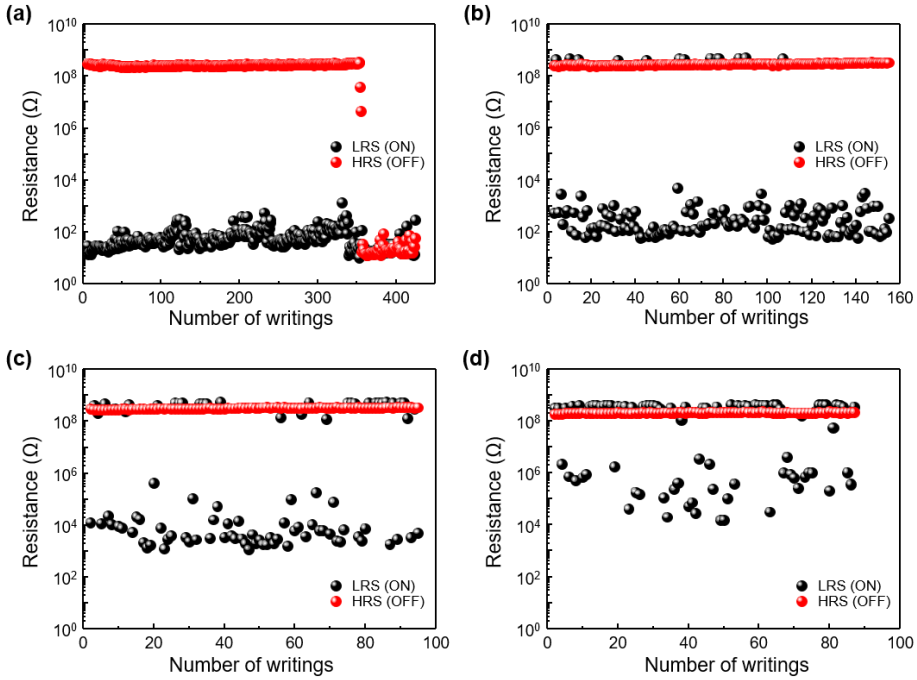

Figure 27 Dependence of the compliance currents in switching pulses. Switching with various current compliances of (a) 10^{-2} A, (b) 10^{-4} A, (c) 10^{-5} A, and (d) 10^{-6} A. The voltage of the switching pulses is 0.15 V. The pulse width is fixed to 250 ms. As illustrate in the figure, 10^{-2} A of the current compliance for reversible switching shows the most stable result. When the current compliance of the pulse is under 10^{-6} A, the reversible switching is impossible. With decreasing the current compliance of the switching pulses, a percent, the reversible switching is accurate, is decreasing. It is obvious that the higher current compliance for the reversible switching is applied, the better switching accuracy is performed.

This result clearly demonstrates that at least four different ON states can be achieved in the $CH_3NH_3PbI_3$ devices for the multilevel data storage by controlling the compliance current for the SET process. We believe that

synthesizing thinner pinhole-free $CH_3NH_3PbI_3$ films in a reproducible manner, controlling the formation of native point defects and understanding the underlying mechanisms exactly are urgently needed for improving endurance and retention properties of $CH_3NH_3PbI_3$-based resistive switching cells for real applications to data storage and minimizing the cell-to-cell variation for reliable operation, which will pave the way for a new material platform in developing high performance nonvolatile memories.

2.4. Conclusion

In conclusion, we demonstrated multilevel resistive switching using an OHP. Solution-processed 400-nm-thick $CH_3NH_3PbI_3$ films with Ag top and Pt bottom electrodes exhibited electroforming-free resistive switching with a low SET voltage of ~0.13 V and high ON/OFF ratios of ~10^6 under ± 0.15 V pulses. Based on these extraordinary properties, four-level storage capability of the $CH_3NH_3PbI_3$–based devices was demonstrated. We attributed the high performance resistive switching behavior of the $CH_3NH_3PbI_3$–based devices to the energetically benign migration of anions defects ($V_I^{\bullet}$ and i_I'), but further studies are needed to identify the mechanism responsible for the ultralow electric field resistive switching. Enhancements in switching speed, endurance and retention are also necessary and may be achieved by controlling the doping concentration, crystallinity and large area compositional uniformity of the OHP film. The inherent structural flexibility and the number of possible combinations for ABX_3-type OHPs will support intensive studies for other electronic device applications beyond resistive switching memories. Finally, we believe that the solution-processed $CH_3NH_3PbI_3$–based cells are promising for microelectronics built on flexible substrates.

2.5 References

1. D. B. Mitzi, S. Wang, C. A. Feild, C. A. Chess, A. M. Guloy, *Science* **1995**, 267, 1473.

2. D. B. Mitzi, K. Chondroudis, C. R. Kagan, *Inorg. Chem.* **1999**, 38, 6246.

3. N. J. Jeon, J. H. Noh, W. S. Yang, Y. C. Kim, S. Ryu, J. Seo, S. I. Seok, *Nature* **2015**, 517, 476

4. G. E. Eperon, S. D. Stranks, C. Menelaou, M. B. Johnston, L. M. Herz, H. J. Snaith, *Energ. Environ. Sci.* **2014**, 7, 982

5. W. J. Yin, T. Shi, Y. Yan, *Adv. Mater.* **2014**, 26, 4653.

6. H. S. Kim, C. R. Lee, J. H. Im, K. B. Lee, T. Moehl, A. Marchioro, R. Humphry-Baker, J. H. Yum, J. E. Moser, M. Grätzel, N. G. Park, *Sci. Rep.* **2012**, 2, 591

7. J. H. Im, C. R. Lee, J. W. Lee, S. W. Park, N. G. Park, *Nanoscale* **2011**, 3, 4088

8. M.-H. Du, *J. Mater. Chem. A* **2014**, 2, 9091.

9. C. Eames, J. M. Frost, P. R. F. Barnes, B. C. O'Regan, A. Walsh. M. S. Islam, *Nat. Commun.* **2015**, 6, 7497.

10. K. Tanaka, T. Takahashi, T. Ban, T. Kondo, K. Uchida, N. Miura, *Solid. State. Commun.* **2003**, 127, 619

11. G. Xing, N. Mathews, S. Sun, S. S. Lim, Y. M. Lam, M. Grätzel, S. Mhaisalkar, T. C. Sum, *Science* **2013**, 342, 344

12. Z. Xiao, Y. yuan, Y. Shao, Q. Wang, Q. Dong, C. Bi, P. Sharma, A. Gruverman, J. Huang, *Nat. Mater.* **2015**, 14, 193.

13. W. Tress, N. Marinova, T. Moehl, S. M. Zakeeruddin, M. K. Nazeeruddin, M. Grätzel, *Energ. Environ. Sci.* **2015**, 8, 995.

14. J. Kim, S.-H. Lee, J. H. Lee, K.-H. Hong, *J. Phys. Chem. Lett.* **2014**, 5, 1312.

15. W. J. Yin, T. T. Shi, Y. F. Yan. *Appl. Phys. Lett* **2014**, 104, 063903.

16. A. Poglitsch, D. Weber, *J. Chem. Phys.* **1987**, 87, 6373.

17. C. C. Stoumpos, C. D. Malliakas, M. G. Kanatzidis, *Inorg. Chem.* **2013**, 52, 9019.

18. Y. Kawamura, H. Mashiyama, K. Hasebe, *J. Phys. Soc. Jpn.* **2002**, 71, 1694.

19. R. Gottesman, E. Haltzi, L. Gouda, S. Tirosh, Y. Bouhadana, A. Zaban, *J. Phys. Chem. Lett.* **2014**, 5, 2662.

20. Q. Lai, Z. Zhu, Y. Chen, S. Patil, F. Wudl, *Appl. Phus. Lett.* **2006**, 88, 133513.

21. R. Waser, R. Dittmann, G. Staikov, K. Szot, *Adv. Mater.* **2009**, 21, 2632

22. F. Pan, S. Gao, C. Chen, C. Song, F. Zeng, *Mater. Sci. Eng. R-Rep.* **2014**, 83, 1

23. I. Valov, R. Waer, J. R. Jameson, M. N. Kozicki, *Nanotechnology* **2011**, 22, 254003.

24. R. Waser, M. Aono, *Nat. Mater.* **2007**, 6, 833.

25. E. J. Yoo, M. Lyu, J. H. Yun, C. J. Kang, Y. J. Choi, L. Wang, *Adv. Mater.* **2015**, 27, 6170

26. M. Xiao, F. Huang, W. Huang, Y. Dkhissi, Y. Zhu, J. Etheridge, A. Gray-Weale, U. Bach, Y.-B. Cheng, L. Spiccia, *Angew. Chem.* **2014**, 126, 10056.

27. G. Dearnale, A. M. Stoneham, D. V. Morgan, *Rep. Prog. Phys.* **1970**, 33, 1129.

28. Y. Aoki, C. Wiemann, V. Feyer, H.-S. Kim, C. M. Schneiger, H. I.-Yoo, M. Martin, *Nat. Commun.* **2014**, 5, 3473.

29. W. Xue, W. Xiao, J. Shang, X. X. Chen, X. J. Zhu, L. Pan, H. W. Tan, W. B. Zhang, Z. H. Ji, G. Liu, X.-H. Xu, J. Ding, R.-W. Li, *Nanotechnology* **2014**, 25, 425204.

30. Y. J. Fu, F. J. Xia, Y. L. Jia, J. Y. Li. X. H. Dia, G. S. Fu, B. Y. Zhu, B. T. Liu, *Appl. Phys. Lett.* **2014**, 104, 223505.

31. M. Morales-Masis, S. J. van der Molen, W. T. Fu, M. B. Hesselbeerth, J. M. van Ruitenbeek, *Nanotechnology* **2009**, 20, 095710.

32. S. Gao, C. Song, C. Chen, F. Zeng, F. Pan, *J. Phys. Chem. C* **2012**, 116, 17955.

33. C. B. Lee, B. S. Kang, A. Benayad, M. J. Lee, S.-E. Ahn, K. H. Kim, G. Stefanovich, Y. Park, I. K. Yoo, *Appl. Phys. Lett.* **2008**, 93, 042115.

34. J. Huang, D. Ma, *Appl. Phys. Lett. 2014*, 105, 093303.

35. S. ChandraKishore, A. Pandurangan, *R. Soc. Chem. Adv.* **2014**, 4, 9905.

36. M.-J. Lee, C. B. Lee, D. Lee, S. R. Lee, M. Chang, J. H. Hur, Y.-B. Kim, C.-J. Kim, D. H. Seo, S. Seo, U.-I. Chung, I.-K. Yoo, K. Kim, *Nat. Mater.* **2011**, 10, 625.

37. X. He, X. Li, *Appl. Phys. Lett.* **2013**, 102, 221601.

38. D. I. Son, T. W. Kim, J. H. Shim, J. H. Jung, D. U. Lee, J. M. Lee, W. I. Park, W. K. Choi, *Nano Lett.* **2010**, 10, 2441.

39. A. A. Bessonov, M. N. Kirikova, D. I. Petukhov, M. Allen, T. Ryhänen, M. J. A. Bailey, *Nat. Mater.* **2015**, 14, 199.

40. T. Sakamoto, H. Sunamura, H. Kawaura, T. Hasegawa, T. Nakayama, M. Aono, *Appl. Phys. Lett.* **2003**, 82, 3032.

41. J. Chen, D. Ma, *J. Appl, Phys.* **2006**, 100, 034512.

42. R. Soni, P. Meuffels, A. Petraru, M. Weides, C. Kügeler, R. Waser, H. Kohlstedt, *J. Appl. Phys.* **2010**, 107, 024517.

43. B. J. Choi, D. S. Jeong, S. K. Kim, C. Rohde, S. Choi, J. H. Oh, H. J. Kim, C. S. Hwang, K. Szot, R. Waser, B. Reichenberg, S. Tiedke, *J. Appl. Phys.* **2005**, 98, 033715.

44. S.-L. Li, D. Shang, J. Li, J. Gang, D. Zheng, *J. Appl. Phys.* **2009**, 105, 033710.

45. K. Szot, W. Speier, G. Bihlmayer, R. Waser, *Nat. Mater.* **2006**, 5, 312.

46. M. Hasan, R. Dong, H. J. Choi, D. S. Lee, D.-J. Seong, M. B. Pyun, H. Hwang, *Appl. Phys. Lett.* **2008**, 92, 202102.

47. H. J. Snaith, A. Abate, J. M. Ball, G. E. Eperon, T. Leijtens, N. K. Noel, S. D. Stranks, J. T.-W. Wang, K. Wojciechowski, W. Zhang, *J. Phys. Chem. Lett.* **2014**, 5, 1511.

48. J. M. Azpiroz, E. Mosconi, J. Bisquert, F. De Angelis, *Energ. Environ. Sci.* **2015**, 8, 2118.

49. E. L. Unger, E. T. Hoke, C. D. Bailie, W. H. Nguyen, A. R. Bowring, T. Heumüller, M. G. Christoforo, M. D. McGehee, *Energ. Environ. Sci.* **2014**, 7. 3690.

50. D. A. Egger, E. Edri, D. Cahen, G. Hodes, *J. Phys. Chem. Lett.* **2015**, 6, 279.

51. A. Walsh, D. O. Scanlon, S. Chen, X. Gong, S. H. Wei, *Angew. Chem.* **2014**, 53, 1.

52. W. J. Yin, T. T. Shi, Y. F. Yan, *J. Phys. Chem. C* **2015**, 119, 5253.

53. Z. Zhang, Q. Ge, S.-C. Li, B. D. Kay, J. M. White, Z. Dohnálek, *Phys. Rev. Lett.* **2007**, 99, 126105.

54. B. P. Uberuaga, L. J. Vernon, *Solid State Ionics* **2013**, 253, 18.

Chapter 3

Morphologically enhanced flexible memory

Quote

Richard P. Feynman "The same equations have the same solutions.”

3.1. Introduction

Organometal halide perovskites (OHPs) with the chemical formula ABX_3 (A is an organic cation, B is Sn or Pb, X is a halide anion) were developed that showed superior optical/electrical properties to traditional semiconducting materials through their large light absorption coefficients, long charge carrier diffusion lengths, and structural and compositional flexibilities.[1-11] Due to their unique properties, OHPs are compatible for various optoelectronic devices such as all-solid-state solar cells,[12-14] light emitting diodes,[15-16] and photodetectors.[17-18] More interestingly, mixed ionic-electronic conduction is observed in OHPs, which is attributed to the migration of ions and charge defects. For example, the formation of a conducting path or a self-doped p-i-n structure in OHP thin films is caused by the migration of native defect species with external biases. Owing to these properties, OHPs have been utilized as insulators in resistive switching memories and artificial synapses. Resistive switching devices and artificial synapses that adopted halide perovskites as the insulating layer have been reported[19-24]. However, the performance was poor with low on/off ratio and short endurance. Moreover, Choi et al. showed an unprecedented improvement in resistive switching devices using OHPs with on/off ratios up to 10^6 under an ultralow operation electric field of 3.25×10^3 V/cm by utilizing a metal/insulator/metal (MIM) structure, unraveling the great potential of OHPs in resistive switching devices.[25] It was reported that changes in the resistivity of OHP insulating layers were attributed to the formation/rupture of conducting filaments caused by the external electric field. However, the operation speed of the previous OHP based-resistive switching device was over 200 ms.

Endurance was still limited to approximately 350 cycles, which is inferior to the endurance of triple-level cell (TLC) NAND flash memories. Generally, TLC NAND flash memories have an endurance of 1000 cycles, which is a minimum criterion for storage devices.[26] The endurance of the device depends on the uniformity and morphology of the OHP thin film to prevent switching failure by localizing the electric field at a specific point of the OHP thin film. Thus, we pay attention to controlling the thickness and morphology, including grain size and peak-to-valley depths in OHP thin films, which play a vital role in high-performance resistive switching devices with extended endurance. The previous solution process-dripping antisolvent during spin coating-could not establish a uniform grain size and low peak-to-valley depths because in the OHP thin films fabricated by dripping antisolvent, the antisolvent cannot penetrate every area of the OHP thin film at the same time.

Here, we show that the durability of OHP-based resistive switching devices can be significantly improved by controlling the uniformity and morphology of polycrystalline OHP thin films. Morphology-improved smooth OHP thin films with a small crystal grain size were obtained by adding a suitable amount of hydrogen iodide (HI) as the additive[27]. Therefore, the use of this smooth OHP thin film as an insulating layer significantly increased the endurance from 350 cycles to over 1300 cycles with an on/off ratio of 10^6 s, and operation time at the level of a few hundreds of micro-seconds was achieved. Our result is the highest value obtained for OHP-based resistive switching devices so far. We measured the current-voltage characteristics of OHP resistive switching devices at various temperatures, with different top electrodes, and with vertical/lateral

device structures to describe the switching and conduction mechanisms in the low- and high-resistance states. In addition, we demonstrate that flexible resistive switching devices with the structural flexibility of OHPs can be operated at the extremely low bending radius of 5 mm. We believe this study would create a new paradigm for resistive switching devices with opportunities in low-cost low-power consumption flexible resistive switching devices.

3.2. Experimental Procedures

Materials preparation: Methylammonium iodide (CH_3NH_3I) was prepared by reacting methylamine (22 mL, 33% in ethanol, Aldrich) and hydriodic acid (10 mL, 57 wt% in water, Aldrich). Reacting solution was vigorously stirred at 0 °C under N2 for 3 h. The product was collected by rotary evaporation under vacuum at 80 °C, dissolved in isopropyl alcohol, and precipitated from ethyl ether 3 times before drying at 50 °C under N_2 for 12 h.

Film formation and MIM cell fabrication: Pt (50 nm)/Ti (20 nm)-coated substrates were deposited by an electron beam. A perovskite solution was prepared by mixing equal molar quantities of PbI_2 and CH_3NH_3I in DMF with a concentration of 40 wt%. To obtain a pinhole-free ultra-uniform perovskite film, a different volume (2–8 vol%) of HI was added to the $CH_3NH_3PbI_3$ solution followed by spin-coating on Pt/Ti-coated substrates at 4000 rpm/m for 200 s and annealing on a hot plate at 100 °C for 10 min under a N_2 atmosphere. The device was completed using the electron beam-evaporation of 100 nm thick Ag or Au through the shadow mask at a pressure of $1x10^{-6}$ Torr.

Device characterization: For XRD measurements, a $CH_3NH_3PbI_3$ perovskite film was coated on a glass substrate. The XRD pattern was obtained using an X-ray diffractometer (BRUKER MILLER Co., D8-Advance) with Cu-Kα radiation (λ = 1.54056 Å). XRD data was recorded at room temperature in the 2θ range 10−60° with a step size of 0.02° and scan speed of 2°/min. The surface and cross-sectional images were obtained by field emission scanning electron microscopy (ZEISS, MERLIN Compact). Images were obtained with an in-lens

secondary electron detector at 1 kV accelerating voltage. The *I-V* characteristics were measured using an Agilent 4156C semiconductor analyzer with DC voltage sweeping mode. Resistive switching by alternating voltage pulses was measured by the Agilent 4156C semiconductor analyzer. All electrical properties were measured in a vacuum chamber (6 x 10^{-2} Torr). To observe the conduction mechanism in the $CH_3NH_3PbI_3$ films, the conductances of $CH_3NH_3PbI_3$ films coated on an Ag/Ti/SiO_2/Si substrate at room temperature were measured using a CAFM (Park systems XE100) in a glovebox under Ar atmosphere. A platinum-coated STM-type tip was used to substitute platinum counter electrodes.

3.3. Results and Discussion

The polycrystalline $CH_3NH_3PbI_3$ thin films used in this study were 300 nm thick and the average grain sizes were approximately 157.9 nm (rough film) and 82.17 nm (smooth film), as shown in the plane-view scanning electron microscopy (SEM) images Figure 28a (rough film) and 28b (smooth film).

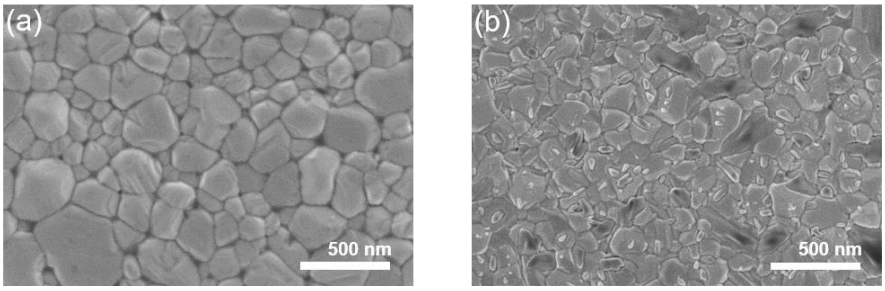

Figure 28 (a), (b) Plane-view SEM images of (a) rough films and (b) smooth $CH_3NH_3PbI_3$ thin films.

In addition, from typical cross-sectional SEM images, we could see pure perovskite layers on Pt/Ti deposited SiO_2/Si substrates (Figure 29a and b).

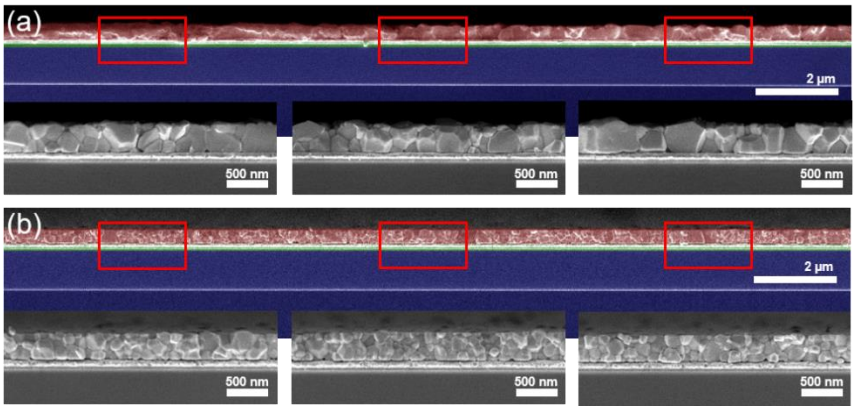

Figure 29 (a), (b) Cross-sectional SEM images of $CH_3NH_3PbI_3$/Pt/Ti/SiO_2/Si vertical structure with (a) rough films and (b) smooth films

A single-phase organolead halide was confirmed from its X-ray diffraction pattern as shown in Figure 29.[28]

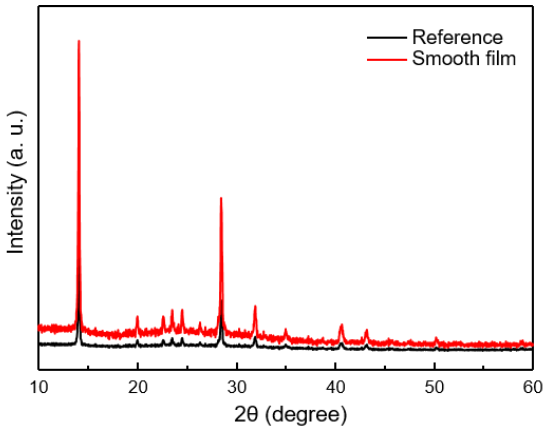

Figure 30 X-ray diffraction pattern of a $CH_3NH_3PbI_3$ film on SiO_2/Si substrate. Black lines are XRD pattern of ref. 24.

We performed atomic force microscopy (AFM) on a $CH_3NH_3PbI_3$ film on a Pt/Ti/SiO_2 substrate to compare the morphologies of rough $CH_3NH_3PbI_3$ films with smooth $CH_3NH_3PbI_3$ films, as shown in Figure 31a (rough film) and 31b (smooth film). For the rough film, the root mean square (RMS) roughness was 21.8 nm with a maximum peak-to-valley depth of 170 nm; the RMS roughness was 18.3 nm with a maximum peak-to-valley depth of 80 nm for the smooth film.

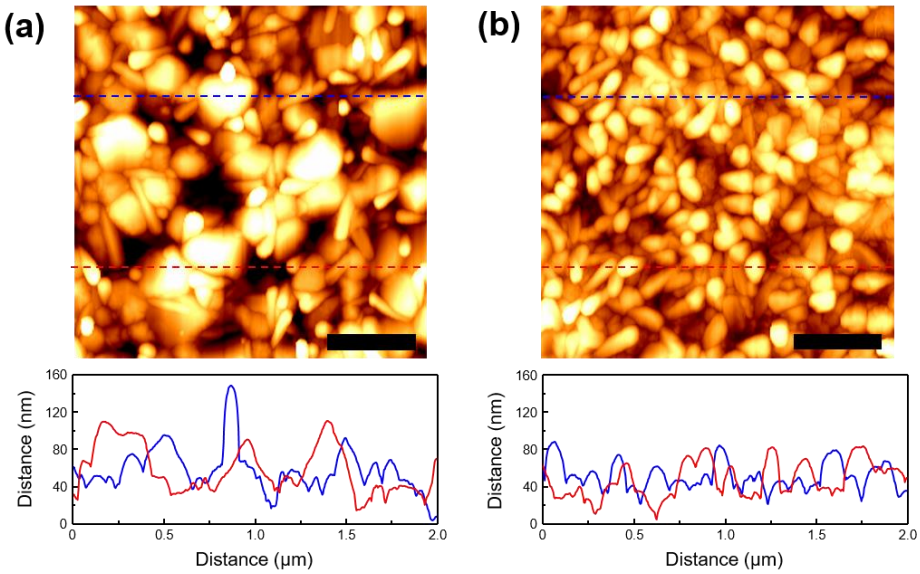

Figure 31 Topological atomic force microscopy images of (a) rough films and (b) smooth films. The scale of bars is 500 nm. The tip moves through the blue and red dotted lines to measure the roughness by the distance (bottom).

The results indicate that the smooth thin film shows smaller grain sizes and is more uniform than the rough thin film. The rapid crystallization method—which involves dripping antisolvent during spin-coating—is widely used[29-30]. However, the method contains a problem that can affect the uniformity of $CH_3NH_3PbI_3$ films. Because the antisolvent is dripped from the upper side of the film, the antisolvent cannot penetrate or slowly propagates from the top to the bottom of the thin film. To fabricate smooth and pinhole-free $CH_3NH_3PbI_3$ films with uniform thicknesses, we added hydroiodic acid with hypophosphorous acid, which is a stabilizer in a solution including the OHP precursors (CH_3NH_3I and PbI_2). It is considered that adding hypophosphorous acid in the precursor solution can significantly improve film quality. Further,

the addition of hydroiodic acid in the precursor solution raises the solubility of PbI_2 in the mixed solution and helps to achieve the accurate mixing ratio between CH_3NH_3I and PbI_2 because PbI_2 is not fully soluble in N,N-dimethylformamide[31].

To maximize the uniformity of the $CH_3NH_3PbI_3$ thin film, we fabricated five types of $CH_3NH_3PbI_3$ thin film with different concentrations of hydroiodic acid additive. The concentrations of the hydroiodic acid additive in the $CH_3NH_3PbI_3$ solution were 0%, 2%, 4%, 6%, and 8%. The samples with 0%, 2%, and 4% additive showed non-uniform thin films. However, the samples with 6% and 8% additive showed uniform and pinhole-free thin films. There was no difference in the qualities of the $CH_3NH_3PbI_3$ thin films between the $CH_3NH_3PbI_3$ solutions that contained 6% and 8% additive (Figure 32).

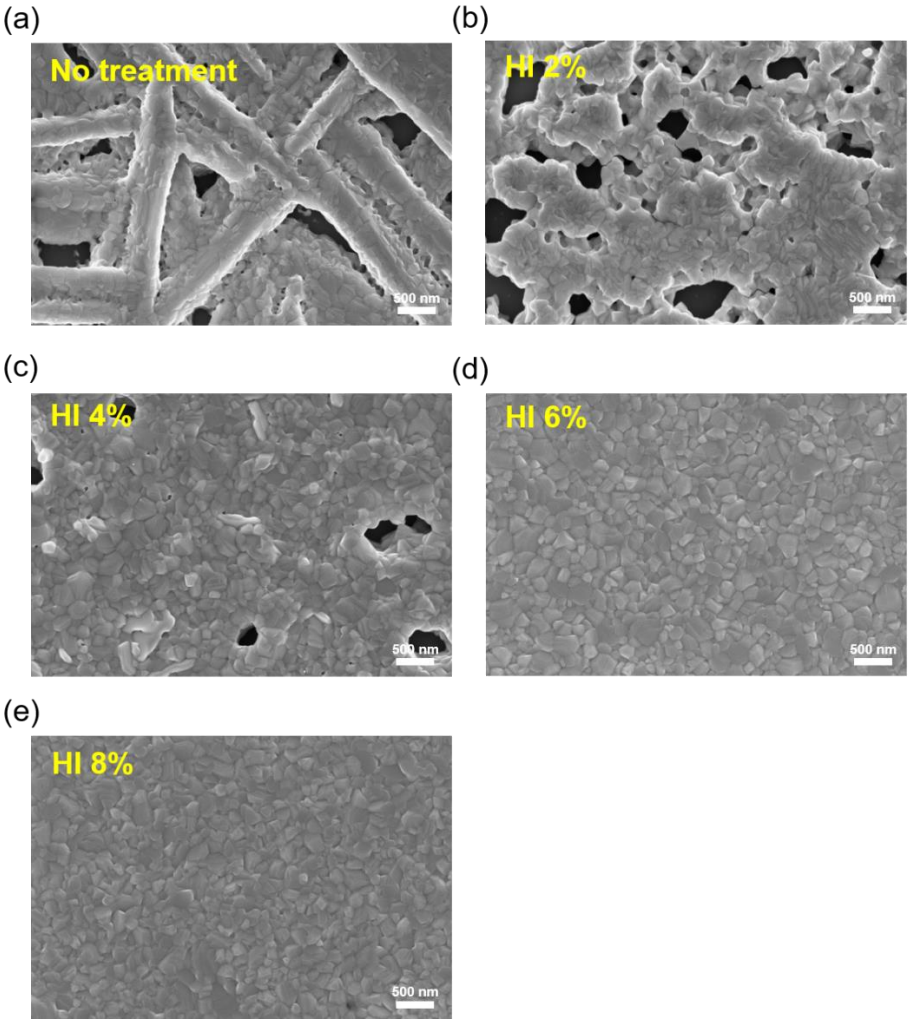

Figure 32 (a), (b), (c), (d), (e) Plane-view SEM images of $CH_3NH_3PbI_3$ thin film on Pt/Ti/SiO_2/Si substrate. The concentration of hydroiodic acid solution in $CH_3NH_3PbI_3$ solution is (a) 0%, (b) 2%, (c) 4%, (d) 6%, (e) 8%.

Therefore, the thin films for this study were fabricated with 6% additive in the $CH_3NH_3PbI_3$ solution. After spin-coating and annealing of the $CH_3NH_3PbI_3$ thin film, MIM vertical structure cells were fabricated by depositing 50 μm x 50 μm top Ag electrodes using a shadow mask and an electron beam evaporator.

The cross-sectional SEM images of the fabricated devices are shown in Figure 33.

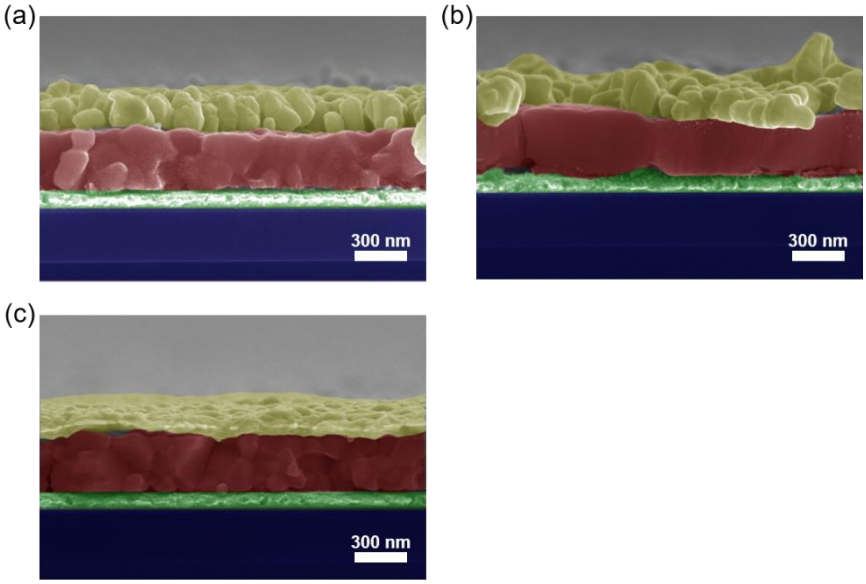

Figure 33 Cross-sectional SEM image of a fabricated (a) Ag/$MAPbI_3$ (smooth film)/Pt/Ti/SiO_2/Si, (b) Ag/$MAPbI_3$ (rough film)/Pt/Ti/SiO_2/Si, and (c) Au/$MAPbI_3$ (smooth film)/Pt/Ti/SiO_2/Si vertical structure.

The schematic illustration and typical current-voltage (*I*–*V*) curves of the Ag/$CH_3NH_3PbI_3$/Pt cells are shown in Figure 34a and b. With the applied voltage sweep of 0 V → +0.3 V → 0 V → -0.7 V → 0 V, the measured current values are plotted on a logarithmic scale. The measurement was conducted under a direct current (DC) voltage bias sweep to the top electrode (Ag). The bottom electrode (Pt) was grounded. The current compliance was 10^{-3} A to prevent the device from getting stuck in a conducting state (low resistance). Both the rough thin film and the smooth thin film showed equivalent *I*-*V* characteristics. The hysteresis loops indicate that the devices show general

bipolar switching behavior.[32] Initially, the device was in an insulating (high resistance) state (HRS) with current levels of 10^{-10}–10^{-9} A.

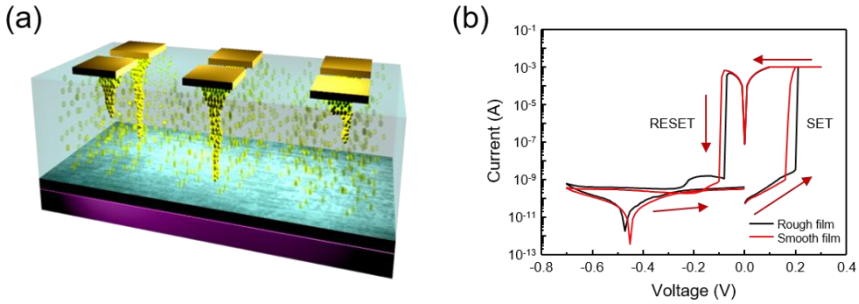

Figure 34 (a) Schematic illustration of the resistive switching mechanism of the organolead halide perovskite resistive switching device. (b) Typical current-voltage (I-V) characteristics of Ag/$CH_3NH_3PbI_3$/Pt devices.

The current increased abruptly when the applied voltage was approximately 0.18 V without any electroforming processes (Figure 35). Then, the device maintained a conducting (low resistance) state (LRS) with current levels of 10^{-3} A, which is the current compliance (SET).

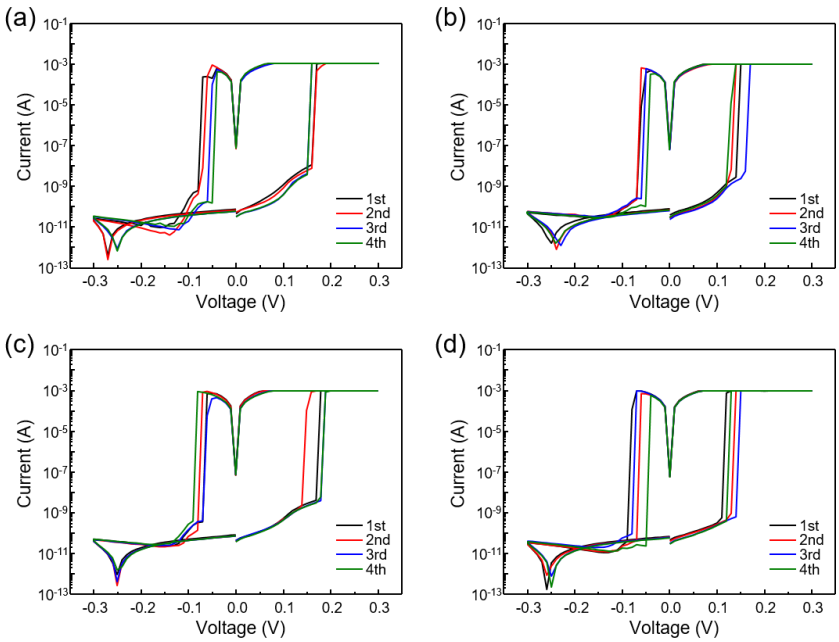

Figure 35 *I-V* characteristics of four Ag/$CH_3NH_3PbI_3$/Pt cells from 4 initial voltage sweeps. SET voltage is + 0.3 V and RESET voltage is – 0.3 V.

The constant ON/OFF ratio of the Ag/$CH_3NH_3PbI_3$/Pt cells with the rough thin film and the smooth thin film were approximately 10^6. The current decreased dramatically when the applied voltage was approximately -0.1 V (RESET). Even though the RESET operation occurs at –0.1 V, applying only –0.3 V is not enough to turn to HRS and can cause an imperfect RESET operation (Figure 36a). As the device repeats the SET/RESET operation, a successively higher RESET voltage is needed. To clarify the behavior of increasing RESET voltage, the DC bias voltage sweep was applied with higher voltages. With the applied voltage sweep of 0 V → +1 V → 0 V → –1 V → 0 V, while the SET voltage was retained, the RESET voltage increased continuously (Figure 36b).

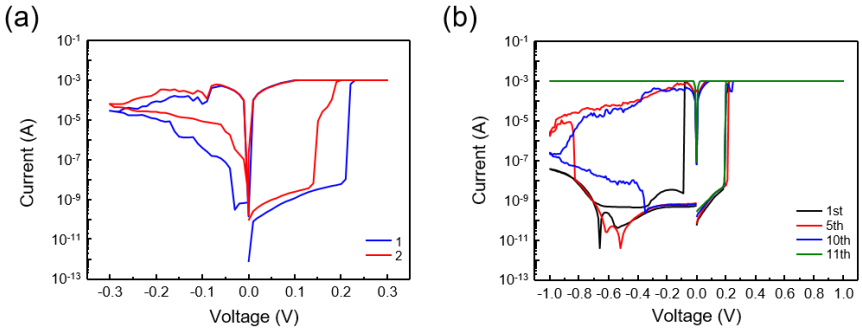

Figure 36 (a) Typical *I-V* characteristics of Ag/$CH_3NH_3PbI_3$/Pt devices with smooth $CH_3NH_3PbI_3$ thin films. (b) *I-V* characteristics of Ag/$CH_3NH_3PbI_3$/Pt devices with high voltage (± 1 V)

Without changes of the operating conditions or the type of thin film, all of the Ag/$CH_3NH_3PbI_3$/Pt cells show ON/OFF ratios above 10^6 s and similar SET/RESET voltages. The results suggest that the formation of a conducting path (filamentary) by external biases without any electro-forming process is the switching mechanism of the devices.[32-34]

Resistive switching with alternating current biases (voltage pulses) is also possible for devices that are fabricated with the rough thin film and the smooth thin film. An Ag/$CH_3NH_3PbI_3$/Pt cell with the rough thin film recorded 312 cycles (Figure 37a). However, an Ag/$CH_3NH_3PbI_3$/Pt cell with the smooth thin film recorded 1338 cycles (Figure 37b). The two devices were measured with SET voltage of +0.3 V (50 ms pulse width) and RESET voltage of –0.7 V (100 ms pulse width). Moreover, the Ag/$CH_3NH_3PbI_3$/Pt cell with the smooth thin film could be operated with the SET voltage of +0.4 V and the RESET voltage of –0.8 V (640 μs pulse width). With shorter pulsed biases, the Ag/$CH_3NH_3PbI_3$/Pt cell with the smooth thin film recorded 1290 cycles (Figure

37c). Because of the limitation of the pulse width of the semiconductor parameter analyzer that we used, applying pulse widths shorter than 640 μs was impossible. Since the operating voltages are increased, switching accuracy is also enhanced. For all measurements, the reading voltage was +0.05 V (640 μs pulse width).

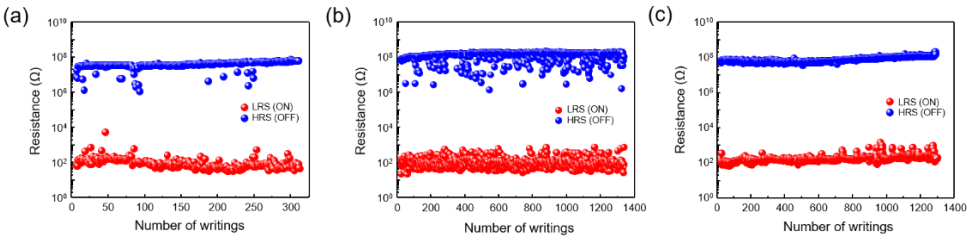

Figure 37 Resistive switching properties of Ag/$CH_3NH_3PbI_3$/Pt devices with rough and smooth $CH_3NH_3PbI_3$ thin films. (a), (b), (c) Reversible resistive switching measured with voltage pulses.

In the same manner as the measurement of *I-V* characteristics, a higher negative bias than positive bias should be applied to extend the endurance of the devices. Applying the same absolute value of the SET and RESET voltage to ±0.3 V leads to an incomplete RESET operation (Figure 38a). The results indicate that the smooth film shows better endurance with respect to electrical biases. The ON/OFF ratios of the devices with the rough thin film and the smooth thin film remained above 10^6 s. This result is the same as the *I-V* characteristics measured by the DC voltage bias sweep. The aspect of degradation in most devices was attributed to the LRS and prevented performing the RESET operation. The *I-V* characteristic of the device, which was stuck in LRS after an endurance test, is shown in Figure 38b. Even though a high negative bias was applied, the cell was turned to HRS very slowly. This

behavior suggests that the RESET operation is not perfect, or the conducting filament grows gradually during repeated SET/RESET operations.

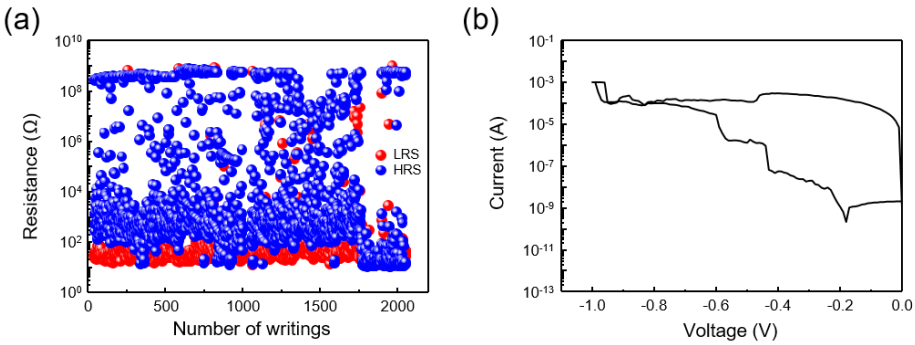

Figure 38 (a) Reversible resistive switching measured with SET voltage of + 0.3 V and RESET voltage of – 0.3 V. A reading voltage is + 0.05 V The pulse width of the SET voltage was 50 ms and the RESET voltage was 100 ms. (b) I-V characteristics of Ag/$CH_3NH_3PbI_3$/Pt devices after the device was stuck in low resistance state.

The typical retention characteristics of the ON and OFF states for an Ag/$CH_3NH_3PbI_3$/Pt cell showed that the ON state is stable up to 29800 s (Figure 39). The measurement of the retention characteristic was conducted at the applied reading voltage of +0.05 V every 10 seconds.

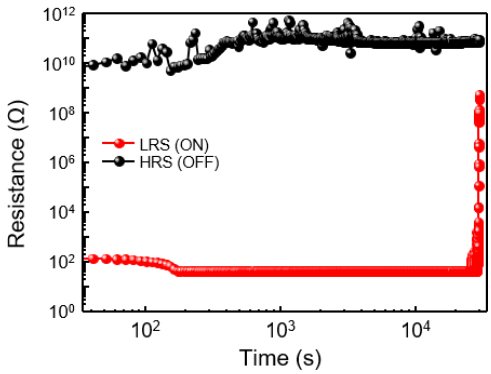

Figure 39 Retention characteristics of the Ag/$CH_3NH_3PbI_3$/Pt devices with smooth thin films.

To verify the long-term stability, we measured *I-V* characteristics of a Ag/$CH_3NH_3PbI_3$/Pt cell for 4 days. Since the $CH_3NH_3PbI_3$ iodizes Ag top electrodes[35], $CH_3NH_3PbI_3$ films can be degradable after depositing Ag top electrodes. The measurement was conducted every 24 hours. Also, the device was stored in vacuum chamber (under $5x10^{-2}$ Torr) to prevent the degradation of $CH_3NH_3PbI_3$ films by H_2O and O_2 in ambient condition. The Ag/$CH_3NH_3PbI_3$/Pt cell showed general resistive switching behavior for 3 days. However, the cell became perfectly insulating and couldn't show resistive switching behavior after 4 days (Figure 40). To prevent the degradation, approaches inserting a passivation layer between $CH_3NH_3PbI_3$ films and Ag top electrodes or using another top electrode material which is non-reactive with $CH_3NH_3PbI_3$ films are required.

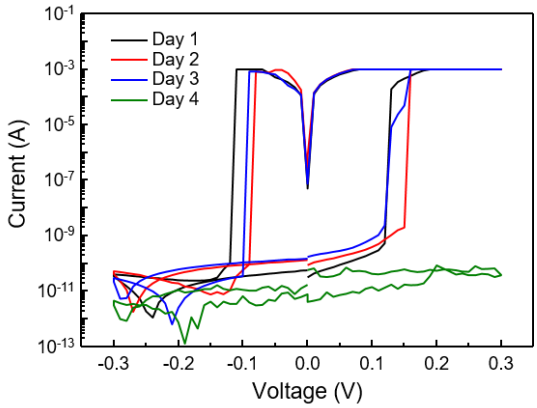

Figure 40 *I-V* characteristics of a Ag/$CH_3NH_3PbI_3$/Pt cell to describe a long term stability.

To investigate the conduction mechanism of the devices, we measured the *I-V* characteristics of the Ag/$CH_3NH_3PbI_3$/Pt cells with the smooth thin film at various temperatures. In low resistance state, only linear region was observed in the *I-V* curves (Figure 41a). It suggested that the ohmic conduction is dominant because the conducting filament connects between the top and bottom electrodes. However, both linear region and non-linear region were observed in high resistance state (HRS) (Figure 41b). The present studies of organolead halide perovskites based memories reported that space charge limited conduction (SCLC) was predominant in HRS[19-20]. Nevertheless, SCLC is not suitable to *I-V* characteristics of our device because the slope of non-linear region is rise by the increase of the temperature. To analyze the conduction mechanism in HRS, we fitted *I-V* curves and calculated average hopping distances (Figure 41b)[32].

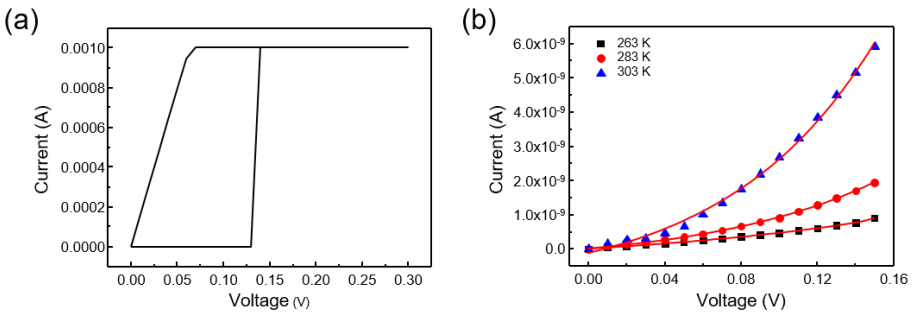

Figure 41 Linear current-voltage (*I-V*) characteristics of a Ag/$CH_3NH_3PbI_3$/Pt cell in (a) low resistance state, and (b) high resistance state.

Thermally assisted hopping is described by the equation,

$$J = \sigma_{TAH}E = n_c 2\nu_{TAH} a q_e \exp\left(\frac{\Delta H}{kT}\right) sinh\left(\frac{q_e E a}{2kT}\right)$$

where n_c is the concentration of majority carrier, q_e is elementary charge, υ is frequency factor, and a is the hopping distance[32]. We focused the relationship between temperature, *T* and the hopping distance, a. With the fitted *I-V* curves, solving a part of the equation,

$$J = Asinh\left(\frac{q_e E a}{2kT}\right), A = n_c 2\nu_{TAH} a q_e \exp\left(\frac{\Delta H}{kT}\right)$$

provided the hopping distance of 114.59 nm, 133.87 nm, and 163.82 nm at 263 K, 283 K, and 303 K, respectively. The hopping distance is rise by the increase of the temperature. It indicates that the conduction mechanism in HRS is thermally assisted hopping.

Typically, redox-based resistive switching behavior involves a valence change mechanism (VCM) or electrochemical metallization (ECM). VCM occurs in specific transition metal oxides and involves a migration of anions such as oxygen vacancies. This redox reaction involves a valence change of the cation sublattice and a change in electronic conductivity.[32,36] ECM is based on

the drift of electrochemically active metal cations such as Ag^{+} and Cu^{2+}. The drift of the metal cations due to external biases forms a conducting path or a filament through an insulating layer. Since the conducting filament is formed by the metal, *I*-*V* characteristics of the device adopting ECM show abruptly increased current levels during the SET process. Accoring to Waser et al.[36], *I*-*V* characteristics of the Ag/$CH_3NH_3PbI_3$/Pt cells is more close to that of an ECM device rather that of a VCM device in that the current increase at the SET voltage is very abrupt, suggesting that the switching mechanism of Ag/$CH_3NH_3PbI_3$/Pt is ECM.[37] Generally, the resistances of metal filaments are inversely proportional to the temperature.[38-39] However, the Ag/$CH_3NH_3PbI_3$/Pt cells do not show the temperature dependence of the metal filament. Since the variation range of the resistance is greater than the increase of the resistance with temperature increase, the temperature dependence of the resistance of the metal filament does not shown (Figure 42).

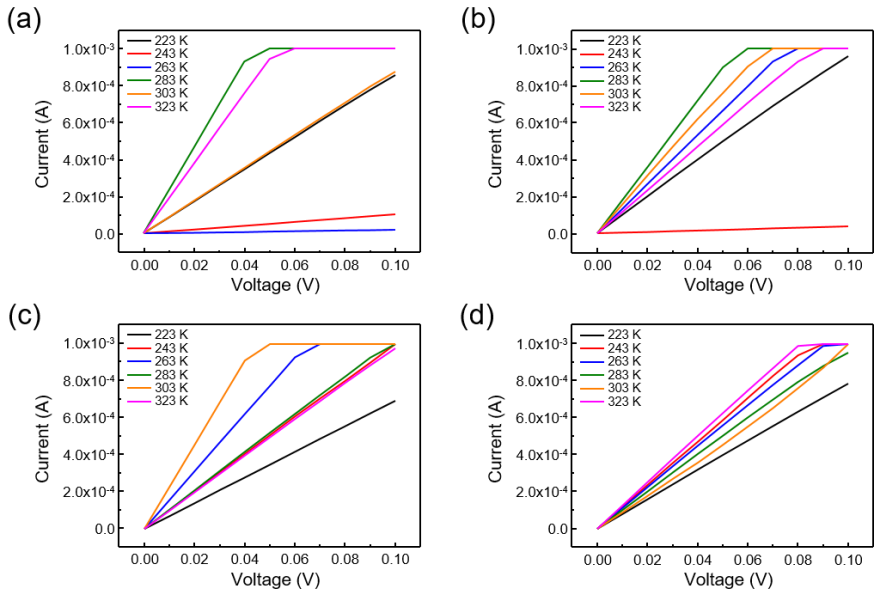

Figure 42 (a), (b), (c), (d) Typical I-V characteristics of Ag/$CH_3NH_3PbI_3$/Pt devices measured at 223 K, 243 K, 263 K, 283 K, 303 K and 323 K.

To investigate the composition of the conducting path (native defects or Ag ions), we estimated the resistivity of the filament. Generally, the size of the filament in resistive switching devices is 8-10 nm.[40] The resistivity of the filament in our devices was about 25.73 x 10-7 Ω•cm where the resistance was 9.832×10^{-3} Ω (1.017×10^{-4} A at 0.01 V) and the assumed diameter and length of the filament are 10 nm and 300 nm, respectively. The resistivity of the filament in our device is close to the resistivity of bulk Ag (15.87 x 10-7 Ω•cm at 273 K). The calculated result indicates that the filament of the device is formed by Ag ions from the top electrode. To investigate the effect of electrochemical activity of the top electrode, we measured the *I-V* characteristics of the device with an Au top electrode. In Figure 43a, general bipolar switching behavior was not observed from the device that adopts Au as the top electrode at high

voltages of ±2 V. Moreover, Figure 43b shows the *I-V* characteristic of a virgin Ag/$CH_3NH_3PbI_3$/Pt device with negative biases. Although negative biases of –8 V were applied, hysteretic *I-V* curves were not observed, in contrast to the *I-V* characteristic with positive biases. This result indicates that the migration of positively charged Ag ions from the top electrode contributes to the formation of the conducting path through the $CH_3NH_3PbI_3$ thin film. Moreover, the ultralow operation voltage of +0.3 V for the SET process is based on the unique properties of the OHPs. Since $CH_3NH_3PbI_3$ has a higher lattice parameter than the lattice parameter of inorganic perovskite materials, the native defect species can migrate easily. Moreover, the binding energy of the native defect species in $CH_3NH_3PbI_3$ is relatively low.[8] This unique property of $CH_3NH_3PbI_3$ also contributes to the migration of Ag ions to form conducting filaments through 300 nm-thick $CH_3NH_3PbI_3$ thin films.

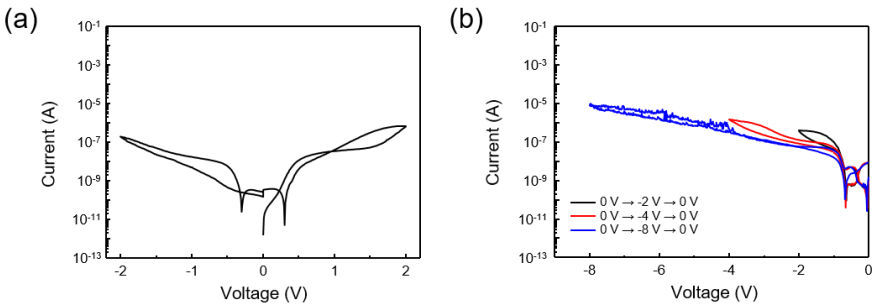

Figure 43 (a) Typical *I-V* characteristics of Au/$CH_3NH_3PbI_3$/Pt devices. (b) *I-V* characteristics of virgin Ag/$CH_3NH_3PbI_3$/Pt cells with negative biases. (c) Current-electric field (*I-E*) characteristics of a lateral-structure Pt/$CH_3NH_3PbI_3$/Pt device with various scan rates. (d) Linear *I-E* characteristics of vertical structure Ag/$CH_3NH_3PbI_3$/Pt devices (upper) and lateral structure

Pt/$CH_3NH_3PbI_3$/Pt device (bottom). The insets show schematic of the lateral and vertical devices.

To provide plausible descriptions of the formation of the conducting path in a vertical MIM structure device, we fabricated two different devices. One was a vertical MIM structure-Ag/$CH_3NH_3PbI_3$/Pt device, which has been explained. The other was a lateral MIM structure-Pt/$CH_3NH_3PbI_3$/Pt device on Pt interdigitated electrodes (IDEs), which were patterned 20-finger like electrodes with an interspacing of 5 μm.[18] A typical current-electric field (*I-E*) characteristic of the lateral MIM structure-Pt/$CH_3NH_3PbI_3$/Pt device is shown in Figure 44a. With the applied voltage sweep of 0 V → +0.5 V → 0 V → -0.5 V → 0 V, the measured current values are plotted on a logarithmic scale. The measurement was conducted under a DC voltage bias sweep at three different scan rates (50, 100, and 500 mV/s). The *I-V* characteristic of the lateral MIM structure-Pt/$CH_3NH_3PbI_3$/Pt device is similar to the dark current of hybrid perovskite solar cells and a photodetector in previous studies.[11, 18, 41] To identify *I-E* characteristics between the lateral and vertical structure-devices, linear *I-E* curves are shown in Figure 44b. Unlike the *I-E* characteristics of the vertical MIM structure-Ag/$CH_3NH_3PbI_3$/Pt device, a dramatic increase of current levels with the formation of conducting paths was not observed. This result originated from the different device structures. Since the lateral device has 5-μm gap between Pt electrodes which are non-active, the *I-E* hysteresis in Figure 44a can be attributed to the migration of native defect species of $CH_3NH_3PbI_3$. However, the vertical MIM structure device has 300-nm gap between Ag active electrodes and passive Pt electrodes. As mentioned earlier, the *I-E* hysteresis in the vertical

device is general bipolar switching behavior and originated from the migration of Ag ions. Therefore, active electrodes and enough electric field for resistive switching (or thin insulating layer) is essential.

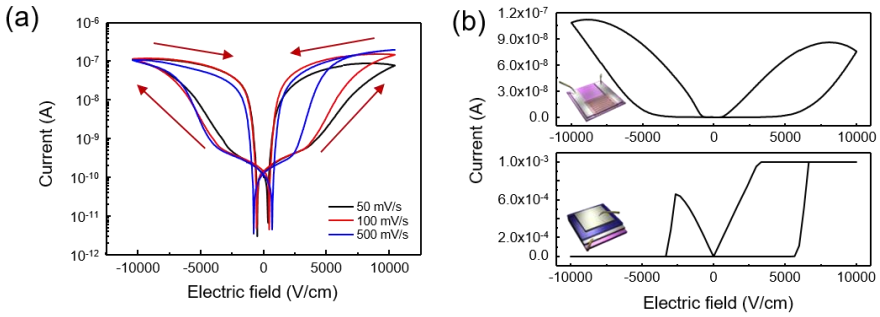

Figure 44 (a) Current-electric field (*I-E*) characteristics of a lateral-structure Pt/$CH_3NH_3PbI_3$/Pt device with various scan rates. (b) Linear *I-E* characteristics of vertical structure Ag/$CH_3NH_3PbI_3$/Pt devices (upper) and lateral structure Pt/$CH_3NH_3PbI_3$/Pt device (bottom). The insets show schematic of the lateral and vertical devices.

With the mechanical flexibility of organolead halide perovskites, we fabricated flexible Ag/$CH_3NH_3PbI_3$/Pt devices on a cyclo-olefin polymer (COP) substrate to demonstrate performance-equivalent to the device on a rigid substrate-of the flexible resistive switching device (Figure 45a).[20, 42] The electrical properties of the flexible devices were measured under tensile-bent states with 5 and 7.5 mm radii of curvature (Figure 45b).

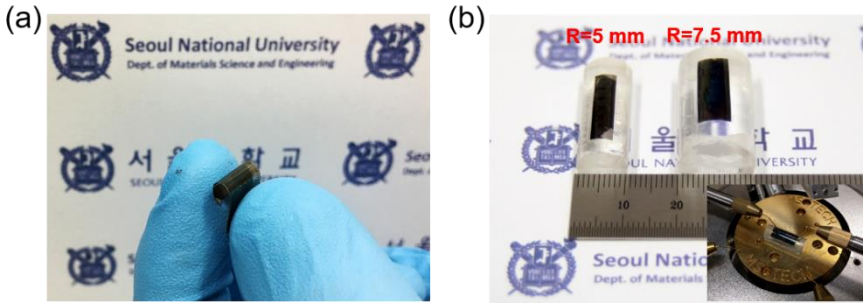

Figure 45 (a) Photograph of a fabricated organolead halide perovskite resistive switching device on a Pt deposited cyclo-olefin polymer substrate. (b) Photograph showing bended states of device. Bending radii were 5 mm (left) and 7.5 mm (right). (inset: photograph of measuring device with a bent state)

To identify the uniformity of the $CH_3NH_3PbI_3$ thin film on the COP substrate, we measured the *I-V* characteristics of ten Ag/$CH_3NH_3PbI_3$/Pt cells under tensile bending states with a 5 mm radius of curvature. Since the device in the bent state shows slightly different electrical properties, we applied different SET/RESET voltages to optimize the operating conditions. With the applied voltage sweep of 0 V → +0.4 V → 0 V → –0.6 V → 0 V, the flexible Ag/$CH_3NH_3PbI_3$/Pt cells showed *I-V* characteristics that are nearly equivalent to the *I-V* characteristics of the devices on the rigid substrate (Figure 46a). Resistive switching with voltage pulses was also possible for the flexible devices. The flexible Ag/$CH_3NH_3PbI_3$/Pt devices recorded 836 (R = 7.5 mm, Figure 46b) and 452 (R = 5 mm, Figure 46c) cycles with a SET voltage of +0.4 V (50 ms pulse width) and RESET voltage of –0.6 V (100 ms pulse width). However, the mechanical stability was not particularly good because the Pt bottom electrode is brittle and fragile.

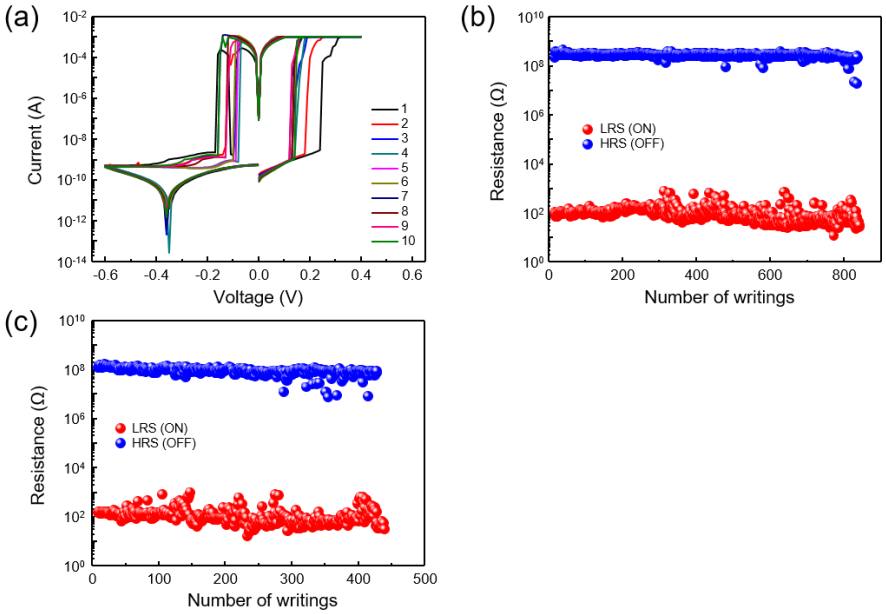

Figure 46 Resistive switching performance of flexible device with the smooth $CH_3NH_3PbI_3$ thin film. (a) Typical current-voltage (*I-V*) characteristics of flexible device with bending stress (a bending radius of 5 mm). Reversible resistive switching measured with SET voltage of + 0.4 V and RESET voltage of – 0.6 V. The pulse widths of the writing voltage were 50 ms (SET) and 100 ms (RESET). Bending radiuses were (b) 7.5 and (c) 5 mm.

3.4. Conclusion

In conclusion, we demonstrated resistive switching devices using an organolead halide perovskite on rigid and flexible substrates. With a suitable amount of the hydroiodic acid additive, morphologically improved solution-processed 300 nm thick smooth $CH_3NH_3PbI_3$ films with Ag top and Pt bottom electrodes exhibited electroforming-free resistive switching with over 1300 cycles of endurance and high ON/OFF ratios of ~10^6 under +0.3 V and –0.7 V pulses. Using the improved solution process, a flexible resistive switching device was achieved with an extremely low bending radius of 5 mm. According to the electrical properties at various temperatures, the SCLC and thermal-assisted hopping mechanism in HRS and ohmic conduction in LRS resulted from the unique electrical properties of the organolead halide perovskite. Moreover, the migration of Ag ions from the top electrode contributes to the formation of the conducting filament. However, improvements in retention time and nanosecond-level operation speed are also necessary and can be established by the control of crystallinity and compositional uniformity in fabrication processes of the OHP films. We believe that organolead halide perovskite memories have potential for high-speed operation and as mechanically stable flexible devices with flexible electrodes based on improved fabrication processes. The various combinations and unique structural flexibility for the lead-free ABX_3-type will contribute to maximizing the performance of environment-friendly organometal halide perovskite devices. Finally, we

believe that organometal halide perovskite materials are promising materials for low-cost low-power consumption flexible memories.

3.5. References

1. Unger, E. L.; Hoke, E. T.; Bailie, C. D.; Nguyen, W. H.; Bowring, A. R.; Heumüller, T.; Christoforo, M. G.; McGehee, M. D., *Energy Environ. Sci.* **2014,** *7* (11), 3690-3698.
2. Mitzi, D. B.; Wang, S.; Feild, C. A.; Chess, C. A.; Guloy, A. M., *Science* **1995,** *267* (5203), 1473-1476.
3. Mitzi, D. B.; Chondroudis, K.; Kagan, C. R., *Inorg. Chem.* **1999,** *38* (26), 6246-6256.
4. Jeon, N. J.; Noh, J. H.; Yang, W. S.; Kim, Y. C.; Ryu, S.; Seo, J.; Seok, S. I., *Nature* **2015,** *517* (7535), 476-480.
5. Eperon, G. E.; Stranks, S. D.; Menelaou, C.; Johnston, M. B.; Herz, L. M.; Snaith, H. J., *Energy Environ. Sci.* **2014,** *7* (3), 982-988.
6. Yin, W. J.; Shi, T. T.; Yan, Y. F., S*J. Phys. Chem. C* **2015,** *119* (10), 5253-5264.
7. Yin, W.-J.; Shi, T.; Yan, Y., *Appl. Phys. Lett.* **2014,** *104* (6), 063903.
8. Eames, C.; Frost, J. M.; Barnes, P. R.; O'Regan, B. C.; Walsh, A.; Islam, M. S., *Nat. Commun.* **2015,** *6*, 7497.
9. Uberuaga, B. P.; Vernon, L. J., *Solid State Ionics* **2013,** *253*, 18-26.
10. Xing, G. C.; Mathews, N.; Sun, S. Y.; Lim, S. S.; Lam, Y. M.; Gratzel, M.; Mhaisalkar, S.; Sum, T. C., *Science* **2013,** *342* (6156), 344-347.
11. Xiao, Z.; Yuan, Y.; Shao, Y.; Wang, Q.; Dong, Q.; Bi, C.; Sharma, P.; Gruverman, A.; Huang, J., *Nat. Mater.* **2015,** *14* (2), 193-198.

12. Kim, H. S.; Lee, C. R.; Im, J. H.; Lee, K. B.; Moehl, T.; Marchioro, A.; Moon, S. J.; Humphry-Baker, R.; Yum, J. H.; Moser, J. E.; Gratzel, M.; Park, N. G., *Sci. Rep.* **2012,** *2*, 591.

13. Burschka, J.; Pellet, N.; Moon, S.-J.; Humphry-Baker, R.; Gao, P.; Nazeeruddin, M. K.; Grätzel, M., *Nature* **2013,** *499* (7458), 316-319.

14. Liu, M.; Johnston, M. B.; Snaith, H. J., *Nature* **2013,** *501* (7467), 395-398.

15. Kim, Y. H.; Cho, H.; Heo, J. H.; Kim, T. S.; Myoung, N.; Lee, C. L.; Im, S. H.; Lee, T. W., *Adv. Mater.* **2015,** *27* (7), 1248-1254.

16. Veldhuis, S. A.; Boix, P. P.; Yantara, N.; Li, M.; Sum, T. C.; Mathews, N.; Mhaisalkar, S. G., *Adv. Mater.* **2016,** *28* (32), 6804-6834.

17. Dong, Y.; Gu, Y.; Zou, Y.; Song, J.; Xu, L.; Li, J.; Xue, J.; Li, X.; Zeng, H., *Small* **2016,** *12* (40), 5622-5632.

18. Kwon, K. C.; Hong, K.; Van Le, Q.; Lee, S. Y.; Choi, J.; Kim, K. B.; Kim, S. Y.; Jang, H. W., *Adv. Funct. Mater.* **2016,** *26* (23), 4213-4222.

19. Yoo, E. J.; Lyu, M.; Yun, J. H.; Kang, C. J.; Choi, Y. J.; Wang, L., *Adv. Mater.* **2015,** *27* (40), 6170-6175.

20. Gu, C.; Lee, J. S., *ACS Nano* **2016,** *10* (5), 5413-5418.

21. Liu, D.; Lin, Q.; Zang, Z.; Wang, M.; Wangyang, P.; Tang, X.; Zhou, M.; Hu, W., *ACS Appl. Mater. Interfaces* **2017,** *9* (7), 6171-6176.

22. Yan, K.; Chen, B.; Hu, H.; Chen, S.; Dong, B.; Gao, X.; Xiao, X.; Zhou, J.; Zou, D., *Adv. Electron. Mater.* **2016,** *2* (8), 1600160.

23. Xiao, Z.; Huang, J., *Adv. Electron. Mater.* **2016,** *2* (7), 1600100.

24. Xu, W.; Cho, H.; Kim, Y. H.; Kim, Y. T.; Wolf, C.; Park, C. G.; Lee, T. W., *Adv. Mater.* **2016,** *28* (28), 5916-5922.

25. Choi, J.; Park, S.; Lee, J.; Hong, K.; Kim, D. H.; Moon, C. W.; Park, G. D.; Suh, J.; Hwang, J.; Kim, S. Y., *Adv. Mater.* **2016,** *28* (31), 6562-6567.

26. Wang, L.; Yang, C.-H.; Wen, J., *Electron. Mater. Lett.* **2015,** *11* (4), 505-543.

27. Zhang, W.; Pathak, S.; Sakai, N.; Stergiopoulos, T.; Nayak, P. K.; Noel, N. K.; Haghighirad, A. A.; Burlakov, V. M.; deQuilettes, D. W.; Sadhanala, A.; Li, W.; Wang, L.; Ginger, D. S.; Friend, R. H.; Snaith, H. J., *Nat. Commun.* **2015,** *6*, 10030.

28. Stoumpos, C. C.; Malliakas, C. D.; Kanatzidis, M. G., *Inorg. Chem.* **2013,** *52* (15), 9019-9038.

29. Xiao, M.; Huang, F.; Huang, W.; Dkhissi, Y.; Zhu, Y.; Etheridge, J.; Gray-Weale, A.; Bach, U.; Cheng, Y. B.; Spiccia, L., *Angew. Chem. Int. Ed.* **2014,** *53* (37), 9898-9903.

30. Jeon, N. J.; Noh, J. H.; Kim, Y. C.; Yang, W. S.; Ryu, S.; Seok, S. I., *Nat. Mater.* **2014,** *13* (9), 897-903.

31. Guloy, A., *Chem. Commun.* **1997,** *0* (7), 697-698.

32. Waser, R.; Dittmann, R.; Staikov, G.; Szot, K., *Adv. Mater.* **2009,** *21* (25-26), 2632-2663.

33. Aoki, Y.; Wiemann, C.; Feyer, V.; Kim, H.-S.; Schneider, C. M.; Ill-Yoo, H.; Martin, M., *Nat. Commun.* **2014,** *5*, 3473.

34. Xue, W.; Xiao, W.; Shang, J.; Chen, X.; Zhu, X.; Pan, L.; Tan, H.; Zhang, W.; Ji, Z.; Liu, G., *Nanotechnol.* **2014,** *25* (42), 425204.

35. Sanehira, E. M.; Tremolet de Villers, B. J.; Schulz, P.; Reese, M. O.; Ferrere, S.; Zhu, K.; Lin, L. Y.; Berry, J. J.; Luther, J. M., *ACS Energy Lett.* **2016,** *1* (1), 38-45.

36. Waser, R., Nanoelectronics and Information Technology : Advanced Electronic Materials and Novel Devices. 3rd ed. *Wiley-VCH: Weinheim*, **2012**, 696-700 .

37. Yoo, E.; Lyu, M.; Yun, J.-H.; Kang, C.; Choi, Y.; Wang, L., *J. Mat. Chem. C* **2016,** *4* (33), 7824-7830.

38. Sun, J.; Liu, Q.; Xie, H.; Wu, X.; Xu, F.; Xu, T.; Long, S.; Lv, H.; Li, Y.; Sun, L., *Appl. Phys. Lett.* **2013,** *102* (5), 053502.

39. Gao, S.; Song, C.; Chen, C.; Zeng, F.; Pan, F., *J. Phys. Chem. C* **2012,** *116* (33), 17955-17959.

40. Wei, Z.; Takagi, T.; Kanzawa, Y.; Katoh, Y.; Ninomiya, T.; Kawai, K.; Muraoka, S.; Mitani, S.; Katayama, K.; Fujii, S. Electron Devices Meeting (IEDM), 2011 IEEE International **2011**, 31.4. 1-31.4. 4.

41. Snaith, H. J.; Abate, A.; Ball, J. M.; Eperon, G. E.; Leijtens, T.; Noel, N. K.; Stranks, S. D.; Wang, J. T.; Wojciechowski, K.; Zhang, W., *J. Phys. Chem. Lett.* **2014,** *5* (9), 1511-1515.

42. Yoon, J.; Sung, H.; Lee, G.; Cho, W.; Ahn, N.; Jung, H. S.; Choi, M., *Energy Environ. Sci.* **2017,** *10* (1), 337-345.

Chapter 4

Reliable RS memory with 2-dimensional layered HPs

Quote

Edsger W. Dijkstra “Simplicity is prerequisite for reliability.” (1975)

4.1. Introduction

Organic–inorganic halide perovskite (OHP) comprising mono-valent organic cation in the A-site and divalent inorganic cation in the B-site in ABX_3 (X = halide) has attracted consider-able attention since the first report describing a long-term durable and high-efficiency solid-state perovskite solar cell in 2012,[1] because of its unprecedented optoelectronic properties. The superb photovoltaic property is related to the intrinsic physico-chemical properties of OHP such as a large absorption coefficient together with micrometer scale long charge diffusion length,[2, 3] and low exciton binding energies.[4]

A facilely tunable band gap and mechanical bendability are its advantages over brittle oxide perovskite, and low temperature processing of OHP is beneficial to flexible electronics. More interestingly, OHP was found to be versatile beyond photo-voltaics in applications such as light emitting didodes,[5, 6] lasing,7 and X-ray imaging.[8]

Recently, the application of OHP was extended to semi-conductor devices including field-effect-transistors,[9] artificial synaptic devices,[10] and non-volatile resistive memories,[11–16] where OHP is a potential alternative to conventional materials for resistive random access memory (ReRAM) due to millivolt-scale low switching voltage and a high on/off ratio. Currently, the most highly studied OHPs are 3-dimensional (3D) $MAPbI_3$,[11–13] $MAPbI_{3-x}Cl_x$,[14, 15] $MAPbBr_{3-x}I_x$,[16] and $CsPbBr_3$.[17] They demonstrated an ON/OFF ratio as high as 10^6, which indicates multi-level resistive switching behavior. Recently, across bay array of $MAPbI_3$ for high-density nanoscale devices was realized.[18] However, 3D OHP-based memory devices still display poor reliability and

stability as compared to resistive memories based on metal oxides such as TiO_{2-x}[19] or HfO_x.[20] The resistive switching occurs as a consequence of formation and rupture of conductive filaments in an insulating layer associated with the nano-ionic motion of electric-field-driven charged defects.[21] Ohmic conduction is usually observed in the low resistance state (LRS) after a sharp increase in current is evidenced by direct observation of the localized nano-scale conducting process under an electric field using conductive atomic force microscopy (C-AFM)[11] and transmission electron microscopy (TEM).[22] In the resistive switching process, it was discovered that it was difficult to control the shape, uniformity, and strength of the conducting filament in oxide-based materials.[23] An uncontrollable conducting pathway in 3D OHP might be related to poor endurance and retention.

We have been interested in 2-dimensional (2D) OHP as a reliable and stable material for ReRAM because of its anisotropic nature. As compared to 3D OHP in Figure. 47, the reduced random migration of charged defects expected in the 2D-layered OHP could be beneficial for formation and rupture of a conducting filament because defects caused by iodide vacancies are distributed in the intralayer of the 2D structure as compared to 3-dimensionally distributed vacancies in 3D OHP. It is noted that the dimensionality can be controlled by interlayer organic molecules and the number of inorganic intralayers.[24]

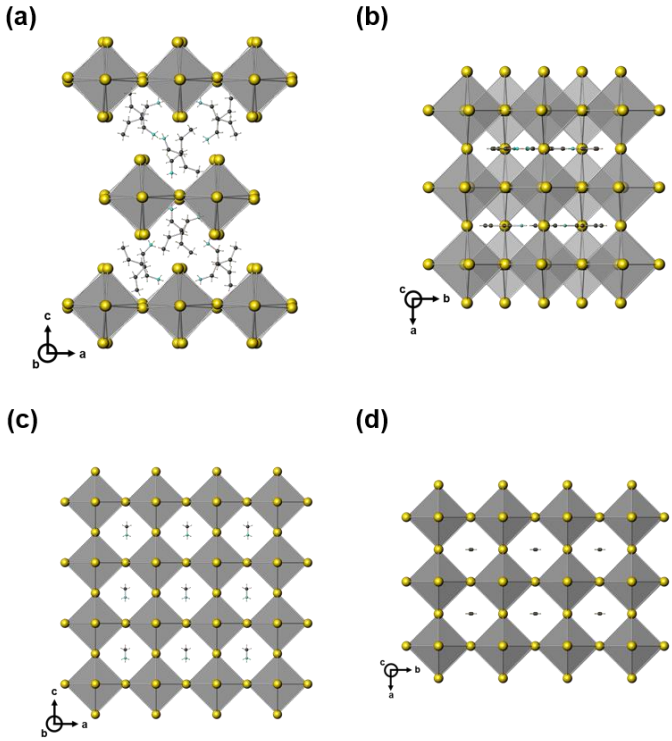

Figure 47 Comparison of crystalline structures of 2D BA_2PbI_4 and 3D $MAPbI_3$ (BA = $C_4H_9NH_3$ and MA = CH_3NH_3). (a, c) Cross-sectional and (b, d) top view of (a, b) BA_2PbI_4 and (c, d) $MAPbI_3$.

Here, I report the resistive switching of $(C_4H_9NH_3)_2(CH_3NH_3)_{n-1}Pb_nI_{3n+1}$ ($C_4H_9NH_3$= BA, CH_3NH_3= A) from n=1 to 3 and n=∞ to study the dependency of resistive switching on the structural change from 3D OHP ($MAPbI_3$) to 2D layered OHP (BA_2PbI_4). The interlayer BA cation has a chain sufficiently long to separate inorganic intralayers comprising PbI_6 octahedra, whereas the small MA cation can be inserted in PbI_6 octahedra to increase 3D characteristics. The resistive switching property is compared to study the effect of dimensionality on resistive switching behavior. Consequently, 2D OHP is found to be more reliable and stable in the switching process than quasi 2D and 3D OHPs. I also

demonstrate the uniformity of the resistive switching properties using 4 inch wafer-scale BA_2PbI_4 thin film.

4.2. Experimental Procedures

Synthesis: $C_4H_9NH_3I$ (butylammonium iodide, BAI) was synthesized by reacting 10ml of $C_4H_9NH_2$ (Aldrich, 99%) with 20 ml of HI (Aldrich, 57 wt % in H_2O). The $C_4H_9NH_2$ solution was placed in a round-bottom flask with magnetic stirring where a HI solution was added dropwise. The reaction proceeded in an ice bath for 2 h. The white precipitate was collected by evaporation sing a rotary evaporator at 60 ^oC. The collected white precipitate was washed with diethyl ether three times. Finally it filtered and dried for 24 h in vacuum oven at 60 ^oC. CH_3NH_3I (methylammonium iodide, MAI) was synthesized by reacting 30 ml of CH_3NH_2 (TCI, 40 wt % in methanol) with 40 ml of HI (Aldrich, 57 st % in H_2O). The following steps were same as that of butylammonium iodide as demonstrated.

Fabrication: The silicon wafer coated by 100 nm of Pt was cleaned by ultrasonication in detergent, ethanol, acetone and ethanol bath for each 15 min. It was treated with UV-ozone for 15 min before spin-coating of the perovskite precursor solution. The $BA_2MA_{n-1}Pb_nI_{3n+1}$ precursor solution (n=1,2,3) was prepared by dissolving 1 mmol of PbI_2 (Alfa Aesar, 99.999%), x mmol (x=2 for n=1, x=1 for n=2, x=0.66 for n=3) of BAI, y mmol (y=0 for n=1, y=0.5 for n=2, y=0.66 for n=3) of MAI, and 2 mmol of DMSO (Sigma, >99.9%) in 1 ml of DMF (Sigma-Aldrich, 99.8%). $MAPbI_3$ precursor solution was prepared by dissolving 1 mmol of PbI_2 with 1 mmol of MAI in 1 ml of DMF. The solution was spin-coated on the Pt-coated Silicon wafer at 4000 rpm for 40 s. (acceleration = 1200 rpm/s), to which 0.5 ml of chlorobenzene was dropped

after 15 s of spinning (after 10 s for $MAPbI_3$). The spin-coated $BA_2MA_{n-1}Pb_nI_{3n+1}$ film (n=1,2,3) as annealed at 55 °C for 1 min and at 100 °C for 50 min while $MAPbI_3$ was annealed at 70 °C for 50 min. Ag (99.99%) was deposited as electrode using a thermal evaporator at ca. 10^{-6} torr. The size of silicon wafer was 1.5 cm·1.5 cm or 4 inch diameter wafer, however the fabrications were same but we dropping 1 ml of chlorobenzene on the 4 inch-scale wafer coated by perovskite film during spin-coating.

Characterization: The surface and cross sectional images were obtained from field emission scanning electron microscopy(JEOL, JSM7000F) at accelerating voltage of 1 kV. All electrical characteristics were measured by using Keithley 4200 in the vacuum probe station at ca. 10^{-2} torr. The *I-V* characteristics was measured by direct voltage current sweeping mode in various temperature and the resistive switching cycling was measured by direct current voltage pulses (10 ms of pulse width). X-ray diffraction patterns were obtained using a Rigaku DMAX-2200PC X-ray diffractometer equipped with a graphite monochromator (λ = 1.5418 Å). The datasets were collected in the 2θ range of 3–65° with a step size of 0.02°. The lattice parameters were refined using the UnitCell program[38]. The *a* and *b* lattice parameters for the $(BA)_2PbI_4$ sample were taken from the literature[39] because the XRD pattern of $(BA)_2PbI_4$ film prepared in this work showed only (00*l*) reflections.

4.3. Results and Discussion

A schematic of the device's structure is displayed in Figure. 48a, which shows that the device is composed of a Pt bottom electrode (BE), an OHP film, and an Ag top electrode (TE). The OHP film was spin-coated onto the Pt-coated substrate. The 150 nm-thick Ag top electrodes were formed on the surface of the OHP film by thermal evaporation, where a dot-patterned shadow mask with a diameter of 100μm was used. OHP thin films with different dimensionalities were prepared: 2D BA_2PbI_4 (n= 1), quasi 2D films of $BA_2MAPb_2I_7$ (n= 2), $BA_2MA_2Pb_3I_{10}$ (n= 3), and 3D $MAPbI_3$ (n=∞). Figure. 48b shows a cross-sectional scanning electron microscopy (SEM) image of a uniform BA2PbI4 film that was deposited by a one-step solution.

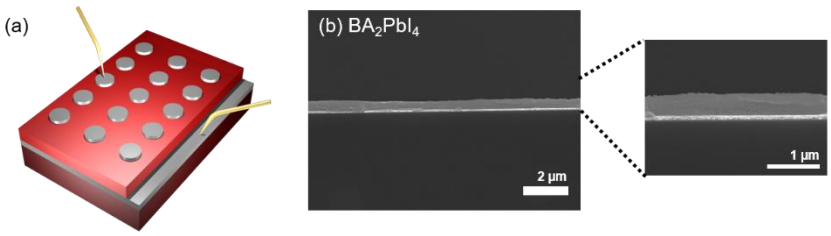

Figure 48 (a) Schematic device structure of Ag/$BA_2MA_{n-1}Pb_nI_{3n+1}$/Pt/Ti/SiO_2/Si. (b) SEM images for thin film BA_2PbI_4 on the silicon substrate coated by 100 nm of Pt.

Pinhole-free thin films for all the studied compositions were confirmed to be pinhole free (Figure. 49).

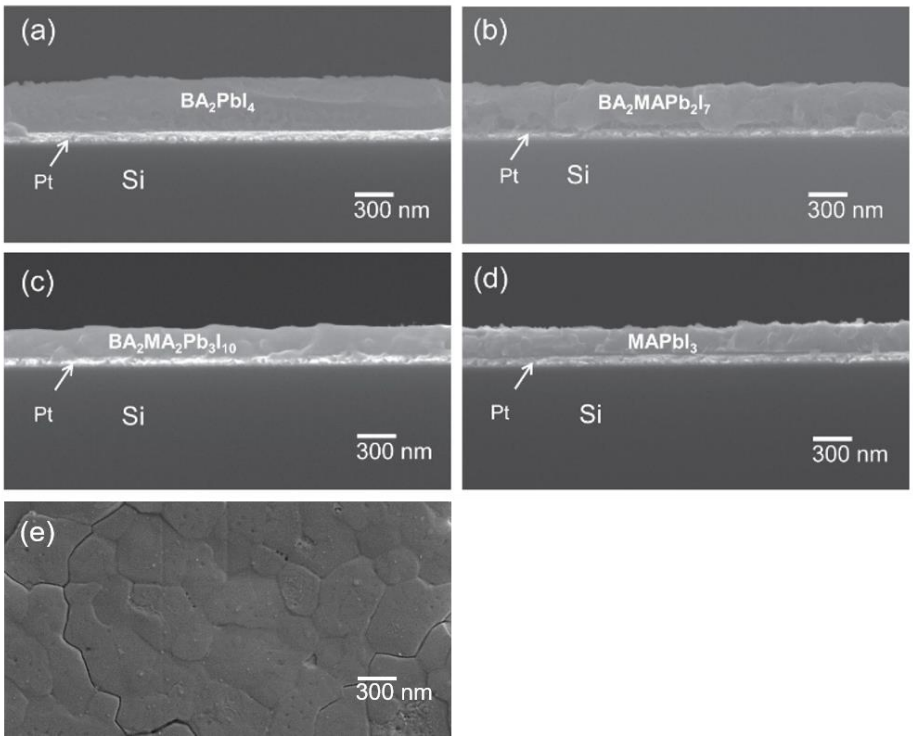

Figure 49 Cross-sectional scanning electron microscopy images for (a) BA_2PbI_4, (b) $BA_2MAPb_2I_7$, (c) $BA_2MA_2Pb_3I_{10}$ and (d) $MAPbI_3$. (e) Plane-view scanning electron microscopy image for BA_2PbI_4. The OHP thin films formed on the Pt coated silicon wafer.

According to the comparative study of the observed and calculated X-ray diffraction (XRD) patterns, all the measured XRD patterns are consistent with both a previous report24 and the calculated XRD patterns (Figure. 50a–d). For BA_2PbI_4, (00l) reflections are exclusively developed, which is indicative of the preferred orientation along the 2D perovskite slab.[24] For $BA_2MAPb_2I_7$ and $BA_2MA_2Pb_3I_{10}$, the predominant (0k0) reflections are also indicative of anisotropic growth of these phases on the substrate. The (0k0) planes for n=2–

4 in $(BA)_2(MA)_{n-1}Pb_nI_{3n+1}$ are parallel to the perovskite slabs, and they correspond to the (00l) reflection for n=1.24

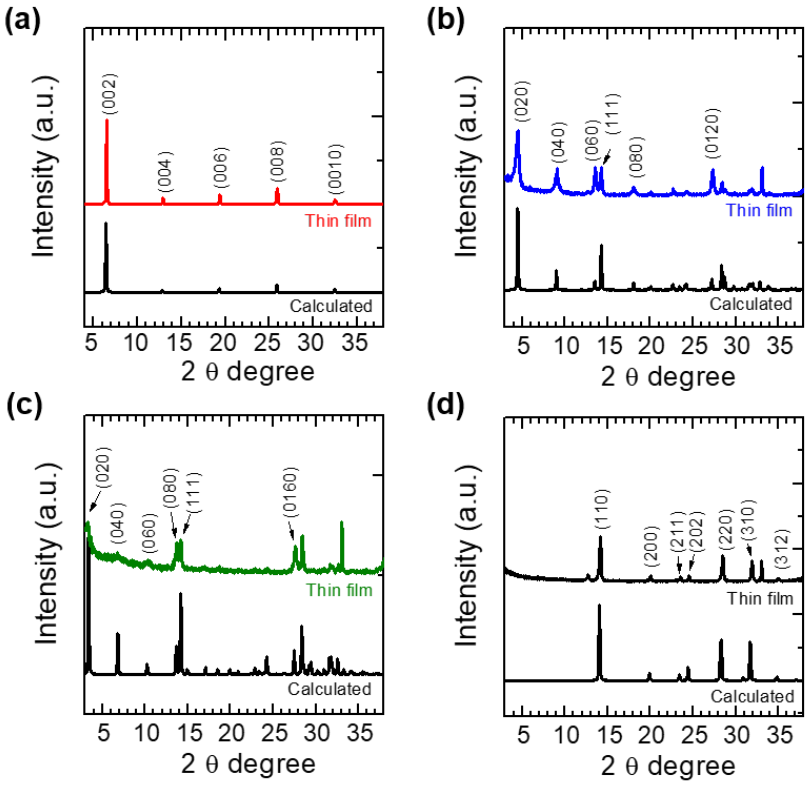

Figure 50 XRD peaks reveals the perovskite formation in (a) BA_2PbI_4, (b) $BA_2MAPb_2I_7$, (c) $BA_2MA_2Pb_3I_{10}$ and (d) $MAPbI_3$.

Figure. 51a–d show the *I–V* characteristics measured under a direct current (DC) voltage sweep. Regardless of the dimensionality of the materials, all the OHPs show bipolar resistive switching behavior. The high resistance state (HRS) is changed to a low resistance state (LRS) at a certain positive bias with an abrupt increase in current (SET process). The devices maintain LRSs beyond the SET voltages, and the abrupt SET process and high ON/OFF ratios clearly suggest the formation of conducting filaments. When negative bias is applied to the

devices, LRSs undergo complete transformation into HRSs (RESET process), supporting the disruption of the conducting pathways. The compliance current was 10^{-2} A and 10^{-1} A for the SET and RESET processes, respectively. It is noted here that the SET voltage decreases as the dimensionality changes from 3D to 2D. We also investigated the initial forming process.

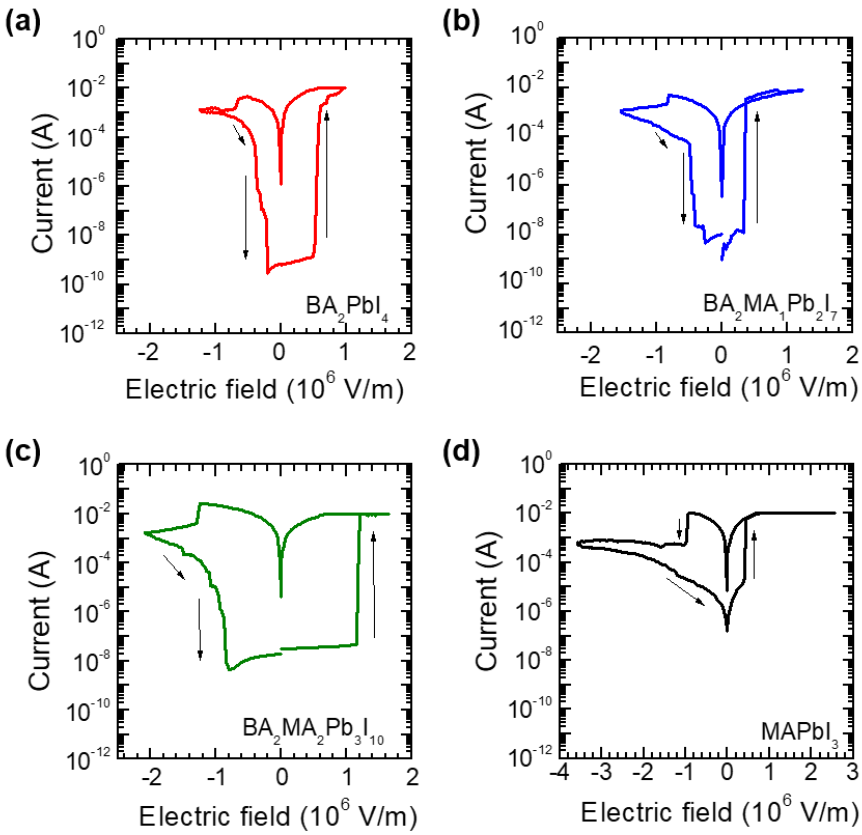

Figure 51 *I-V* characteristics of (a) BA_2PbI_4, (b) $BA_2MAPb_2I_7$, (c) $BA_2MA_2Pb_3I_{10}$, (d) $MAPbI_3$.

In Figure. 52, *I–V* curves show little difference in switching voltage and process between forming and the SET process, which indicates that 2D-layered OHP and quasi-2D OHP enable the electroforming-free process.

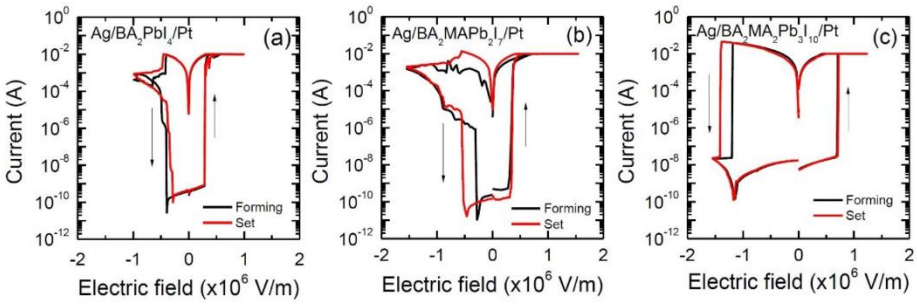

Figure 52 *I-V* curves for forming process and set process for (a) Ag/BA_2PbI_4/Pt, (b)Ag/BA_2MAPb_2I7/Pt, (c)Ag/$BA_2MA_2Pb_3I_{10}$/Pt. All *I-V* curves measured at one electrode and showed electroforming-free process.

Figure. 53a compares the SET voltage, represented by electric field (E), where the average film thickness estimated from the cross-sectional SEM images (Figure. 49) was 404.5 nm for BA_2PbI_4, 324.1 nm for $BA_2MAPb_2I_7$, 241.1 nm for $BA_2MA_2Pb_3I_{10}$, and 195.5 nm for $MAPbI_3$. The average electric field for the SET process was found to be 0.47 × 10^6, 0.52×10^6, and 0.45 × 10^6 V/m for $MAPbI_3$, $BA_2MA_2Pb_3I_{10}$, and $BA_2MAPb_2I_7$, respectively, whereas BA_2PbI_4 switches on the device at the relatively lower SET electric field of 0.25 × 10^6 V/m. For the $MAPbI_3$, the measured electric field for the SET process is comparable to the reported values (0.325 × 10^6 V/m).11 The low operating electric field observed from BA_2PbI_4 indicates that the SET and RESET processes could be easier in a 2D-layered structure than 3D or quasi 2D structures. The ON/OFF ratio is compared in Figure. 53b, where BA_2PbI_4 and $BA_2MAPb_2I_7$ demonstrate an ON/OFF ratio as high as approximately 10^7, whereas the ON/OFF ratio is decreased to approximately 10^5 in $BA_2MA_2Pb_3I_{10}$ and approximately 10^2 in $MAPbI_3$. This indicates that the ON/OFF ratio tends to increase as the dimensionality decreases from 3D to 2D.

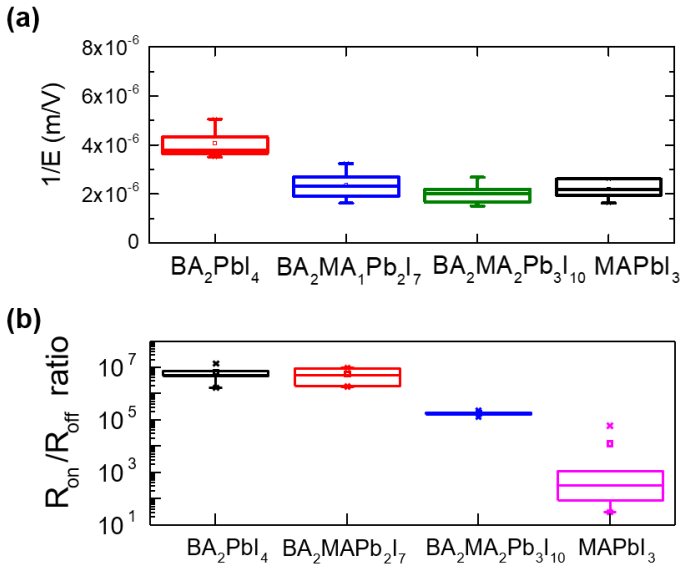

Figure 53 (a) The electric field for SET process was compared, the lowest electric field was observed in BA_2PbI_4. (b) the on/off ratio each material (Reading voltage was 0.02 V).

To understand the origin of the resistive switching behavior, we plot logarithmic *I–V* characteristics of the devices (Figure. 54a–c). Because $MAPbI_3$ is found to be highly sensitive to environmental conditions such as humidity and oxygen and thereby it exhibits relatively unstable resistive switching behavior, the switching performance is compared for BA_2PbI_4, $BA_2MAPb_2I_7$, and $BA_2MA_2Pb_3I_{10}$. In Figure. 54a–c, the LRS is fitted with slope = 1 for all the samples, which indicates that a conducting filament is formed during the SET process.[28, 29] However, voltage-independent current is exhibited at the HRS, which is indicative of non-flow of internal electric charges. This result supports the tenet that the conduction path or underlying mechanism is similar regardless of the structural dimensionality. The current at the HRS decreases from

approximately 10^{-8} to 10^{-10} and to 10^{-11} A as the dimensionality is reduced from quasi 2D (n= 3 and n=2) to 2D (n= 1). Thus, the increased ON/OFF ratio in 2D BA_2PbI_4 is attributed to the significant decrease in the HRS current rather than a slight change in the LRS current.

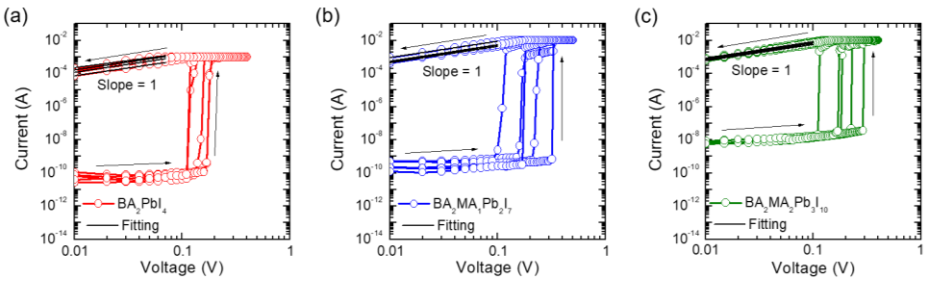

Figure 54 Fitted logarithmic *I-V* characteristics of (a) BA_2PbI_4, (b) $BA_2MA_1Pb_2I_7$, (c) $BA_2MA_2Pb_3I_{10}$.

It was reported that change in dimensionality from 3D $MAPbI_3$ to 2D BA_2PbI_4 enlarged the bandgap along with changes in valence band maximum and conduction band minimum,[24] which might lead to the different Schottky barrier heights at the interface of both of the TE Ag and the BE Pt. We calculated the Schottky barrier heights from the difference between the work function of the metal electrode and the Fermi level of perovskite (assuming that it is an intrinsic semiconductor) and found that BA_2PbI_4 shows the highest barrier at both sides of the interfaces because of its wider bandgap (Figure. 55). The increase in barrier height as the dimensionality shifts from 3D to 2D is likely to decrease the density of the injected carrier from electrode to perovskite, which can explain the decrease in the HRS current traveling from quasi 2D to 2D, as observed in Figure. 54a–c.

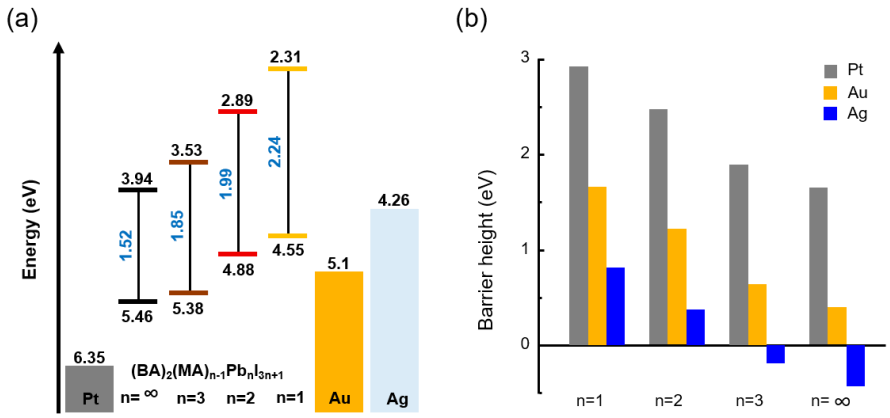

Figure 55 (a) Energy band diagram and (b) Schottky barrier heights at each metal electrode interface calculated by difference between the Fermi level of $(BA)_2(MA)_{n-1}Pb_nI_{3n+1}$ and work function of metal.

We examined the effect of temperature on the electrical characteristics of the HRS over temperatures ranging from 150 K to 360 K to study further differences in OFF current at the HRS depending upon dimensionality. In Figure. 54a–c, resistance at the HRS (R_{off}) is decreased as the temperature increases, which is indicative of semiconductor-like behavior. To understand the temperature-dependent semiconducting behavior of our perovskite samples, an Arrhenius plot of the HRS current (I_{off}) as a function of inverse temperature was created, which is displayed in the insets of Figure. 54a–c. The electrical thermal activation energy (E_a) is estimated using equation (1),

$$\ln I_{off} = \ln I_0 - {}^{E_a}/_{kT}$$

Where I_{off} is the HRS current, I_0 is the constant, k is the Boltzmann constant, and T is the absolute temperature.[30] Two distinct E_a values are obtained from the plots for each sample. In the low temperature region, E_a= 0.047, 0.053, and

0.085 eV are estimated for $BA_2MA_2Pb_3I_{10}$, $BA_2MA_1Pb_2I_7$, and BA_2PbI_4, respectively, while a larger E_a of 0.185, 0.190, and 0.583 eV is evaluated for higher temperatures. This indicates that all the samples have low E_a values below room temperature but show high E_a values near and above room temperature. In addition, E_a is increased upon reducing the dimensionality from quasi 2D to 2D. E_a is related to the donor level (trap state) at the conduction band, and deeper trap states tend to increase E_a at the HRS and thereby decrease the OFF current.

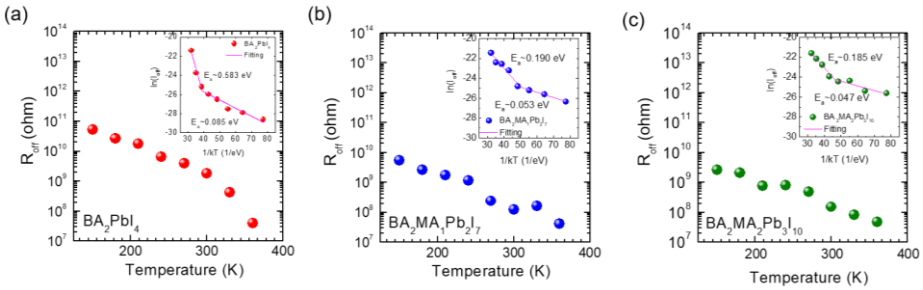

Figure 56 Temperature dependent resistance of (a) BA_2PbI_4, (b) $BA_2MA_1Pb_2I_7$, (c) $BA_2MA_2Pb_3I_{10}$. The decreased resistance as temperature increased showed the typical semiconductor property. In insert figure, two distinguish slope was determined from $In(I_{off})$-1/kT plot. It result as two different dominant conducting mechanism, and highest thermal electronic activation energy was observed in BA_2PbI_4 in range of T>300 K.

When considering that the metallic filament is broken in the HRS, the small current can be explained by thermally excited electrons hopping via the shallow trap states at high temperatures.[31] E_a is thus related to the donor level (trap state) at the conduction band, and deeper trap states tend to increase E_a at the HRS and thereby decrease the OFF current. The increase in E_a at high temperatures

as the dimensionality reduces from quasi 2D to 2D is ascribed to the deeper trap states associated with the larger band gap and higher conduction band minimum. Therefore, higher Schottky barrier heights and E_a are responsible for the smaller OFF current and higher ON/OFF ratio for 2D BA_2PbI_4.

Regarding the filament formation mechanism in BA_2PbI_4, it is unclear, but iodide migration (or iodide vacancy) is assumed to be dominantly involved such as that in $MAPbI_3$, as evidenced by X-ray photoelectron spectroscopy (XPS) study.[32] Because both mechanisms of the Ag redox reaction and vacancy migration can be possible when using an Ag electrode, it is interesting to investigate whether or not switching at different electrodes occurs. However, there is no resistive switching response in the Au/BA_2PbI_4/Pt device even under an electric field that is 3 times higher compared to Ag/BA_2PbI_4/Pt (Figure. 57), which indicates that electrochemical metallization (ECM) by Ag redox reaction could be dominant in 2D OHP. Nevertheless, it is uncertain whether ECM is involved because of the lower electric field for the SET ($<10^6$ V/m) that exists as compared to the high electric field ($>10^7$ V/m) required for ECM. Further studies are required to clarify the filament formation mechanism that occurs with 2D OHP.

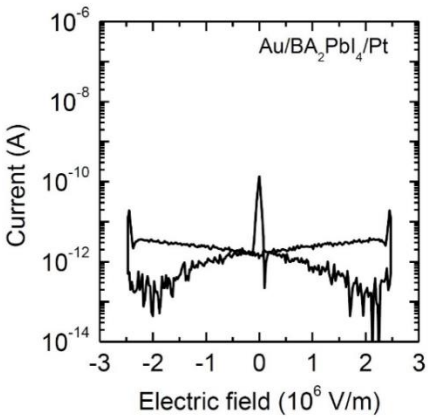

Figure 57 *I-V* curve of Au/BA_2PbI_4/Pt device. The electric field was applied from positive sweeping to negative sweeping.

Device reliability was determined by the stability and number of switching cycles. Figure. 58 shows the endurance characteristics for BA_2PbI_4 ,$BA_2MA_1Pb_2I_7$, and $BA_2MA_2Pb_3I_{10}$ A direct current (DC) pulse was applied with magnitude of 0.5 V for the SET process and −0.6 V for the RESET process, where the pulse width was 10 ms during more than 250 cycles. It is noted that perfect resistive switching is realized for Ag/BA_2PbI_4/Pt for 250 cycles, while quasi 2D perovskites show relatively unstable switching behavior as the number of cycles increases primarily because of the instability of the HRS. This indicates that the RESET process is critical to determine the reliability of devices rather than the SET process. The resistive switching behavior was reported to be closely related to the shape, uniformity, and dimension of the conducting filament as well as the defect sites caused by the crystallographic structure.[23]

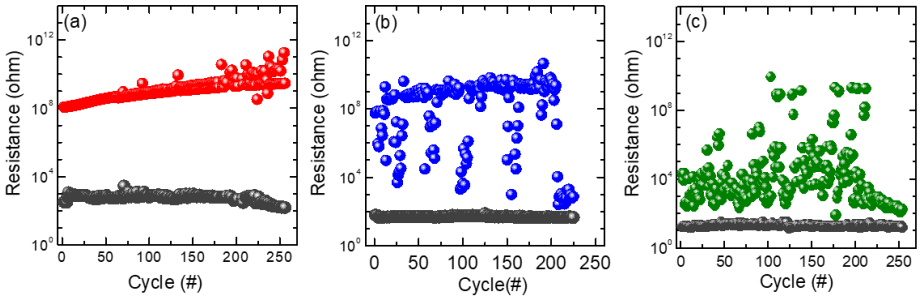

Figure 58 Endurance characteristics of Ag/$BA_2MA_{n-1}Pb_nI_{3n+1}$/Pt, (a) BA_2PbI_4, (b) $BA_2MA_1Pb_2I_7$, (c) $BA_2MA_2Pb_3I_{10}$. SET voltage was 0.5 V and RESET voltage was -0.6 V. (The pulse width was 10 ms). Reading voltage was + 0.02 V/- 0.02 V.

Two types of conducting filaments in bipolar switching memory devices were observed by TEM,22,33 SEM,34 and C-AFM35 – a bulky shape22,35 and a dendrite-like (multiple) shape.33,34 It is expected that the conducting filament is difficult to completely annihilate under the RESET process. The conducting filament is expected to be broken for the rupture process in the case of the bulky shape, and the partially remaining filaments are responsible for the resistance at the HRS. However, after the rupture process, additional residual filaments are expected due to multiple filaments in the dendrite-like shape, which can decrease the resistance at the HRS. Because we observed insulating characteristics at the HRS and a higher ON/OFF ratio approaching the 2D structure, it is likely that the bulky filament shape has formed in our 2D system. A more stable HRS for 2D than quasi 2D in Figure. 58 indicates that residual filaments at the HRS are formed with less frequency for 2D than for quasi 2D.

We also measured the retention behavior to investigate the retention time and resistance. The SET retention shows that 2D-layered and quasi-2D OHP remain unchanged for more than 10^3 s (Figure. 59). However, the LRS resistance decreases from 50 ohm (BA_2PbI_4) to 33 ohm ($BA_2MAPb_2I_7$) and to 27 ohm ($BA_2MA_2Pb_3I_{10}$).

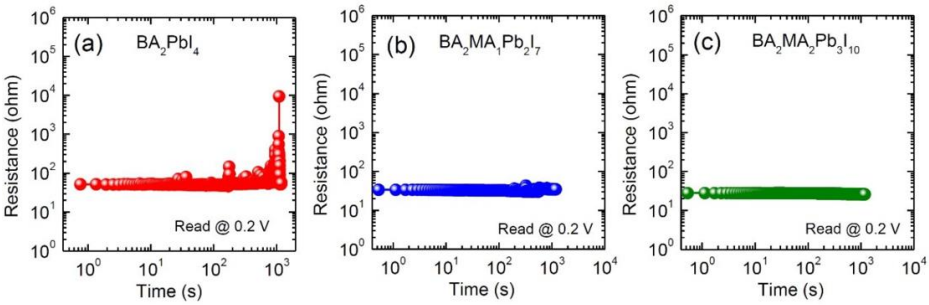

Figure 59 Retention for LRS of (a)Ag/BA_2PbI_4/Pt, (b) Ag/$BA_2MAPb_2I_7$/Pt and (c) Ag/$BA_2MA_2Pb_3I_{10}$/Pt devices. The measured resistances are 50, 33 and 27 ohm for BA_2PbI_4,$BA_2MAPb_2I_7$, and $BA_2MA_2Pb_3I_{10}$, respectively.

Assuming that the conducting filament is cylindrical, a decrease of resistance is indicative of an increase in the radius of the conducting filament with MA content. Therefore, energy and time required for the rupture of the filament will be higher and longer for a larger radius, respectively, which is expected to decrease the stability of the HRS as the MA content increases, i.e., dimensionality increases. Regarding switching stability, we investigated changes in the crystal structure before and after the application of bias voltage. Three different samples for each 2D BA_2PbI_4 and 3D $MAPbI_3$ were prepared: the as-prepared perovskite on the Pt bottom electrode (perovskite/Pt), the as-prepared perovskite sandwiched by the Ag top electrode and the Pt bottom electrode (Ag/perovskite/Pt), and the Ag/perovskite/Pt sample after 10 cycles

of voltage sweeping (one cycle of voltage sweeping consists of: 0.5 V → 0 V→ −0.5 V → 0 V), together with a thin film consisting of a mixture of AgI and perovskite with 0.8 mmol of AgI with respect to 1 mol of perovskite (mixture perovskite/Pt) for comparison. Figure. 60 shows the XRD patterns. The cell volume was calculated from the XRD data to compare the structural changes during voltage sweeping (Table 3). An unknown peak at approximately 8.5° was detected after Ag deposition in BA_2PbI_4 before and after voltage sweeping (Figure. 60a), while no noticeable unknown peaks were found in $MAPbI_3$ (Figure. 60b). This unknown peak is also observed from the mixture of AgI and BA_2PbI_4 but not from the mixture with $MAPbI_3$. This indicates that AgI exists after deposition of the Ag TE and after voltage sweeping for BA_2PbI_4. AgI peaks at approximately 22°, and 24° is less pronounced for both the as-deposited Ag electrode and the mixture, which is pronounced after voltage sweeping. For $MAPbI_3$, AgI is not observed; instead, metallic Ag is detected after Ag deposition and voltage sweeping. From the evolution of XRD, it cannot be ruled out that migration of Ag^+ ion may create a conducting path in 2D BA_2PbI_4.

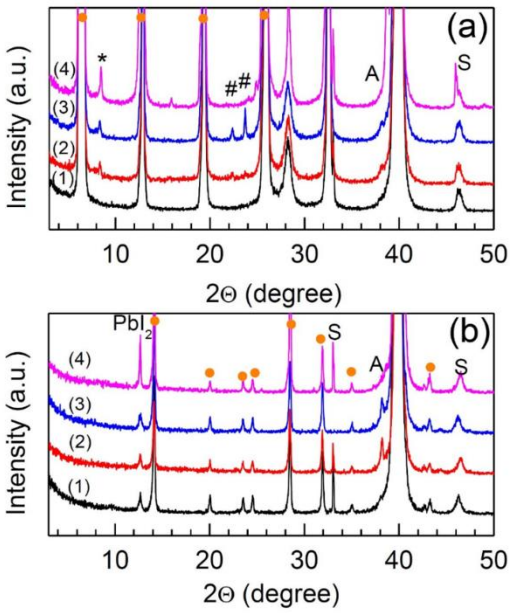

Figure 60 XRD patterns of four different samples for (a) BA_2PbI_4 and (b) $MAPbI_3$, where (1) represents the as-prepared perovskite on Pt electrode (Perovskite/Pt), (2) the as-prepared perovskite with Ag electrode (Ag/perovskite/Pt), (3) the sample after 10 cycles of voltage sweeping (bias aged Ag/perovskite/Pt) and (4) a thin film of mixture of AgI and perovskite with 0.8 mmol of AgI with respect to 1 mol of perovskite (mixture perovskite/Pt). The area of Ag was 0.09 cm2 with the thickness of 150 nm. The voltage sweeping cycle was 0.5 V →0 V →-0.5V→0 V. The perovskite phase is marked with orange circles. A indicates metallic Ag, # denotes AgI and S corresponds to peak from silicon wafer.* denotes unknown peak.

Sample		a (Å)	b (Å)	c (Å)	V (Å^3)
$MAPbI_3$	Bare	8.8528(7)		12.563(3)	984.6(2)
	Ag	8.8518(7)		12.565(3)	984.6(2)
	Ag_V	8.8559(7)		12.590(3)	987.4(2)
	AgI_0.8mmol	8.8594(7)		12.575(3)	987.0(2)
BA_2PbI_4	Bare	8.862	8.862	27.509(1)	2116.6(4)
	Ag	8.862	8.862	27.505(1)	2116.2(4)
	Ag_V	8.862	8.862	27.512(1)	2116.8(4)
	AgI_0.8mmol	8.862	8.862	27.615(1)	2124.7(4)

Table 3 Lattice parameters and unit cell volumes of the samples

The unit cell volume was calculated to investigate the impact of applied bias on OHP. The cell volume of $MAPbI_3$ is increased after voltage sweeping, whereas no significant change in cell volume occurred for BA_2PbI_4 (Figure. 61). The improved structural stability of BA_2PbI_4 under repeated voltage sweeping is in part responsible for the improved endurance performance.

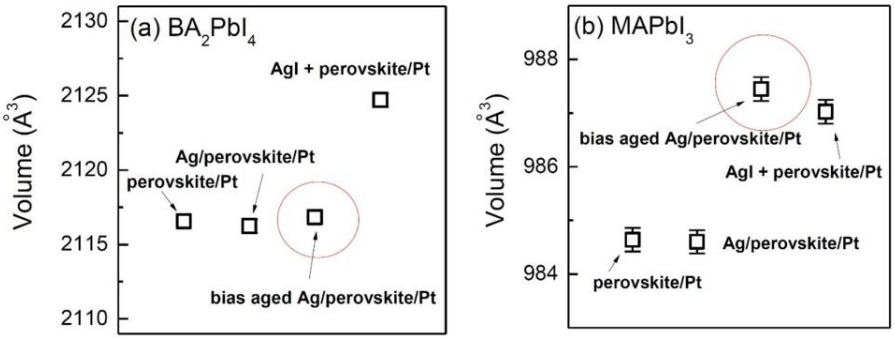

Figure 61 The unit cell volumes of three different samples mentioned in Figure 56 for (a) BA_2PbI_4, and (b) $MAPbI_3$ calculated by lattice parameters listed in Table 3.

To check the feasibility of the 2D OHP for use in a large area scale, we investigated the resistive switching properties of 4 inch wafer-scale BA_2PbI_4 thin films. Figure. 62a shows the BA_2PbI_4 film deposited on a 4 inch wafer,

where the wafer-scale film was prepared by the solution process. Five different areas were chosen, and the resistive switching characteristics were measured. Figure. 62b–d shows the HRS, LRS, and SET voltage, represented by an electric field, where little deviation of each property was found.

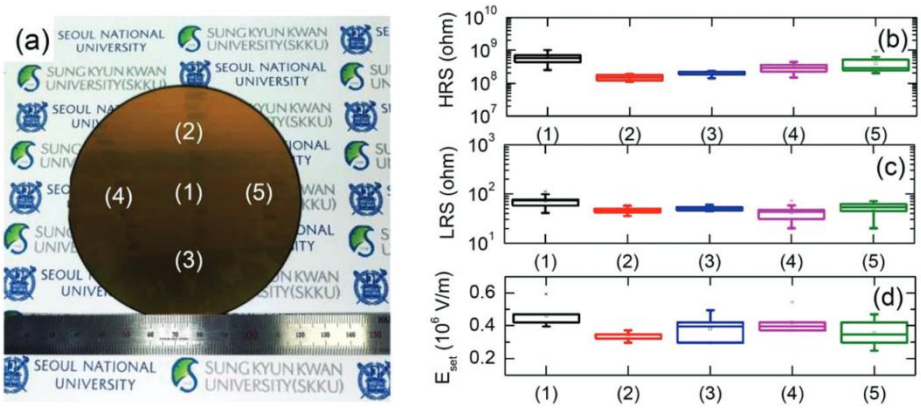

Figure 62 Reliable resistive switching properties of Ag/BA_2PbI_4/Pt prepared on a 4 inch wafer. (a) BA_2PbI_4 was spin-coated on a 4 inch wafer, and Ag electrodes were deposited on locations (1) – (5). (b) HRS, (c) LRS, and (d) SET voltage, represented by electric field (E) on (1) – (5).

The average thickness is found to be 473.4 with deviation of ±30.6 nm (Figure. 63), which is responsible for the small deviation in HRS and LRS. The measured switching properties of the 4 inch wafer are found to be nearly comparable to those of the small-sized device.

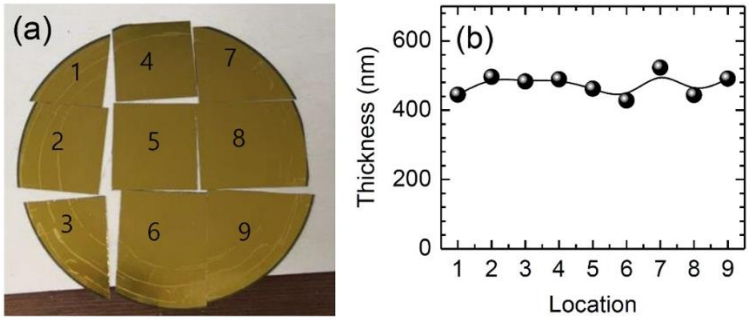

Figure 63 BA_2PbI_4 film deposited on (a) Si wafer and (b) its thickness measured from different part designated in (a).

The reliable switching property of the 4 inch large-scale wafer suggests the feasibility of low-cost and large-area 2D OHP-based resistive memory. Reliability is further confirmed from 20 electrodes at room temperature (Figure. 64a and b). Bipolar switching is observed at the elevated temperature of 87 °C, which is probably related to the non-phase transition of 2D perovskite (Figure 64c). Our data strongly suggests that BA_2PbI_4 is suitable for non-volatile memory, which should be capable of operating at elevated temperatures in a high-density electronic circuit.

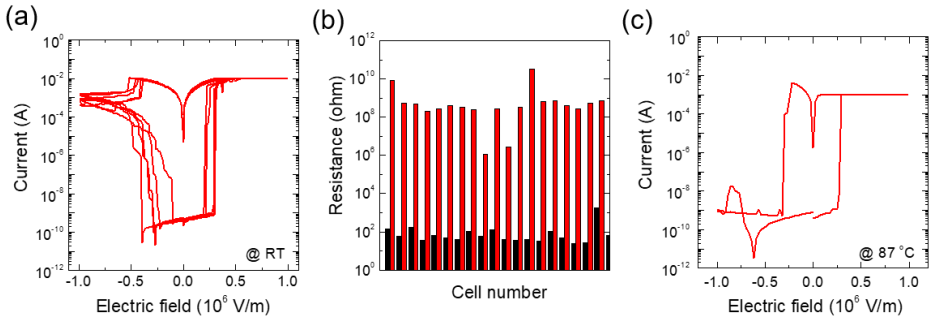

Figure 64 (a) Comparison of *I-V* characteristics from 5 repeated sweeps at room temperature. (b) Distribution of resistances in HRS and LRS was shown (read at 0.02 V). (c) I-V characteristics measured at 87 ºC.

4.4. Conclusion

We prepared and studied the resistive switching behavior of $BA_2MA_{n-1}Pb_nI_{3n+1}$ films for n=1,2,3 and ∞ (2D layered structure for n= 1 and 3D structure for n=∞). The anisotropic 2D structure exhibited a lower operating voltage, higher ON/OFF ratio, and more stable endurance without failure during 250 cycles compared to the quasi 2D and 3D structure. It was confirmed that higher Schottky barrier heights and E_a were responsible for the smaller HRS current and higher ON/OFF ratio for 2D BA_2PbI_4. We obtained for the first time reliable resistive switching from a 4 inch wafer-scale device based on solution-processed BA_2PbI_4. Stable resistive switching behavior was observed even at the elevated temperature of 87 °C. Our results suggest that 2D perovskite is a promising material for a resistive memory device.

4.5. References

1. Kim, H.-S.; Lee, C.-R.; Im, J.-H.; Lee, K.-B.; Moehl, T.; Marchioro, A.; Moon, S.-J.; Humphry-Baker, R.; Yum, J.-H.; Moser, J. E.; Grätzel, M.; Park, N.-G. *Sci. Rep.* **2012**, *2*, srep00591.
2. Filip, M. R.; Eperon, G. E.; Snaith, H. J.; Giustino, F. *Nat. Commun.* **2014**, *5*, ncomms6757.
3. Eperon, G. E.; Stranks, S. D.; Menelaou, C.; Johnston, M. B.; Herz, L. M.; Snaith, H. J. *Energy Environ. Sci.* **2014**, *7* (3), 982–988.
4. Gu, C.; Lee, J.-S. *ACS Nano* **2016**, *10* (5), 5413–5418.
5. Shi, D.; Adinolfi, V.; Comin, R.; Yuan, M.; Alarousu, E.; Buin, A.; Chen, Y.; Hoogland, S.; Rothenberger, A.; Katsiev, K.; Losovyj, Y.; Zhang, X.; Dowben, P. A.; Mohammed, O. F.; Sargent, E. H.; Bakr, O. M. *Science* **2015**, *347* (6221), 519–522.
6. Stranks, S. D.; Eperon, G. E.; Grancini, G.; Menelaou, C.; Alcocer, M. J. P.; Leijtens, T.; Herz, L. M.; Petrozza, A.; Snaith, H. J. *Science* **2013**, *342* (6156), 341–344.
7. Miyata, A.; Mitioglu, A.; Plochocka, P.; Portugall, O.; Wang, J. T.-W.; Stranks, S. D.; Snaith, H. J.; Nicholas, R. J. *Nat. Phys.* **2015**, *11* (7), 582–587.
8. Yuan, M.; Quan, L. N.; Comin, R.; Walters, G.; Sabatini, R.; Voznyy, O.; Hoogland, S.; Zhao, Y.; Beauregard, E. M.; Kanjanaboos, P.; Lu, Z.; Kim, D. H.; Sargent, E. H. *Nat. Nanotechnol.* **2016**, *11* (10), 872–877.
9. Lee, J.-W.; Choi, Y. J.; Yang, J.-M.; Ham, S.; Jeon, S. K.; Lee, J. Y.; Song, Y.-H.; Ji, E. K.; Yoon, D.-H.; Seo, S.; Shin, H.; Han, G. S.; Jung, H. S.;

Kim, D.; Park, N.-G. *ACS Nano* **2017**, *11* (3), 3311–3319.

10. Xing, G.; Mathews, N.; Lim, S. S.; Yantara, N.; Liu, X.; Sabba, D.; Grätzel, M.; Mhaisalkar, S.; Sum, T. C. *Nat. Mater.* **2014**, *13* (5), 476–480.
11. Heiss, W.; Brabec, C. *Nat. Photonics* **2016**, *10* (5), 288–289.
12. Chin, X. Y.; Cortecchia, D.; Yin, J.; Bruno, A.; Soci, C. *Nat. Commun.* **2015**, *6*, ncomms8383.
13. Xu, W.; Cho, H.; Kim, Y.-H.; Kim, Y.-T.; Wolf, C.; Park, C.-G.; Lee, T.-W. *Adv. Mater.* **2016**, *28* (28), 5916–5922.
14. Choi, J.; Park, S.; Lee, J.; Hong, K.; Kim, D.-H.; Moon, C. W.; Park, G. D.; Suh, J.; Hwang, J.; Kim, S. Y.; Jung, H. S.; Park, N.-G.; Han, S.; Nam, K. T.; Jang, H. W. *Adv. Mater.* **2016**, *28* (31), 6562–6567.
15. Yan, K.; Peng, M.; Yu, X.; Cai, X.; Chen, S.; Hu, H.; Chen, B.; Gao, X.; Dong, B.; Zou, D. *J. Mater. Chem. C* **2016**, *4* (7), 1375–1381.
16. Hwang, B.; Gu, C.; Lee, D.; Lee, J.-S. *Sci. Rep.* **2017**, *7*, srep43794.
17. Liu, D.; Lin, Q.; Zang, Z.; Wang, M.; Wangyang, P.; Tang, X.; Zhou, M.; Hu, W. *ACS Appl. Mater. Interfaces* **2017**, *9* (7), 6171–6176.
18. Yoo, E.; Lyu, M.; Yun, J.-H.; Kang, C.; Choi, Y.; Wang, L. *J. Mater. Chem. C* **2016**, *4* (33), 7824–7830.
19. Lee, M.-J.; Lee, C. B.; Lee, D.; Lee, S. R.; Chang, M.; Hur, J. H.; Kim, Y.-B.; Kim, C.-J.; Seo, D. H.; Seo, S.; Chung, U.-I.; Yoo, I.-K.; Kim, K. *Nat. Mater.* **2011**, *10* (8), 625–630.
20. Lee, H. Y.; Chen, P. S.; Wu, T. Y.; Chen, Y. S.; Wang, C. C.; Tzeng, P. J.; Lin, C. H.; Chen, F.; Lien, C. H.; Tsai, M. J. In *2008 IEEE International*

Electron Devices Meeting; 2008; pp 1–4.

21. Kwon, D.-H.; Kim, K. M.; Jang, J. H.; Jeon, J. M.; Lee, M. H.; Kim, G. H.; Li, X.-S.; Park, G.-S.; Lee, B.; Han, S.; Kim, M.; Hwang, C. S. *Nat. Nanotechnol.* **2010**, *5* (2), 148–153.
22. Kim, K. M.; Jeong, D. S.; Hwang, C. S. *Nanotechnology* **2011**, *22* (25), 254002.
23. Cao, D. H.; Stoumpos, C. C.; Farha, O. K.; Hupp, J. T.; Kanatzidis, M. G. *J. Am. Chem. Soc.* **2015**, *137* (24), 7843–7850.
24. Zhuge, F.; Peng, S.; He, C.; Zhu, X.; Chen, X.; Liu, Y.; Li, R.-W. *Nanotechnology* **2011**, *22* (27), 275204.
25. Gao, S.; Chen, C.; Zhai, Z.; Liu, H. Y.; Lin, Y. S.; Li, S. Z.; Lu, S. H.; Wang, G. Y.; Song, C.; Zeng, F.; Pan, F. *Appl. Phys. Lett.* **2014**, *105* (6), 063504.
26. Yang, C.-S.; Shang, D.-S.; Chai, Y.-S.; Yan, L.-Q.; Shen, B.-G.; Sun, Y. *Phys. Chem. Chem. Phys.* **2016**, *18* (18), 12466–12475.
27. Wang, Z. Q.; Xu, H. Y.; Zhang, L.; Li, X. H.; Ma, J. G.; Zhang, X. T.; Liu, Y. C. *Nanoscale* **2013**, *5* (10), 4490–4494.
28. Szot, K.; Speier, W.; Bihlmayer, G.; Waser, R. *Nat. Mater.* **2006**, *5* (4), 312–320.
29. Kim, K. M.; Choi, B. J.; Shin, Y. C.; Choi, S.; Hwang, C. S. *Appl. Phys. Lett.* **2007**, *91* (1), 012907.
30. Jung, K.; Seo, H.; Kim, Y.; Im, H.; Hong, J.; Park, J.-W.; Lee, J.-K. *Appl. Phys. Lett.* **2007**, *90* (5), 052104.
31. Cao, B.; Cai, W.; Zeng, H. *Appl. Phys. Lett.* **2006**, *88* (16), 161101.

32. Hsiung, C.-P.; Liao, H.-W.; Gan, J.-Y.; Wu, T.-B.; Hwang, J.-C.; Chen, F.; Tsai, M.-J. *ACS Nano* **2010**, *4* (9), 5414–5420.

33. Yang, Y.; Gao, P.; Gaba, S.; Chang, T.; Pan, X.; Lu, W. *Nat. Commun.* **2012**, *3*, 1737.

34. Celano, U.; Goux, L.; Belmonte, A.; Opsomer, K.; Franquet, A.; Schulze, A.; Detavernier, C.; Richard, O.; Bender, H.; Jurczak, M.; Vandervorst, W. *Nano Lett.* **2014**, *14* (5), 2401–2406.

35. Strachan, J. P.; Pickett, M. D.; Yang, J. J.; Aloni, S.; David Kilcoyne, A. L.; Medeiros-Ribeiro, G.; Stanley Williams, R. *Adv. Mater.* **2010**, *22* (32), 3573–3577.

36. Wiesmann, H. J.; Zeller, H. R. *J. Appl. Phys.* **1986**, *60* (5), 1770–1773.

37. Chae, S. C.; Lee, J. S.; Kim, S.; Lee, S. B.; Chang, S. H.; Liu, C.; Kahng, B.; Shin, H.; Kim, D.-W.; Jung, C. U.; Seo, S.; Lee, M.-J.; Noh, T. W. *Adv. Mater.* **2008**, *20* (6), 1154–1159.

38. Holland, T. J. B.; Redfern, S. a. T. *Mineral. Mag.* **1997**, *61* (1), 65–77.

39. Mitzi, D. B. *Chem. Mater.* **1996**, *8* (3), 791–800.

Chapter 5

A Fundamental Approach for extended RS performance

Quote

Leon O. Chua

"The three basic two-terminal circuit elecments are defined in terms of a relationship between two of the four fundamental circuit variables." (1971)

5.1. Introduction

In recent years, several intensive research have been in progress for the application of halide perovskites (HPs) in microelectronic devices beyond solar cells,[1–3] such as light-emitting diodes,[4, 5] photodetectors,[6, 7] resistive switching devices,[8–10] thin-film transistors,[11–13] and artificial synapses.[14, 15] This is particularly true because HP-based resistive switching memories exhibit low-operation voltages, reduced power consumption, high on/off ratios, and remarkable mechanical flexibility.[9, 16] These outstanding properties are suitable for next-generation resistive switching memories. However, the present HP-based resistive switching memories have critical weaknesses, such as short endurance and poor air-stability. To overcome these limitations, diverse solutions have been reported. One strategy is discovering and synthesizing more stable chemical compositions of HPs. To obtain stable resistive switching properties, various compositions of HPs have been investigated and reported.[17–19] Another strategy is adopting a passivation layer on HP films, such as polymethyl methacrylate (PMMA), zinc oxide, and ethylene diamine, so as to isolate the films from the atmosphere and complement their defects.[20–23] The other strategy is by improving the morphology of the HP films. In this regard, solvent engineering can be employed. By dripping antisolvents, such as toluene, benzene, and chlorobenzene, and adding hydroiodic acid solution as an additive in the precursor solution of HPs, morphologically uniform and high quality HP films[24–27] can be obtained. Nevertheless, these strategies still could not provide the fundamental solutions to the degradation mechanism in resistive switching devices.

I have been interested in the use of HPs for resistive switching devices because HP easily changes its composition and crystalline structure by a certain tolerance factor (*t*) value.[28, 29] The $MAPbI_3$ crystalline structure is a pseudo-cubic structure under ambient conditions. However, the MA^+ cation of $MAPbI_3$ in BX_6 octahedral void causes a disordered structure and exhibits hysteresis, which is an important factor in the resistive switching behavior.[30, 31] Hence, $MAPbI_3$ is weak under ambient conditions because of the volatile MA^+ cation. On the other hand, the $RbPbI_3$ crystalline structure is orthorhombic, which is extremely stable under ambient conditions because of the less volatile Rb^+ cation and can be stabilized as a one-dimensional orthorhombic configuration in nature.[32–35] A stable mixture of HPs was made by mixing stable $RbPbI_3$. The controlled Ag migration in $Rb_{1-x}MA_xPbI_3$ could be beneficial for the resistive switching behavior because of the control formation and rupture of the conducting bridge by the non-switchable $RbPbI_3$.

Here, I report the mixture of non-switchable $RbPbI_3$ and switchable $MAPbI_3$ as resistive switching memory to control the growth of the Ag bridge, which connects between the top and bottom electrodes. With the ultralow operation electric field and on/off ratio, all solutions processed $Rb_{1-x}MA_xPbI_3$ resistive switching memory shows three times extended endurance than pristine $MAPbI_3$ memories. To provide direct evidence for the resistive switching behavior, conductive atomic force microscopy (CAFM) and energy-dispersive X-ray spectroscopy (EDS) mapping were highlighted with a field scanning electron microscope (FE-SEM) to observe the role of the Ag bridge through the HP films as an insulator. To enhance air stability, a solution-processed ultrathin PMMA

layer coated on a perovskite layer protects the device from water vapor and oxygen in atmosphere. Our study provides a new strategy to enhance the endurance of HP-based resistive switching memories for next generation non-volatile computer storage.

5.2. Experimental Procedures

Materials preparation: All materials were used without purification. PbI_2 (99.9985%) was purchased from Alfa Aesar (U.S.A.) and CH_3NH_3I from Xi'AnP-OLED Co. (China). Expect of two materials and RbI (99.9%) were purchased from Sigma-Aldrich (U.S.A).

Film formation and MIM cell fabrication: The Pt (100 nm)/Ti (20 nm)-deposited substrates were prepared by an electron beam evaporator. The Pt/Ti-coated Si wafer substrates were cleaned by an ultrasonic-bath in acetone, ethanol, and deionized water, each for 15 min. The prepared mixture perovskite solution is 55 wt.% CH_3NH_3I, RbI, PbI_2 and DMSO (Sigma-Aldrich, >99.9%), at 1-x:x:1:1 molar ratio, in *N*,*N*-dimethylformamide (Sigma-Aldrich, 99.8%). The perovskite precursor solution was coated on the Pt/Ti-coated Si wafer substrate by the adduct method reported by Park et al. The 8.5 μL of dissolved solution was spin-coated on the substrates at 4000 rpm for 20 s and after starting spin-coating, 0.5 mL of diethyl ether drops (Sigma Aldrich) were provided for 10 s. The spin-coated mixture perovskite films were annealed at 70 °C for 1 min and thereafter at 100 °C for 5 min. Then, as it cooled to room temperature, 20 μL of PMMA solution was deposited by spin-coating at 4000 rpm for 30 s. The solution consisted of 2 mg PMMA (Sigma Aldrich) in 1 mL of chlorobenzene (Sigma Aldrich, 99.8%). The device was fabricated using a thermal evaporator of 100-nm thick Ag through the shadow mask at a pressure of 3×10^{-6} Torr.

Device characterization: The surface and cross-sectional images were obtained by FE-SEM (JSM-7600F, JEOL). The crystalline structures were

detected by X-ray diffractometer (D8 advance, Bruker) with Cu Kα radiation (λ = 1.54056 Å). The XRD data was recorded in the range of 5–60° of the 2 theta range with a scan speed of 6° min^{-1}. Samples of TEM were prepared by FIB (JIB-4601F, JEOL). Then, the distribution of elements on the mixture perovskite films was detected by TEM/EDS (JEM ARM 200F, JEOL). The *I-V* characteristics of the device (DC voltage sweeping mode) and resistive switching by alternating voltage pulse were achieved using an Agilent 4156C semiconductor analyzer under a vacuum of 6×10^{-2} Torr. To observe the topography and resistance change of the $Rb_{1-x}MA_xPbI_3$ films, the films deposited on a Ag/Ti/SiO_2/Si substrate were measured using an AFM (Park systems XE100).

5.3. Results and Discussion

Figure 65a-c shows the schematic of the top, three-dimensional (3D), and front views of the $MAPbI_3$ crystalline structure. The $MAPbI_3$ crystal structure is a pseudo-cubic phase because of the change in the crystalline structure effected by the MA^+ cation random motion.[36] Hence, the top and front schematics do not show a crystalline structure that is rotated and tilted. As shown in Figure 65d-f, the $RbPbI_3$ crystalline structure is in the orthorhombic phase because of being broken as a cubic structure by the lattice distortion of the small Rb^+ cation. The top, 3D, and front schematics exhibit a crystalline structure, which is rotated and tilted. The space group configuration of $RbPbI_3$ has a very stable orthorhombic structure.[32, 33]

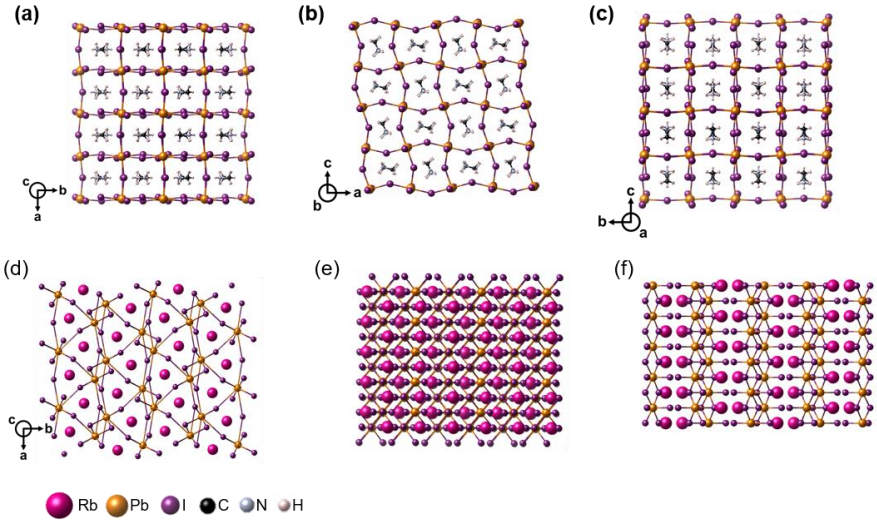

Figure 65 Crystal structure of $MAPbI_3$ (a-c, MA=CH_3NH_3) and $RbPbI_3$ (d-f). (a, d) top view, (b, e) 3-dimension view and (c, f) cross-sectional view.

Figure 66 shows the X-ray diffraction (XRD) patterns of $MAPbI_3$, $RbPbI_3$, and different RbI concentration because of the formation of $Rb_{1-x}MA_xPbI_3$. A single-phase halide perovskite was confirmed from pristine $MAPbI_3$ (orange line) and $RbPbI_3$ (magenta line).[37, 38] As the concentration of RbI increases, $Rb_{1-x}MA_xPbI_3$ is formed because both $MAPbI_3$ and $RbPbI_3$ XRD patterns were observed. As the concentration of $RbPbI_3$ increases, the intensity of $RbPbI_3$ XRD pattern increases, whereas the intensity of $MAPbI_3$ XRD pattern decreases. This is because the $MAPbI_3$ crystalline structure is broken and the $RbPbI_3$ is formed by the lattice distortion of the three-dimensional network of BX_6 distortion as a result of the Rb^+ ion being smaller than the MA^+ ion.

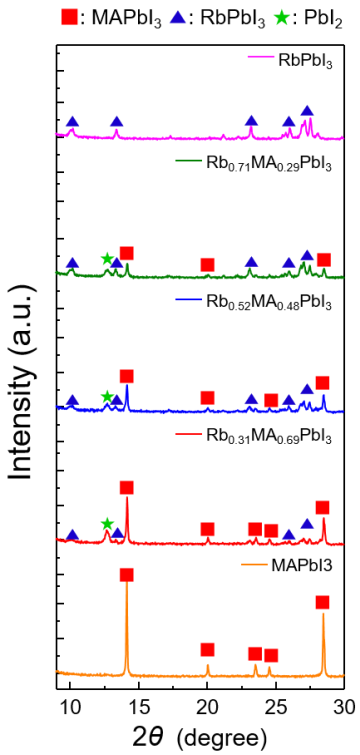

Figure 66 X-ray diffraction pattern of the $Rb_{(1-x)}MA_xPbI_3$/Pt substrates. (Orange line - $MAPbI_3$, Red line – $Rb_{0.31}MA_{0.69}PbI_3$, Blue line - $Rb_{0.52}MA_{0.48}PbI_3$, Green line - $Rb_{0.71}MA_{0.29}PbI_3$ and Magenta line - $RbPbI_3$)

To investigate the entire distribution of $RbPbI_3$ and $MAPbI_3$ crystalline structure, we conducted an energy-dispersive X-ray spectroscopy mapping of the rubidium and lead atoms using a scanning-transmission electron microscope (STEM) on a vertical PMMA/$Rb_{1-x}MA_xPbI_3$/Pt/Ti/SiO_2/Si sample, made by focused ion beam (FIB) milling. The aforementioned is conducted because only rubidium atoms are detected from $RbPbI_3$, whereas lead atoms are detected from both $RbPbI_3$ and $MAPbI_3$. The EDS mapping shows the distribution of $RbPbI_3$ in $MAPbI_3$ by the distribution of rubidium atoms, which are related to lead atoms. Figure 67a–e shows the cross-sectional view of STEM

images of PMMA/$Rb_{1-x}MA_xPbI_3$/Pt/Ti/SiO_2/Si devices and their EDS mapping for rubidium and lead atoms. In the STEM dark field image of pristine $MAPbI_3$, grain boundaries were observed. The distribution of rubidium and lead atoms is counted in $MAPbI_3$. However, the pristine $MAPbI_3$ does not involve rubidium atoms. Accordingly, rubidium atoms in the $MAPbI_3$ are counted by means of characteristic X-ray that is called hard X-ray. The hard X-ray generates from aperture, holder, lens, vacuum chamber and specimen. Backscattering of X-ray phonons occurs first from specimen then from bulk. These scattering X-ray phonons can generates continuous and characteristic X-ray.[39] Therefore, small amounts of rubidium atoms, confirmed to exist only in $MAPbI_3$, were ignored by hard X-ray (Figure 67a). For pure $RbPbI_3$ STEM dark field image, the grain boundary was not detected. On the other hand, rubidium and lead atoms were detected throughout the thin films. Where the amount of rubidium atoms is close to the amount of lead atoms, it was confirmed to synthesize the pristine $RbPbI_3$ (Figure 67e). To increase $RbPbI_3$ concentration, grain boundaries were reduced with the mixture of $MAPbI_3$ and $RbPbI_3$. As the concentration of RbI increases, the rubidium atoms become uniform in distribution and their concentration increases. Hence, a uniform distribution and an increased concentration of $RbPbI_3$ can be observed. This suggests that the concentration of $RbPbI_3$ is inversely proportional to the grain boundaries in the $Rb_{1-x}MA_xPbI_3$ film.

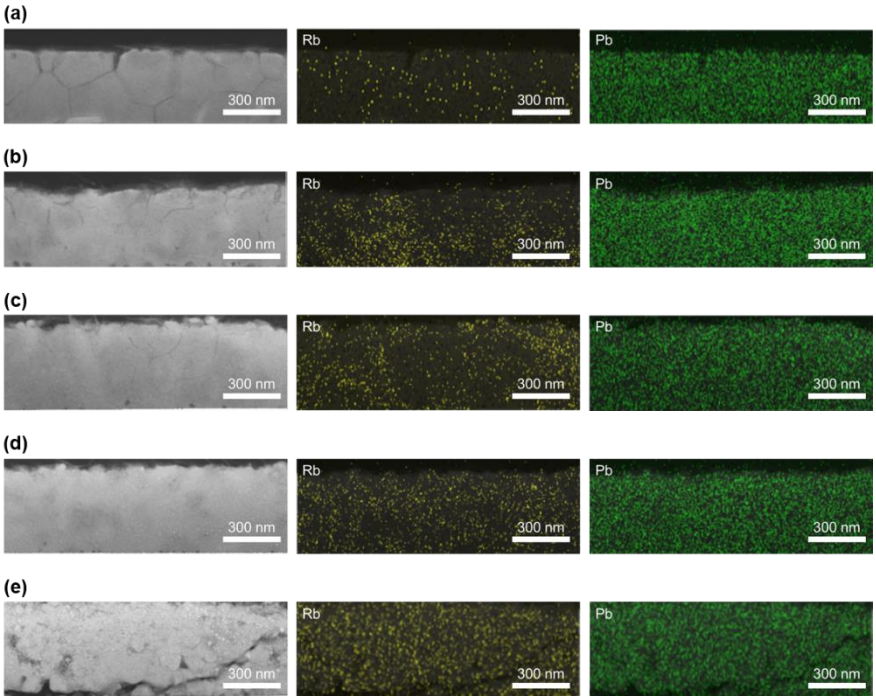

Figure 67 Cross-sectional view scanning transmission electron microscopy (STEM) image and energy dispersive spectrometer (EDS) mapping of (a) $MAPbI_3$ (b) $Rb_{0.31}MA_{0.69}PbI_3$, (c) $Rb_{0.52}MA_{0.48}PbI_3$, (d) $Rb_{0.71}MA_{0.29}PbI_3$ and (e) $RbPbI_3$ films (White - scanning transmission electron microscopy dark field image, Yellow - Rb atom and Green- Pb atom by corresponding STEM-EDS)

Figure 68 shows the schematic and optical microscopic image of the vertical Ag/$Rb_{1-x}MA_xPbI_3$/Pt/Si structured device. The Pt/Ti substrate was treated with UV ozone to improve its wettability before the spin-coating process. Uniform films were formed by using the Lewis acid–base adduct method.[40] The process is as follows. First, the precursor solution of MAI, RbI, PbI_2 and dimethyl sulfoxide (DMSO) was dropped in *N*,*N*-dimethylformamide solution. Thereafter, the solution was spread over the entire the substrate. Then, ether is dropped on the center of the substrate during spin coating. Finally, the substrate

is annealed to remove the solvent. To fabricate the vertical MIM structure device, the Ag top electrodes are deposited using a thermal evaporator and a 100 × 100 μm^2 dot patterned shadow mask.

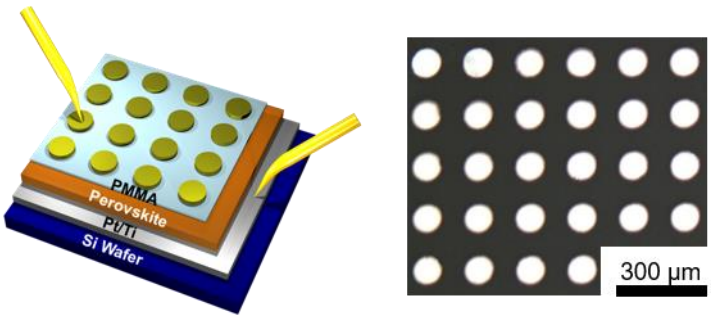

Figure 68 Schematic (left) and optical microscopic image (right) of Ag/PMMA/$Rb_{1-x}MA_xPbI_3$/Pt devices.

From typical cross-sectional SEM images, pristine polycrystalline $MAPbI_3$ and $Rb_{1-x}MA_xPbI_3$ layers were observed to be deposited on the Pt/Ti deposited Si substrates. The 500-nm thick pristine $MAPbI_3$ and $Rb_{1-x}MA_xPbI_3$ films were uniformly deposited and pin-hole free with antisolvent dripping (Figure 69). For a comparison of resistive switching properties in pristine $MAPbI_3$ and $Rb_{1-x}MA_xPbI_3$, the thickness of all HP films were fixed for the application equivalent electric fields.

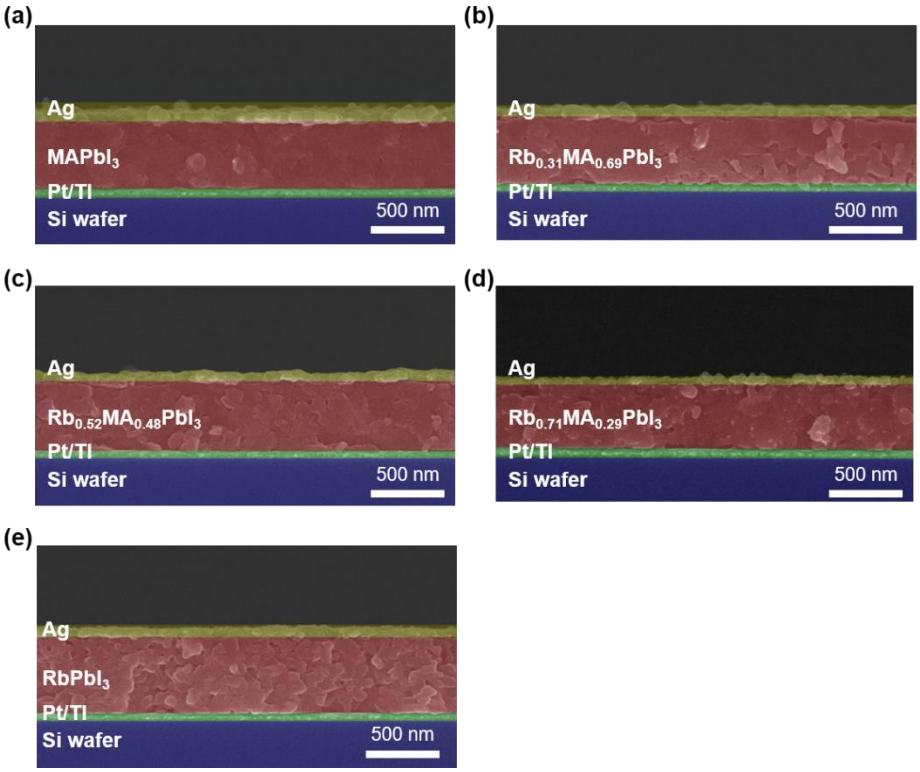

Figure 69 Cross-sectional view SEM image of the Ag/PMMA/$Rb_{1-x}MA_xPbI_3$/Pt devices. (a) $MAPbI_3$ (b) $Rb_{0.31}MA_{0.69}PbI_3$, (c) $Rb_{0.52}MA_{0.48}PbI_3$, (d) $Rb_{0.71}MA_{0.29}PbI_3$ and (e) $RbPbI_3$.

As shown in the plane-view SEM images, the average grain sizes of the HP films, which are pristine $MAPbI_3$ and $RbPbI_3$ concentrations of 30, 50, and 70%, are 150, 126, 85, and 70 nm, respectively (Figure 70). The average grain size of HP films tends to be reduced as the concentration of $RbPbI_3$ is increased.

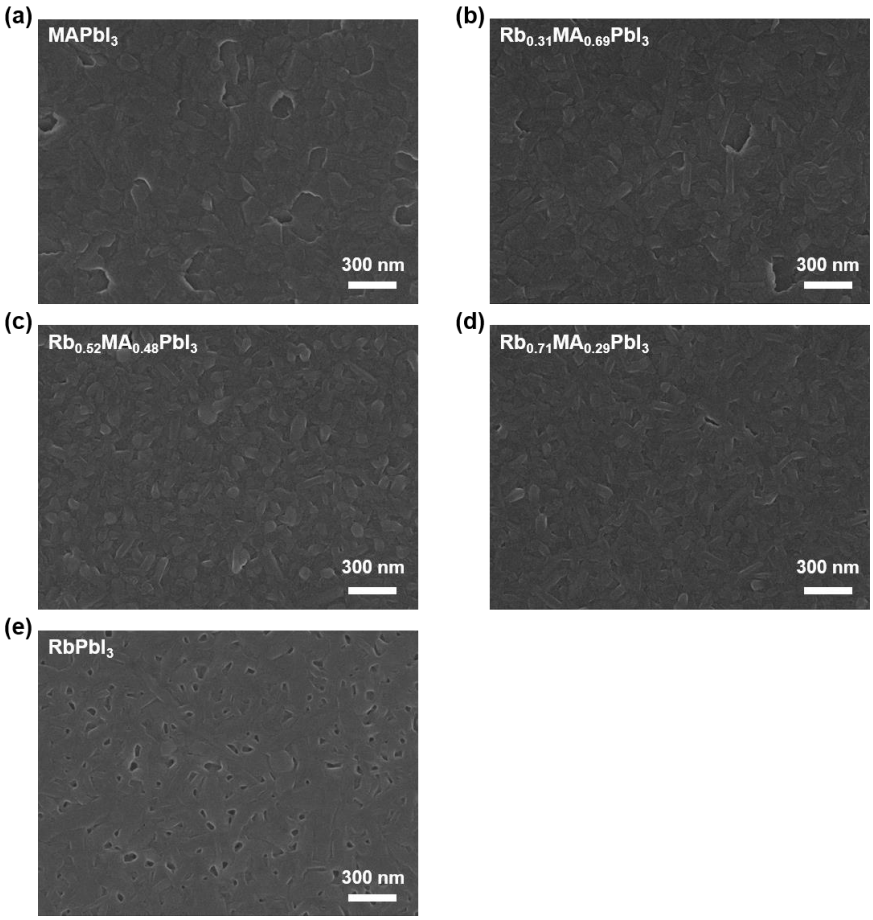

Figure 70 Plane-view SEM image of (a) $MAPbI_3$ (b) $Rb_{0.31}MA_{0.69}PbI_3$, (c) $Rb_{0.52}MA_{0.48}PbI_3$, (d) $Rb_{0.71}MA_{0.29}PbI_3$ and (e) $RbPbI_3$ films.

Typical *I-V* characteristics of fabricated devices are shown in Figure 71a–d. The *I-V* characteristics were measured under the DC sweeping mode of the semiconductor parameter analyzer. The external biases were applied to the Ag top electrodes, whereas the Pt bottom electrodes were grounded. The measurement of *I-V* characteristics was performed to the applied voltage bias sweep with a voltage step of 0.01 V (0 → maximum positive voltage → 0 → maximum negative voltage → 0). For the pristine $MAPbI_3$ device, the applied

maximum positive and negative voltages were +0.3 and −0.3 V. Similarly, the applied maximum positive and negative voltages for $RbPbI_3$ with concentrations of 31, 52, 71, and 100% (pristine $RbPbI_3$) mixed devices were ±1, ±1, ±1.5, and ±2 V, respectively. In the initial DC sweeping, $Rb_{1-x}MA_xPbI_3$ devices showed an electroforming process. Present studies have reported that HP-based resistive switching devices are electroforming-free regardless of the switching mechanism.[8–10] However, our $Rb_{1-x}MA_xPbI_3$-based resistive switching devices exhibited electroforming process, which is analogous to general resistive switching devices.[41, 42] The voltage for the electroforming process is also proportional to the concentration of $RbPbI_3$. The electroforming voltage for $RbPbI_3$ with concentrations of 30, 50, and 70% was +0.6, +1.2, and +1.35 V, respectively. After the electroforming process, all devices, except the pristine $RbPbI_3$-based device, showed general resistive switching behaviors. Initially, the devices maintained high resistance states (HRS, ~10^{-9} A). Thereafter, the current levels sharply increased and became low resistance states (LRS, ~10^{-3} A), where the applied bias is approximately +0.25 V. After applying a negative bias of approximately −0.12 V, the devices abruptly turned to an HRS. All of the devices exhibited general bipolar switching without the pristine $RbPbI_3$ device. These *I-V* characteristics suggest that the conducting paths through HP films are localized by the conducting bridge. However, the pristine $RbPbI_3$ device did not show resistive switching behavior even though high voltage (~2 V) was applied. After the electroforming process, the $Rb_{1-x}MA_xPbI_3$ resistive switching devices exhibited a SET voltage of approximately +0.25 V, except for the pristine $RbPbI_3$ device.

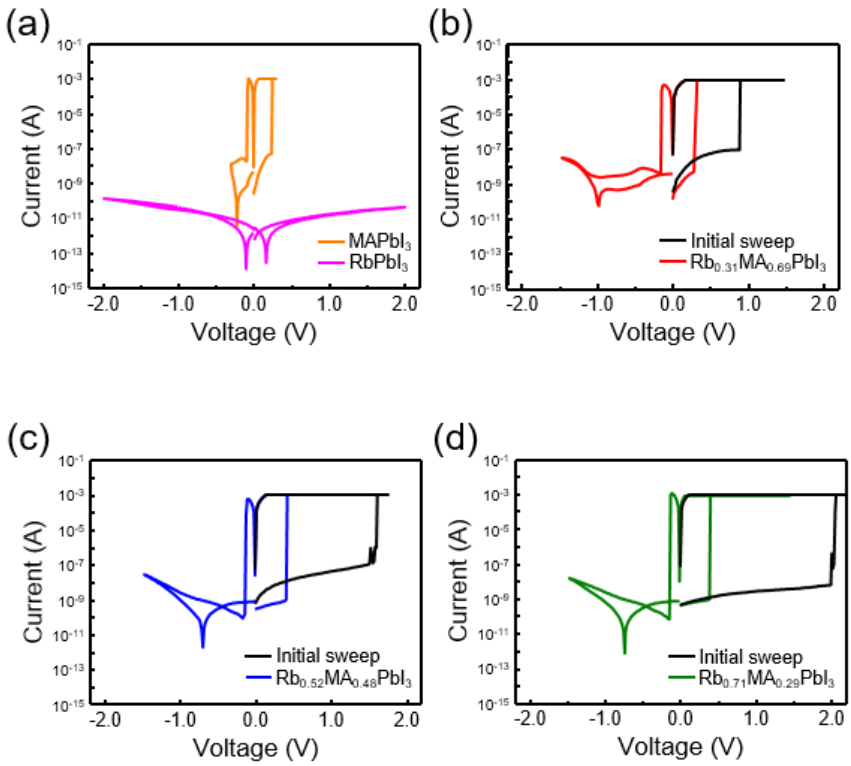

Figure 71 Typical current−voltage (*I*−*V*) characteristics of Ag/PMMA/$RbPbI_3$ mixed $MAPbI_3$/Pt devices. (a) $MAPbI_3$ and $RbPbI_3$, (b) $Rb_{0.31}MA_{0.69}PbI_3$, (c) $Rb_{0.52}MA_{0.48}PbI_3$, and (d) $Rb_{0.71}MA_{0.29}PbI_3$.

As described in Figure 72a–d, the endurance of the resistive switching with voltage pulses (alternating current biases) was measured without the pristine $RbPbI_3$-based device. The switching voltage for the SET process is slightly different. The pristine $MAPbI_3$ and 30% of the $RbPbI_3$ mixed with $MAPbI_3$ devices were operable with a SET voltage of +0.3 V (SET) and −1 V (RESET). On the other hand, 50 and 70% of the $RbPbI_3$ mixed devices were switchable with a higher SET voltage of +0.5 V. The RESET voltage was equivalent for all devices. Because of the limitation of the semiconductor parameter analyzer, the switching speed was fixed to 640 μs. The endurance of the pristine $MAPbI_3$

device was 300 cycles (Figure 72a). However, $Rb_{1-x}MA_xPbI_3$ devices exhibited extended endurance. This tendency becomes more pronounced as the concentration of $RbPbI_3$ is increased. The devices with $RbPbI_3$ concentrations of 31, 52, and 71% showed endurance of 670, 820, and 970 cycles, respectively (Figure 72b–d). This result suggests that the non-switchable $RbPbI_3$ contributes to the stable formation and rupture of a conducting bridge between the top and bottom electrodes.

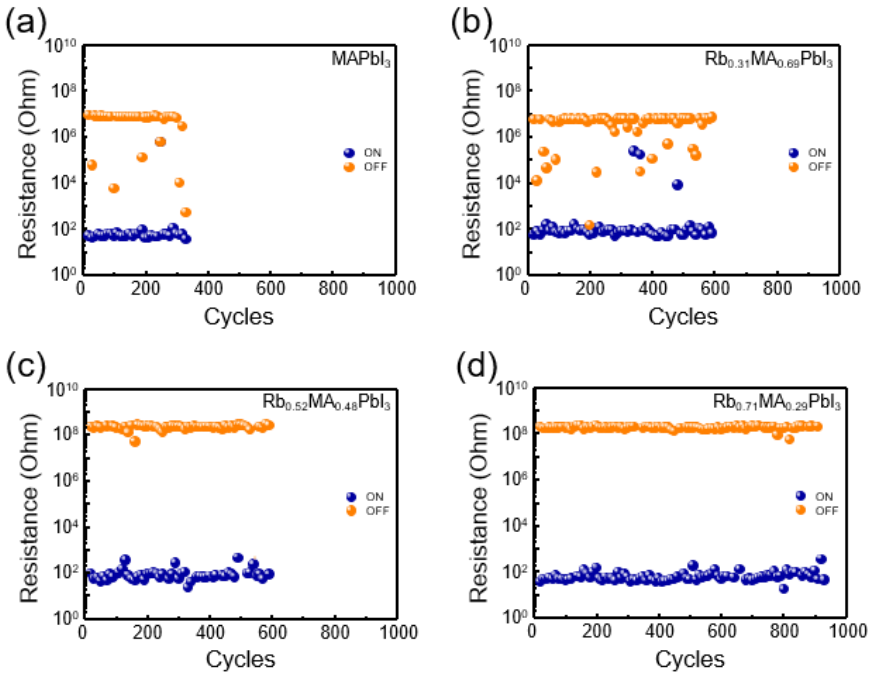

Figure 72 Reversible resistive switching behavior measured with the voltage pulses. Pulse width is fixed to 640 μs. (a) $MAPbI_3$, (b) $Rb_{0.31}MA_{0.69}PbI_3$, (c) $Rb_{0.52}MA_{0.48}PbI_3$, and (d) $Rb_{0.71}MA_{0.29}PbI_3$.

The retention characteristics of both pristine $MAPbI_3$ and $Rb_{1-x}MA_xPbI_3$ devices were up to 12 000 s in HRS (Figure S3). In LRS, the retention characteristics of the pristine $MAPbI_3$ devices were up to 5200 s, and Rb_{1-}

$_xMA_xPbI_3$ devices exhibited from 8000–10000 s, irrespective of the concentration of $RbPbI_3$.

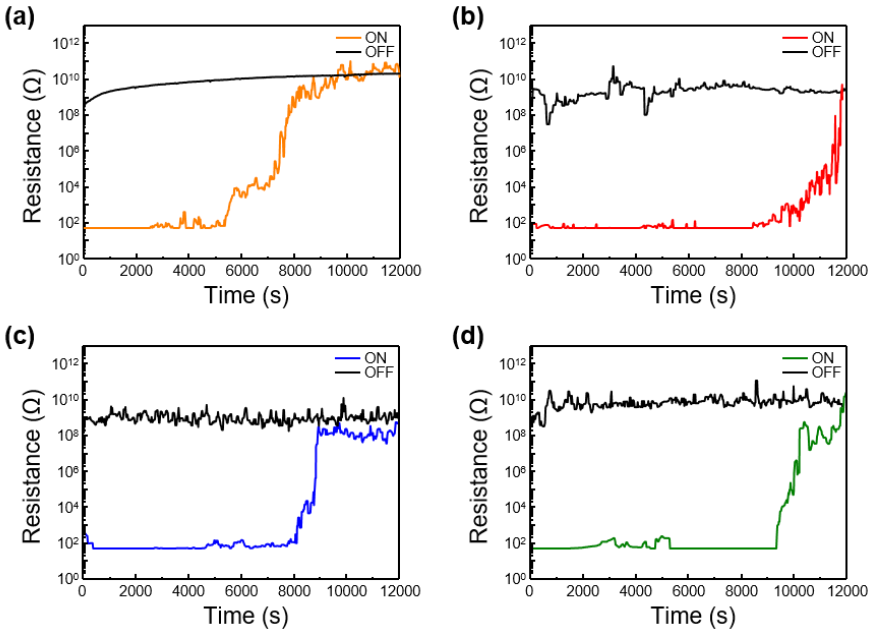

Figure 73 Retention characteristics of the Ag/PMMA/$Rb_{1-x}MA_xPbI_3$/Pt devices. (a) $MAPbI_3$ (b) $Rb_{0.31}MA_{0.69}PbI_3$, (c) $Rb_{0.52}MA_{0.48}PbI_3$, and (d) $Rb_{0.71}MA_{0.29}PbI_3$

In order to check the long-term stability, we measured *I-V* characteristics of Ag/PMMA/$Rb_{1-x}MA_xPbI_3$/Pt devices. The devices were stored in ambient condition *I-V* characteristics of the devices were conducted every day. Since PMMA layer (~30 nm) for passivation protected $Rb_{1-x}MA_xPbI_3$ films from H_2O and O_2 in ambient condition, the devices exhibited general bipolar resistive switching behavior for 8 days (Figure 74).

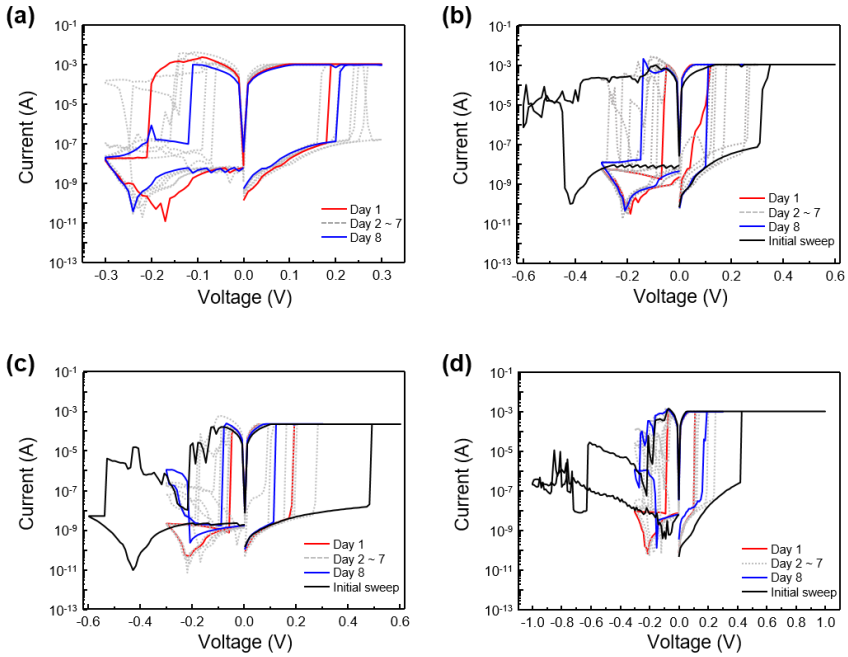

Figure 74 Long-term stability of the Ag/PMMA/$Rb_{1-x}MA_xPbI_3$/Pt devices. (a) $MAPbI_3$ (b) $Rb_{0.31}MA_{0.69}PbI_3$, (c) $Rb_{0.52}MA_{0.48}PbI_3$, and (d) $Rb_{0.71}MA_{0.29}PbI_3$.

To provide a plausible explanation for conduction mechanism in the $Rb_{1-x}MA_xPbI_3$ devices, the *I-V* characteristics of the devices were measured at various temperatures. From the linear-plot of the *I-V* curves, the *I-V* characteristics in the LRS only exhibited a linear region (Figure 75). It suggested that the conduction mechanism of the $Rb_{1-x}MA_xPbI_3$ device is an ohmic conduction. Because the current flow is governed by the conducting bridge, the resistance of typical metallic filament-based resistive switching devices in LRS follows the temperature dependence of metals, which means that the resistance of the metallic filament is proportional to temperature.[43, 44] For example, the resistance of approximately 20 Ω increases when the temperature increases by 100°. However, our device does not exhibit temperature dependence of the resistance in LRS because the fluctuation range

of the resistance in LRS is greater than the increase in resistance when temperature increases.[16]

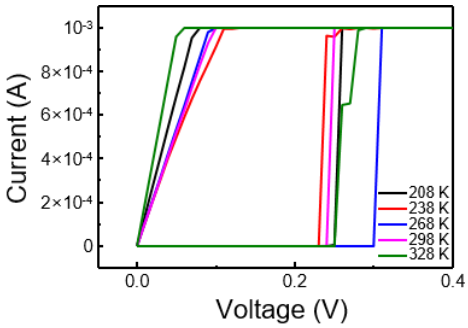

Figure 75 Linear *I*−*V* characteristics of the Ag/PMMA/$Rb_{1-x}MA_xPbI_3$/Pt devices in low resistance state.

In HRS, the *I*-*V* characteristics of the $Rb_{1-x}MA_xPbI_3$ device showed both linear and non-linear regions (Figure 76a). Generally, previous studies of halide perovskite-based resistive switching devices described that the conduction is governed by the space charge limited conduction (SCLC) in HRS.[8, 9] However, SCLC is not appropriate for our device because the slope of the non-linear region in *I*-*V* curves is proportional to the temperature in HRS (Figure 76a and b). To interpret the conduction behavior in HRS, we fitted the *I*-*V* characteristics and computed the average ion hopping distances (Figure 76b).[41, 45] The thermally-assisted ion hopping is governed by the equation,

$$J = \sigma_{TAH}E = n_c 2\nu_{TAH} a q_e \exp\left(\frac{\Delta H}{kT}\right) sinh\left(\frac{q_e E a}{2kT}\right)$$

where n_c is the concentration of the majority carrier, q_e is the elementary charge, υ is the frequency factor, and a is the ion hopping distance. We aimed at determining the relationship between the ion hopping distance, a, and temperature, *T*. With the fitted *I*-*V* characteristics, the simplified equation,

$$J = N sinh\left(\frac{q_e E a}{2kT}\right), N = n_c 2\nu_{TAH} a q_e \exp\left(\frac{\Delta H}{kT}\right)$$

resulted to the ion hopping distances of 78.31, 93.25, 109.26, 129.45, and 164.43 nm at 208, 238, 268, 298, and 328 K, respectively. The above equation and *I-V* characteristics indicate that the ion hopping distance is proportional to temperature. Therefore, this suggests that the conduction mechanism of the $RbPbI_3$ mixed $MAPbI_3$ devices is an ohmic conduction in LRS and a thermally assisted ion hopping mechanism in HRS.

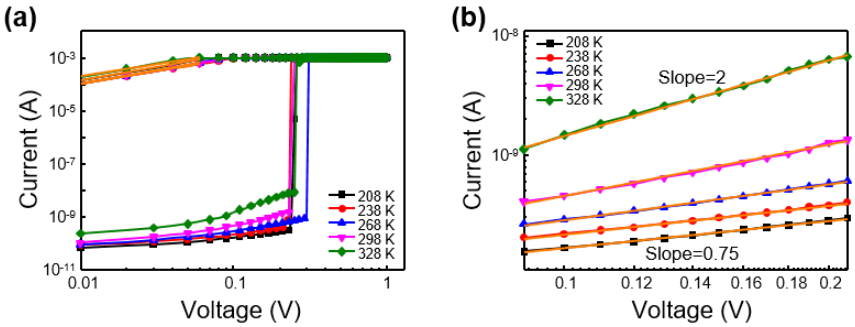

Figure 76 Logarithmic *I*−*V* characteristics of the Ag/PMMA/$Rb_{1-x}MA_xPbI_3$/Pt devices in (a) low resistance state and (b) high resistance state.

To investigate the source of the resistive switching behavior in HP films, we conducted a CAFM measurement of the vertical PMMA/$Rb_{1-x}MA_xPbI_3$/PMMA/Ag/Ti/SiO_2/Si structured device. The concentration of $RbPbI_3$ was 50%. To observe the migration of Ag ions, we used an Ag coated Si substrate. Because of the electrochemically active Ag bottom electrodes, ultrathin PMMA layers (~30 nm) were deposited between the Ag bottom electrodes and HP films to prevent a reaction, resulting in the formation of AgI layer (Figure 77).[46, 47]

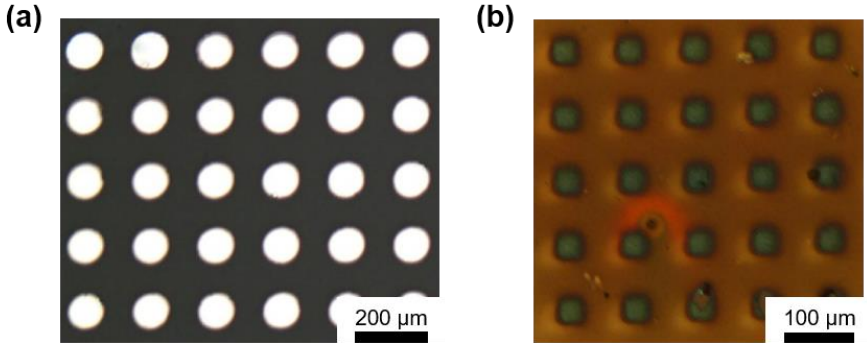

Figure 77 The effect of the PMMA layer to prevent chemical reation between Ag top eletrodes and halide perovskite films. (a) PMMA coated, and (b) non-coated $MAPbI_3$ films.

Figure 78 shows topological atomic force microscopy images of 10 × 10 μm^2 HP films. The root mean square roughness is 11.475 nm and the average grain size is approximately 83 nm.

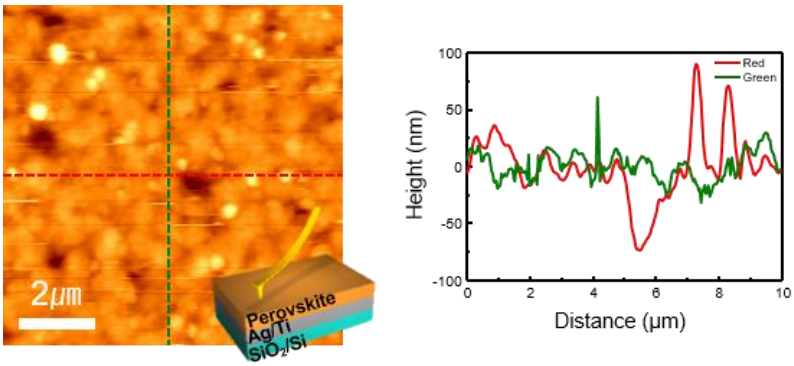

Figure 78 Topological atomic force microscopy (AFM) images of the $RbPbI_3$ mixed $MAPbI_3$ films of 10 × 10 μm^2 (left). The roughness is measured by AFM tips moving along the green and red dotted lines by distance (right).

First, a bias of 0.4 V was applied to the HP films of area 10 × 10 μm^2. At a bias of 0.4 V on the Pt coated tip, the $Rb_{1-x}MA_xPbI_3$ film was fully insulating at

current levels of 6–8 × 10^{-9} A (Figure 79a). Then, we applied a bias of 0.8 V to an area of 5 × 5 μm^2, which is at the center of the area measured in Figure 79b. The $Rb_{1-x}MA_xPbI_3$ film became fully conducting after a bias of 0.8 V was applied.

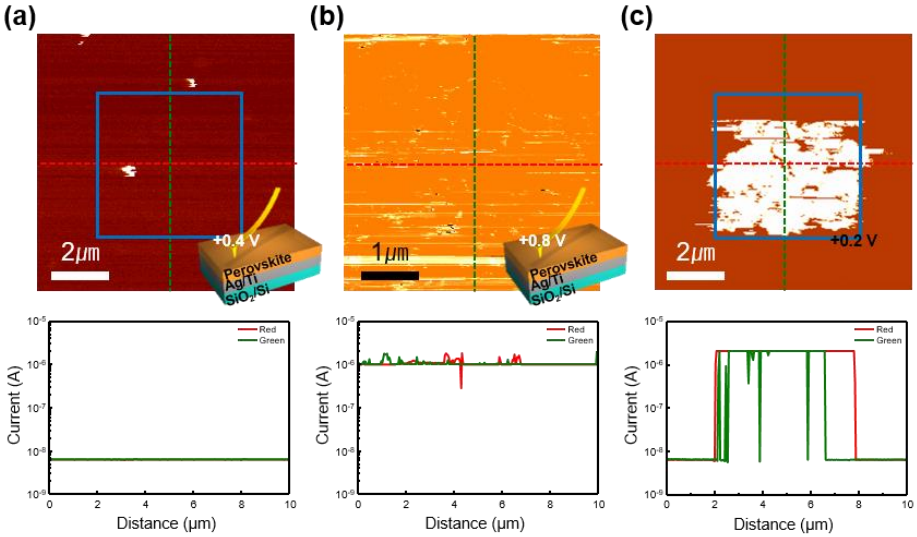

Figure 79 Conductive AFM image of the of the $Rb_{1-x}MA_xPbI_3$ films of (a) 10 × 10 μm^2 at bias 0.4 V, (b) 5 × 5 μm^2 (blue are in (a) and (c)) at bias 0.8 V and 10 × 10 μm^2 at bias 0.2 V. The current is measured by AFM tips moving along the green and red dotted lines by distance (bottom).

The current level of the $Rb_{1-x}MA_xPbI_3$ film was approximately 10^{-6} A. Thereafter, a CAFM measurement was conducted for the whole area of 10 × 10 μm^2 with a bias of 0.2 V. The mapping image describes that the region with a bias of 0.8 V retains the conducting state (Figure 79c). Moreover, the line profiles (red and green lines) in Figure 5d exhibit the part of the $Rb_{1-x}MA_xPbI_3$ film, which was applied with a bias of 0.8 V became a conducting state.

To clarify the atomic element of the conducting filament, we performed an EDS mapping of the $Rb_{1-x}MA_xPbI_3$ film where we conducted CAFM measurement. The blue boxes indicate the region where CAFM measurement was conducted. Because the CAFM measurement was performed under the contact mode, morphological changes of HP films were observed in a plane-view SEM image (Figure 80).

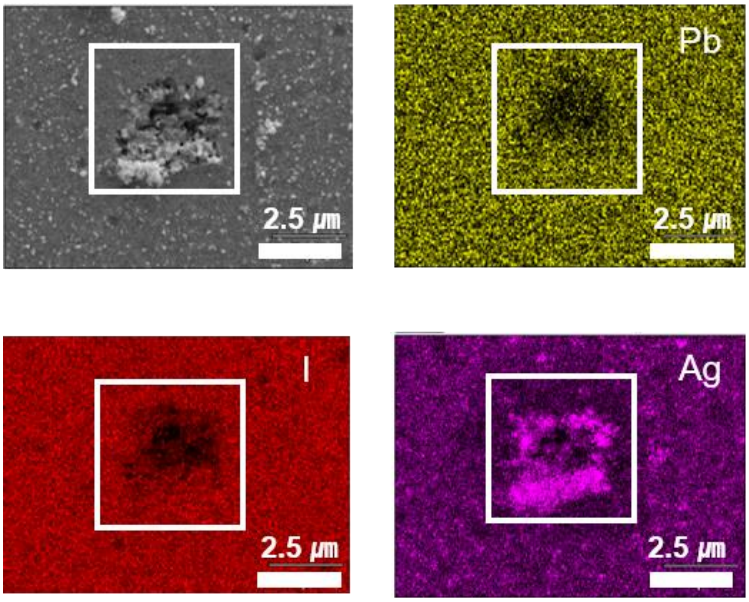

Figure 80 Plane view SEM image and EDS mapping of the $Rb_{0.52}MA_{0.48}PbI_3$ films after CAFM measurement. (SEM image – dark field, yellow – Pb atom, red – I atom, purple – Ag atom and white area is CAFM measurement.

Without the region where CAFM was performed, the EDS mapping of Ag, Pb, and I indicates that they are homogeneously distributed within the HP films, suggesting that the films are uniformly fabricated on the Ag deposited substrate. The region where the CAFM measurement was conducted showed relatively high concentrations of Ag atoms based on the EDS mapping images. However,

the EDS mapping of I and Pb exhibited a slightly low intensity in the region where the CAFM was performed because the HP film was damaged by the Pt coated CAFM tip. The EDS mapping result indicates that Ag atoms are migrated by an external bias, which is from the Pt coated CAFM tip. Accordingly, this is a strong evidence that the resistance change between HRS to LRS is caused by the migration of Ag ions between Ag top electrodes and Pt bottom electrodes.

Generally, the resistive switching behavior with electrochemical metallization or mechanism is based on the migration of electrochemically active metals and formation of metal filaments through the insulating layer. When an external bias is applied, the Ag electrode, which is electrochemically active, is dissolved. Then, dissolved Ag cations migrate and form a conducting bridge between the Ag top and Pt bottom electrodes (Figure 81). As earlier mentioned, with reference to Figure 76, the conduction mechanism in HRS is thermally assisted by the ion hopping transport. With this thermally assisted ion hopping transport, the Ag cations migrate and reach the Pt bottom electrode, which acts as a counter electrode.[41] Thereafter, reductions in the Ag cations, which reach the bottom electrode, occurs. Therefore, the formation of the conducting bridge, which consists of Ag atoms is achieved, and the resistance of the device is changed to LRS.[48, 49] In contrast with the formation of the conducting filament, the rupture of the same filament occurs when an external bias is applied in the opposite direction.[50, 51] However, the persistently repeated formation/rupture process can cause the expansion of the conducting filament.[48] When the conducting filament grows considerably large so as to rupture with the external

bias, the device cannot become insulating, resulting to a switching failure. Thus, controlling the growth of the conducting bridge can be a key in enhancing the endurance of the resistive switching device.[52] A proposed mechanism to confine the growth of the Ag bridge is described in Figure 6. Because the non-switchable $RbPbI_3$ restrains the growth of the Ag bridge through the HP films, the Ag bridge cannot be expanded during the persistently repeated formation/rupture process. Moreover, the endurance of the devices was proportional to the concentration of $RbPbI_3$. This suggests that the non-switchable $RbPbI_3$ contributes to the enhancement of endurance.

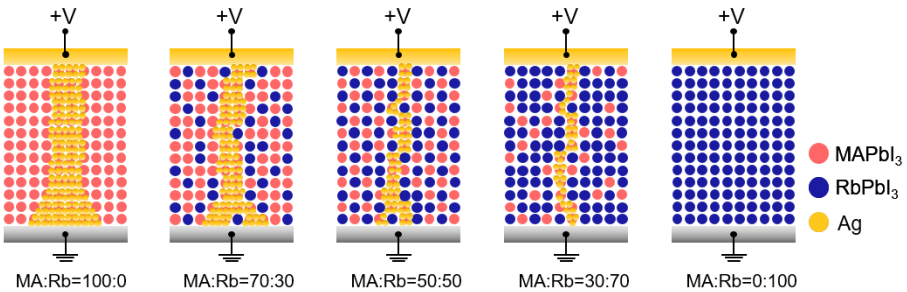

Figure 81 Schematic diagram of inhibited growth of Ag bridge with increasing the concentration of $RbPbI_3$

5.4. Conclusion

We investigated the HP-based resistive switching device with non-switchable $RbPbI_3$ mixed with switchable $MAPbI_3$ films. The memory devices fabricated with increasing $RbPbI_3$ concentrations showed to form electroforming resistive switching with three times extended endurance. It is suggested that non-switchable $RbPbI_3$ confined the growth of the Ag filament. The increase in the

concentration of $RbPbI_3$ increased the endurance of the devices and formed electroforming. According to the conduction properties at different temperatures, the thermally assisted hopping mechanism in HRS and ohmic conduction in LRS resulted from the conduction properties of the HP-based memory. Furthermore, it was observed that the migration of Ag ions contributes to the formation of the Ag bridge. However, the HP memory needs to be improved in retention time and nanoscale-level operation. Our results suggest that the HP mixture has a potential for resistive switching memory devices.

5.5. References

1. Kim, H.-S.; Lee, C.-R.; Im, J.-H.; Lee, K.-B.; Moehl, T.; Marchioro, A.; Moon, S.-J.; Humphry-Baker, R.; Yum, J.-H.; Moser, J. E., *Sci. Rep.* **2012,** *2*, 591.
2. Burschka, J.; Pellet, N.; Moon, S.-J.; Humphry-Baker, R.; Gao, P.; Nazeeruddin, M. K.; Grätzel, M., *Nature* **2013,** *499*, 316-319.
3. Liu, M.; Johnston, M. B.; Snaith, H. J., *Nature* **2013,** *501*, 395-398.
4. Kim, Y. H.; Cho, H.; Heo, J. H.; Kim, T. S.; Myoung, N.; Lee, C. L.; Im, S. H.; Lee, T. W., *Adv. Mater.* **2015,** *27*, 1248-1254.
5. Veldhuis, S. A.; Boix, P. P.; Yantara, N.; Li, M.; Sum, T. C.; Mathews, N.; Mhaisalkar, S. G., *Adv. Mater.* **2016,** *28* (32), 6804-6834.
6. Dong, Y.; Gu, Y.; Zou, Y.; Song, J.; Xu, L.; Li, J.; Xue, J.; Li, X.; Zeng, H., *Small* **2016,** *12*, 5622-5632.
7. Kwon, K. C.; Hong, K.; Van Le, Q.; Lee, S. Y.; Choi, J.; Kim, K. B.; Kim, S. Y.; Jang, H. W., *Adv. Funct. Mater.* **2016,** *26*, 4213-4222.
8. Yoo, E. J.; Lyu, M.; Yun, J. H.; Kang, C. J.; Choi, Y. J.; Wang, L., *Adv. Mater.* **2015,** *27*, 6170-6175.
9. Gu, C.; Lee, J. S., *ACS Nano* **2016,** *10*, 5413-5418.
10. Choi, J.; Park, S.; Lee, J.; Hong, K.; Kim, D. H.; Moon, C. W.; Park, G. D.; Suh, J.; Hwang, J.; Kim, S. Y.; Jung, H. S.; Park, N. G.; Han, S.; Nam, K. T.; Jang, H. W., *Adv. Mater.* **2016,** *28*, 6562-6567.
11. Kagan, C.; Mitzi, D.; Dimitrakopoulos, C., *Science* **1999,** *286* (5441), 945-947.

12. Senanayak, S. P.; Yang, B.; Thomas, T. H.; Giesbrecht, N.; Huang, W.; Gann, E.; Nair, B.; Goedel, K.; Guha, S.; Moya, X., *Sci. Adv.* **2017,** *3*, e1601935.

13. Xu, J.; Li, J.; Tang, L.; Peng, Y.; Wu, Y.; Du, Y.; Huang, L.; Ni, J.; Cai, H.; Zhang, J., *Phys. Status Solidi* **2017,** *214*, 1700170.

14. Xiao, Z.; Huang, J., *Adv. Electron. Mater.* **2016,** *2*, 1600100.

15. Xu, W.; Cho, H.; Kim, Y. H.; Kim, Y. T.; Wolf, C.; Park, C. G.; Lee, T. W., *Adv. Mater.* **2016,** *28*, 5916-5922.

16. Choi, J.; Le, Q. V.; Hong, K.; Moon, C. W.; Han, J. S.; Kwon, K. C.; Cha, P.-R.; Kwon, Y.; Kim, S. Y.; Jang, H. W., *ACS Appl. Mater. Interfaces* **2017,** *9*, 30764-30771.

17. Seo, J.-Y.; Choi, J.; Kim, H.-S.; Kim, J.; Yang, J.-M.; Cuhadar, C.; Han, J. S.; Kim, S.-J.; Lee, D.; Jang, H. W., *Nanoscale* **2017,** *9*, 15278-15285.

18. Liu, D.; Lin, Q.; Zang, Z.; Wang, M.; Wangyang, P.; Tang, X.; Zhou, M.; Hu, W., *ACS Appl. Mater. Interfaces* **2017,** *9*, 6171-6176.

19. Hwang, B.; Gu, C.; Lee, D.; Lee, J. S., *Sci. Rep.* **2017,** *7*, 43794.

20. Eperon, G. E.; Habisreutinger, S. N.; Leijtens, T.; Bruijnaers, B. J.; van Franeker, J. J.; deQuilettes, D. W.; Pathak, S.; Sutton, R. J.; Grancini, G.; Ginger, D. S., *ACS nano* **2015,** *9*, 9380-9393.

21. You, J.; Meng, L.; Song, T.-B.; Guo, T.-F.; Yang, Y. M.; Chang, W.-H.; Hong, Z.; Chen, H.; Zhou, H.; Chen, Q., *Nat. Nanotechnol.* **2016,** *11*, 75-81.

22. Lee, S.; Park, J. H.; Lee, B. R.; Jung, E. D.; Yu, J. C.; Di Nuzzo, D.; Friend, R. H.; Song, M. H., *J. Phys. Chem. Lett.* **2017,** *8* (8), 1784-1792.

23. Hwang, B.; Lee, J.-S., *Sci. Rep.* **2017,** *7*, 673.

24. Jeon, N. J.; Noh, J. H.; Kim, Y. C.; Yang, W. S.; Ryu, S.; Seok, S. I., *Nat. Mater.* **2014,** *13* (9), 897-903.

25. Xiao, M.; Huang, F.; Huang, W.; Dkhissi, Y.; Zhu, Y.; Etheridge, J.; Gray-Weale, A.; Bach, U.; Cheng, Y. B.; Spiccia, L., *Angew. Chem. Int. Ed. Engl.* **2014,** *53* (37), 9898-9903.

26. Liang, P. W.; Liao, C. Y.; Chueh, C. C.; Zuo, F.; Williams, S. T.; Xin, X. K.; Lin, J.; Jen, A. K. Y., *Adv. Mater.* **2014,** *26* (22), 3748-3754.

27. Zhang, W.; Pathak, S.; Sakai, N.; Stergiopoulos, T.; Nayak, P. K.; Noel, N. K.; Haghighirad, A. A.; Burlakov, V. M.; deQuilettes, D. W.; Sadhanala, A.; Li, W.; Wang, L.; Ginger, D. S.; Friend, R. H.; Snaith, H. J., *Nat. Commun.* **2015,** *6*, 10030.

28. Mitzi, D. B., *Prog. Inorg. Chem.* **2007,** *48*, 1-121.

29. Travis, W.; Glover, E.; Bronstein, H.; Scanlon, D.; Palgrave, R., *Chem. Sci.* **2016,** *7*, 4548-4556.

30. Meloni, S.; Moehl, T.; Tress, W.; Franckevičius, M.; Saliba, M.; Lee, Y. H.; Gao, P.; Nazeeruddin, M. K.; Zakeeruddin, S. M.; Rothlisberger, U., *Nat. Commun.* **2016,** *7*, 10334.

31. Xiao, Z.; Yuan, Y.; Shao, Y.; Wang, Q.; Dong, Q.; Bi, C.; Sharma, P.; Gruverman, A.; Huang, J., *Nat. Mater.* **2014,** *14* 193-198.

32. Young, J.; Rondinelli, J. M., *J. Phys. Chem. Lett.* **2016,** *7*, 918-922.

33. Brgoch, J.; Lehner, A. J.; Chabinyc, M.; Seshadri, R., *J. Phys. Chem. C* **2014,** *118*, 27721-27727.

34. Lim, D.-H.; Ramasamy, P.; Kwak, D.-H.; Lee, J.-S., *Nanotechnology* **2017,** *28*, 255601.

35. Jung, M.-H.; Rhim, S. H.; Moon, D., *Sol. Energy Mater. Sol. Cells* **2017,** *172*, 44-54.

36. Whitfield, P.; Herron, N.; Guise, W.; Page, K.; Cheng, Y.; Milas, I.; Crawford, M., *Sci. Rep.* **2016,** *6*, 35685.

37. Dang, Y.; Liu, Y.; Sun, Y.; Yuan, D.; Liu, X.; Lu, W.; Liu, G.; Xia, H.; Tao, X., *Cryst. Eng. Comm.* **2015,** *17*, 665-670.

38. Trots, D.; Myagkota, S., *J. Phys. Chem. Solids* **2008,** *69*, 2520-2526.

39. Goldstein, J. I.; Newbury, D. E.; Michael, J. R.; Ritchie, N. W.; Scott, J. H. J.; Joy, D. C., *Scanning electron microscopy and X-ray microanalysis*. Springer: 2017.

40. Ahn, N.; Son, D.-Y.; Jang, I.-H.; Kang, S. M.; Choi, M.; Park, N.-G., *J. Am. Chem. Soc.* **2015,** *137*, 8696-8699.

41. Waser, R.; Dittmann, R.; Staikov, G.; Szot, K., Redox-based resistive switching memories–nanoionic mechanisms, prospects, and challenges. *Adv. Mater.* **2009,** *21*, 2632-2663.

42. Tsuruoka, T.; Terabe, K.; Hasegawa, T.; Aono, M., *Nanotechnology* **2010,** *21*, 425205.

43. Gao, S.; Song, C.; Chen, C.; Zeng, F.; Pan, F., *J. Phys. Chem. C* **2012,** *116*, 17955-17959.

44. Sun, J.; Liu, Q.; Xie, H.; Wu, X.; Xu, F.; Xu, T.; Long, S.; Lv, H.; Li, Y.; Sun, L., *Appl. Phys. Lett.* **2013,** *102*, 053502.

45. Tsuruoka, T.; Terabe, K.; Hasegawa, T.; Aono, M., *Nanotechnology* **2011,** *22*, 254013.

46. Kato, Y.; Ono, L. K.; Lee, M. V.; Wang, S.; Raga, S. R.; Qi, Y., Silver iodide formation in methyl ammonium lead iodide perovskite solar cells with silver top electrodes. *Adv. Mater. Interfaces* **2015,** *2* 1500195.

47. Zhang, T.; Meng, X.; Bai, Y.; Xiao, S.; Hu, C.; Yang, Y.; Chen, H.; Yang, S., *J. Mater. Chem. A* **2017,** *5*, 1103-1111.

48. Arita, M.; Takahashi, A.; Ohno, Y.; Nakane, A.; Tsurumaki-Fukuchi, A.; Takahashi, Y., *Sci. Rep.* **2015,** *5*, 17103.

49. Takahashi, Y.; Kudo, M.; Arita, M., *ECS Trans.* **2015,** *69*, 299-309.

50. Lin, Y.-Y.; Lee, F.-M.; Chien, W.-C.; Chen, Y.-C.; Hsieh, K.-Y.; Lu, C.-Y. International Electron Devices Meeting (IEDM), 2010 IEEE International, IEEE: 2010; pp 22.2. 1-22.2. 4.

51. Chen, B.; Lu, Y.; Gao, B.; Fu, Y.; Zhang, F.; Huang, P.; Chen, Y.; Liu, L.; Liu, X.; Kang, J. International Electron Devices Meeting (IEDM), 2011 IEEE International, IEEE: 2011; pp 12.3. 1-12.3. 4.

52. Liu, Q.; Long, S.; Lv, H.; Wang, W.; Niu, J.; Huo, Z.; Chen, J.; Liu, M., *ACS nano* **2010,** *4*, 6162-6168.

Chapter 6
Summary

Quote

Antoine Laurent Lavoisier

We must trust to nothing but facts. These are presented to us by Nature, and cannot deceive. We ought, in every instance, to submit our reasoning to the test of experiment, and never to search for truth but by the natural road of experiment and observation. (1790)

This work provides a foundation for adopting HPs to resistive switching memories. I believe RS memories fabricated from these fascinating materials will be promising candidates for commercial applications in the near future with progress in device fabrication and the material itself. Further research should resolve the existing problems facing next-generation RS memories

Through the Chapter 1, historical background, which is related to the needs of memory devices for the record, sharing, and communication of human beings, is described. Also, technologies of next-generation memories to support the Information Age is introduced. To realize RS memories, the HPs with unique properties are suggested as insulating layer. The fabrication processes for HPs based devices including solution and vacuum processes halide perovskite based device are explained.

Through the Chapter 2, the first high performance $MAPbI_3$-based resistive switching memory is described. The vertical structured exhibited ultralow operation voltage of ± 0.15 V, high on/off ratio of 10^6, and four-step of multilevel resistance. To unearth the origin of ultralow operation voltage for RS behavior, DFT calculation about iodide point defect was conducted. With C-AFM results and temperature dependence of *I-V* characteristics, RS behavior is originated from the bulk conduction, not along the grain boundaries.

Through the Chapter 3, RS devices, which is based on morphologically improved $MAPbI_3$ films with hydroiodic acid as an additive, is described to enhance endurance properties. The RS device with improved MAPbI3 films exhibited the endurance of 1330 cycles. Based on the morphologically

improved films, flexible RS devices was operable under extremely low bending radius of 5 mm. *I-V* characteristics which was measured under 263, 283, 303 K revealed the conduction mechanism of Ag/$MAPbI_3$/Pt/SiO_2/Si devices is thermally assisted hopping, not space charge limited conduction.

Through the Chapter 4, the RS memory based on 2-dimensional layered HPs is described. Previous RS memory with 3-dimensional HPs exhibited cell to cell variation due to grain boundaries in the crystal structures. However, 2D HPs based RS memories showed uniform RS behavior because 2D layered HP films don't include grain boundaries. Moreover, 2D layered HPs have a stable crystal structure with respect to consistent external biases, enabling reliable RS. Based on the excellent uniformity of 2D layered HP films, RS memories, which were fabricated on a 4-inch wafer with solution processes, showed equivalent RS characteristics even the operation temperature was 87 ºC.

Through the Chapter 5, a fundamental approach is described to extend endurance properties for RS memory with conducting filament. With utilizing the mixture of non-switchable orthorhombic $RbPbI_3$ and switchable tetragonal $MAPbI_3$, the abnormal growth of the conducting filament is prevented during repeated switching. It was confirmed that the endurance was improved from 300 times to 900 times as the concentration of Rb in $Rb_{1-x}MA_xPbI_3$ films was increased. To assure long-term stability, spin coated PMMA films as a passivation layer prevent chemical reaction and formation of AgI layer between the $Rb_{1-x}MA_xPbI_3$ films and Ag top electrodes. Moreover, the PMMA films protect the $Rb_{1-x}MA_xPbI_3$ films from oxygen and water vapor.

This thesis has suggested the possibility of fabricating HP resistive switching devices, emphasizing high performance, low-cost and low-tempearture synthesis, a low power consumption, and mechanical and compositional flexibility. A wide variety of HPs can be realized with compositional flexibility, which is a major strength of HP applications. However, very few studies have addressed HP based microelectronic devices. Corresponding research in this field will have to be conducted to overcome the limitations of film preparation and stability and profoundly understand the intrinsic properties of HPs.

Acknowledgments

학위과정을 시작하기까지 많은 망설임 들이 있었습니다. 과연 제가 연구를 할 자격이 있는 사람인지, 그럴만한 그릇을 갖추고 있는지, 내가 맞지 않는 옷을 입고자 혼자 발버둥 치는 것은 아닌지에 대한 고민들이 많았습니다. 이러한 고민에도 불구하고 물심양면으로 지원해주신 부모님과 홀로 육아를 이끌어온 아내에게 감사의 말을 전하고자 합니다.

부족하기만 했던 저에게 박사가 될 수 있도록 이끌어주신 장호원 교수님께 무한한 감사의 말씀을 드립니다. 교수님과 함께하였던 5년의 시간은 저에게 잊지 못할 5년이 되었습니다. 난관에 봉착했을 때, 연구의 목표와 기본을 돌아보게 지도해주셨기에 많은 생각을 할 수 있었습니다. 수많은 실패에도 아낌없이 지원해주신 남기태 교수님과 중앙대학교 김수영 교수님께도 감사의 말씀 드립니다. 성균관대학교 박남규 교수님, 정현석 교수님, 신현정 교수님, 국민대학교 차필령 교수님, 홍익대학교 권용우 교수님, 한국에너지기술연구원 이찬우 박사님, 포항공과대학교 이장식 교수님, 이동화 교수님, 교수님들께서 계셨기에 제가 미래소재디스커버리 과제를 통해 도약할 수 있었습니다. 특히 정현석 교수님께서 말씀하셨던 연구자의 윤리는 잊지 않도록 노력하겠습니다. 감사합니다.

연구 초기, 전기적 특성 분석의 다양한 방법들을 알려주신 심영석 박사님, 처음으로 실험실 꾸리시느라 고생하신 김도홍 박사님, 갑작스러운 TEM 부탁에도 묵묵히 도와주신 전종명 박사님, 같은 유부남으로써 어려운 고민 들어주시던 홍승표 박사님, 처음에 별로 대화도 없다가도 갑작스레 기판 만들어달란 부탁에도 웃으며 만들어줬던 권기창 박사님, 장비 고장에도 언제든지 달려와 주셨던 에이엔씨테크 조동현 사장님, 덕분에 제가 여기까지 올 수 있었습니다. 감사합니다.

공동연구를 진행하며 무리한 샘플 요청에도 모두 응해주신 박승학, Le Van Quyet, 서자영, 이상명 연구원님들께도 감사의 말씀 전합니다. 여러분들이 있었기에 부족한 환경에서도 좋은 연구를 수행할 수 있었습니다. 협업을 어떻게 해 나갈지에 대해서도 배우는 과정이 되었었습니다.

이리도 못난 형을 형이라고 같이 해준 천우, 구택, 태민, 석훈, 준민, 운배, 태형, 창연, 종성이와 충원이, 함께해서 행복했다. 너희들을 만난 건 나에게 행운이었어. 특히 SEM 찍어달라고 칭얼대던 나에게 군말 없이 찍어준 천우, 데이터를 어떻게 해석해야 할지 항상 길잡이가 되어주었던 구택이, 보살 같은 석훈이 정말 고맙다. 준민이에겐 이빔 떠넘기고 가는 것 같아 한편으론 미안하다. 잘 부탁한다. 옷깃만 스쳐도 인연이라는데, 이 정도면 다들 정말 좋은 인연이 아닐까 싶다.

우리 메모리 팀 여러분, 그래도 선배라고 군말 없이 도와준 지수, 동생인데도 부담 없이 대해준 효정 누나, 도와준 것 없이 취직한다고 귀찮게만 만든 선길이, 미래소재디스커버리 라는 큰 짐을 드리고 가는 것 같아 미안한 마음이 큽니다. 제가 좀 더 잘해놨어야 하는데 그러지 못한 것 같아 마음이 계속 가네요. 제가 졸업하더라도 힘 닿는 데까지 도와드리도록 노력하겠습니다.

마지막으로 파아란 여러분들께도 감사의 말 전합니다. 뜬금없이 대학원 입학했다고 자전거 하나 끌고 와서는 같이 타자고 한 저에게 따뜻하게 맞아준 여러분들이 있어 대학원 생활도 잘 마무리 할 수 있었습니다.

사랑합니다, 여러분. 어디서든 다시 만날 날을 기다리겠습니다.

List of Publications

1. K. C. Kwon, K. Hong, Q. V. Le, S. Y. Lee, J. Choi, K.-B. Kim, S. Y. Kim, and H. W. Jang, "Inhibition of ion migration for reliable operation of organolead halide perovskite-based metal/semiconductor/metal broadband photodetectors", Advanced Functional Materials 26, 4213-4222 (2016),
2. J. Choi, S. Park, J. Lee, K. Hong, D.-H. Kim, C. W. Moon, G. D. Park, J. Suh, J. Hwang, S. Y. Kim, H. S. Jung, N.-G. Park, S. Han, K. T. Nam, and H. W. Jang, "Organolead halide perovskites for low operating voltage multilevel resistive switching", Advanced Materials 28, 6562-6567 (2016), <Co-first, front cover>
3. J. Choi, Q. V. Le, K. T. Hong, C. W. Moon, J. S. Han, K.C. Kwon, P.-R. Cha, Y. W. Kwon, S. Y. Kim, and H. W. Jang "Enhanced endurance organolead halide perovskite resistive switching memories operable under an extremely low bending radius", ACS Applied Materials & Interfaces 9, 30764-30771 (2017), <Co-first>
4. J.-Y. Seo, J. Choi, H.-S. Kim, J. Kim, J.-M. Yang, C. Cuhadar, J. S. Han, S.-J. Kim, D. Lee, H. W. Jang, and N.-G. Park " Wafer-scale reliable switching memory based on 2-dimensional layered organic-inorganic halide perovskite", Nanoscale 9, 15278-15285 (2017), <Co-first>
5. J. S. Han, Q. V. Le, J. Choi, K. Hong, C. W. Moon, T. L. Kim, H. Kim, S. Y. Kim and H. W. Jang "Air-stable cesium lead iodide perovskite

for ultra-low operating voltage resistive switching", Advanced Functional Materials 28, 1705783 (2017),

6. H. Kim, J. S. Han, J. Choi, S. Y. Kim, and H. W. Jang, “Halide perovskites for applications beyond photovoltaics”, Small Methods 2, 1700310 (2018),
7. N. Park, Y. Kwon, J. Choi, H. W. Jang, and P.-R. Cha, “Plausible carrier transport model in organic-inorganic hybrid perovskite resistive memory devices”, AIP Advances 8, 045205 (2018),
8. J. Choi, J. S. Han, K. Hong, S. Y. Kim, and H. W. Jang, “Organic-inorganic hybrid halide perovskites for memories, transistors, and artificial synapses”, Advanced Materials, accepted, <Co-first>
9. S. Lee, J. Choi, J. B. Jeon, B. J. Kim, J. S. Han, T. L. Kim, H. S. Jung, and H. W. Jang, “Enhanced conducting bridge resistive switching in mixtures of switchable tetragonal $CH_3NH_3PbI_3$ and non-switchable orthorhombic $RbPbI_3$”, Small, submitted, <Co-first>

Cover image

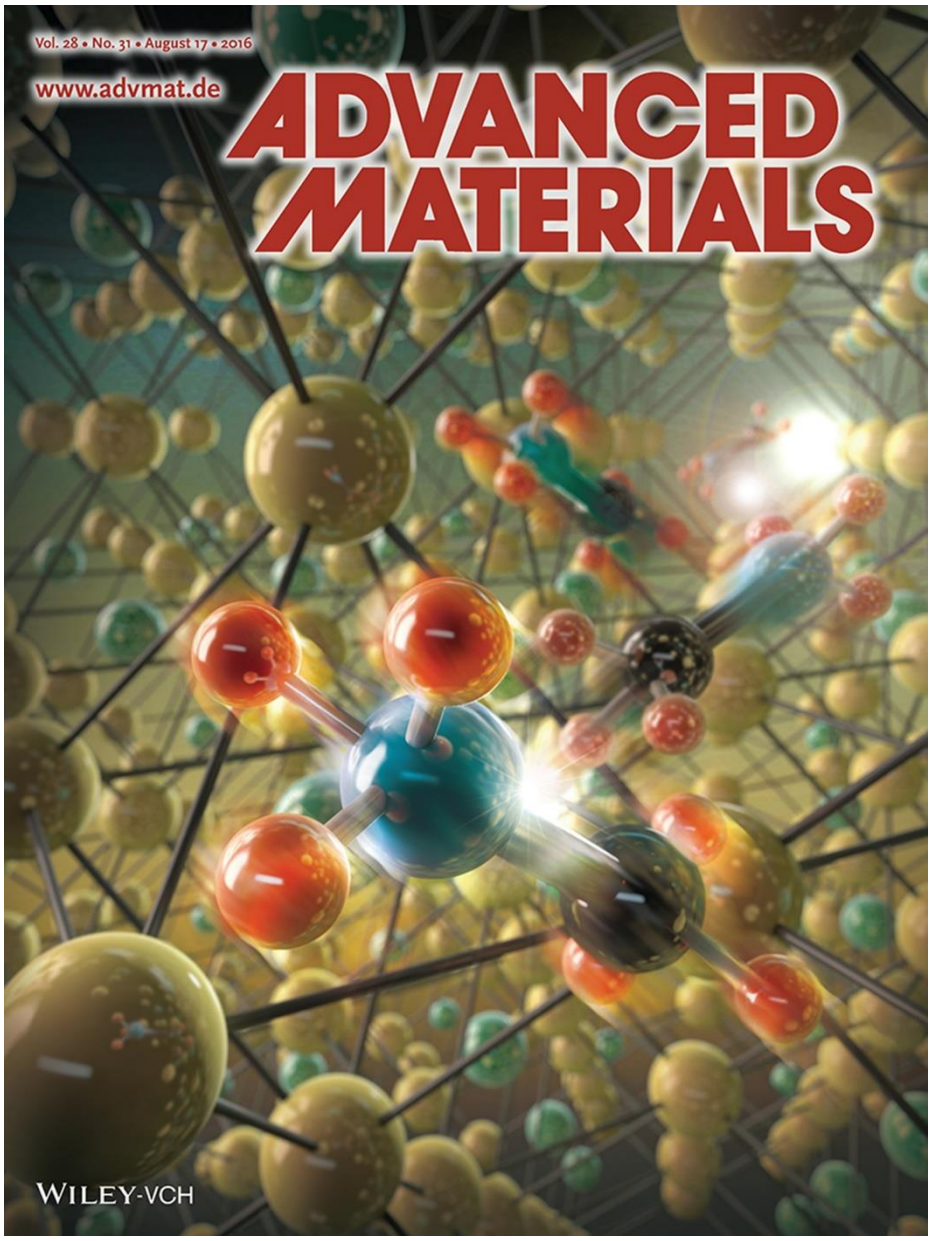

Advanced Materials 28, 6562-6567 (2016) **(16/08/01)**

Patents

1. Memory device having non-volatile resistive switching characteristics and manufactureing method thereof, 10-1687812, Korea
2. Flexible memory device having multilevel resistance switching characteristics and manufacturing method thereof, 10-1782379, Korea

Awards and honors

1. The Excellent Presentation Paper Award, Korean Institute of Electrical and Electronic Material Engineers (2016.06.23)

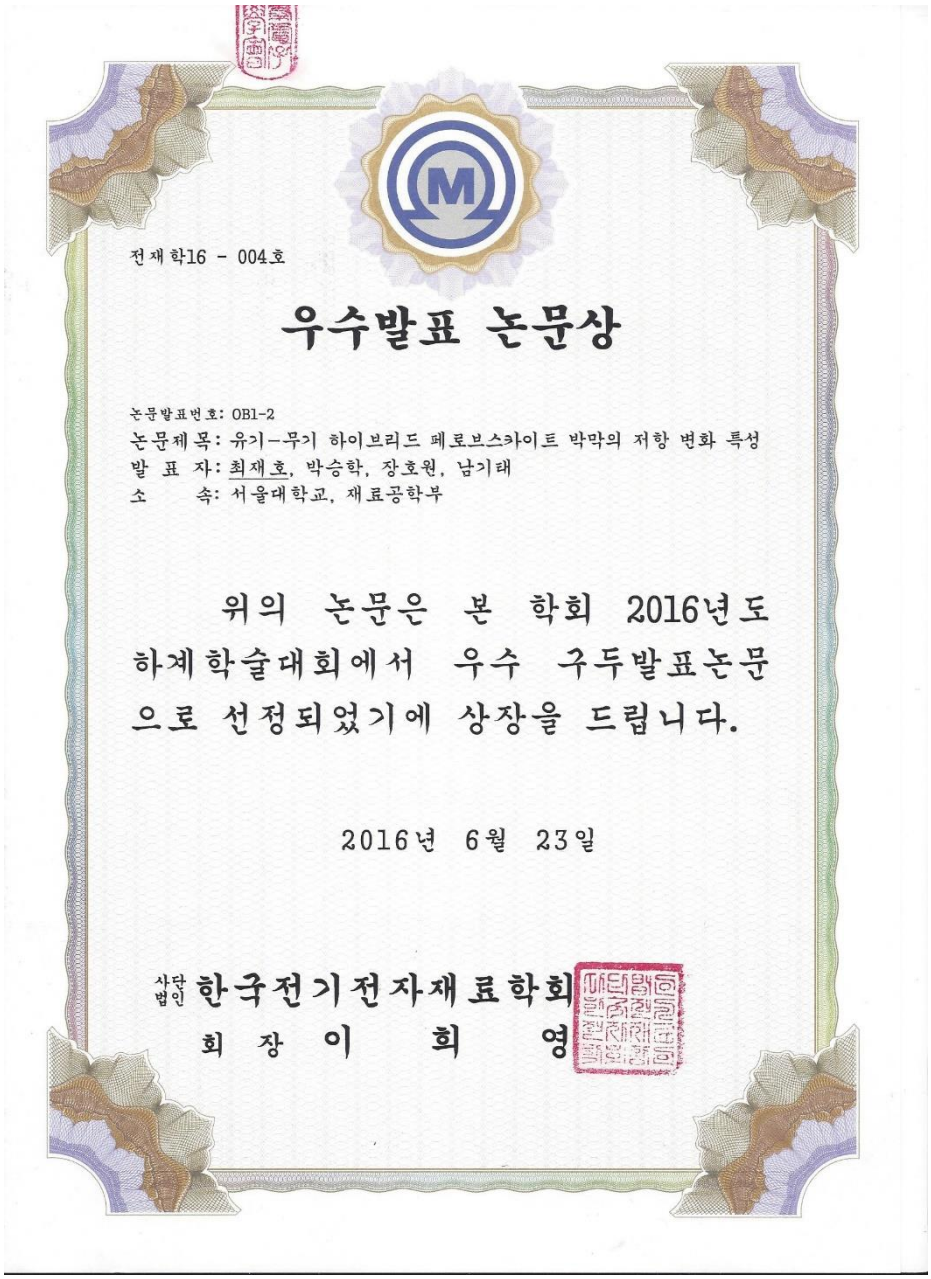

전재학16 - 004호

우수발표 논문상

논문발표번호: OB1-2
논문제목: 유기-무기 하이브리드 페로브스카이트 박막의 저항 변화 특성
발 표 자: 최재호, 박승학, 장호원, 남기태
소 속: 서울대학교, 재료공학부

위의 논문은 본 학회 2016년도 하계학술대회에서 우수 구두발표논문으로 선정되었기에 상장을 드립니다.

2016년 6월 23일

사단법인 한국전기전자재료학회
회 장 이 희 영

Participation of international conference, symposium and workshop

1. J. Choi, J. Y. Hwang, K. T. Nam, and H. W. Jang, “Nonlinear Current-Voltage Characteristics of Perovskite Alkyl Ammonium Lead Iodide”, American Chemical Society, San Francisco, U.S. (20140810) <Poster>
2. J. Choi, S. Park, K. T. Nam and H. W. Jang, “Ultralow Electric Field Resistive Switching in Organometal Halide Perovskite”, European-Materials Research Society (E-MRS) 2015, Lille, France (20150515) < Oral>
3. J. Choi, K. Hong, K. C. Kwon, S. Park, K. T. Nam and H. W. Jang, “Hybrid Organic-Inorganic Perovskite Thin Films for Nonvolatile Memory and Broadband Photodetector”, Nano Convergence Conference 2016, Seoul, Republic of Korea (201601208) <Poster>
4. J. Choi, S. Park, K. T. Nam and H. W. Jang, “Organolead Halide Perovskites for Multilevel Resistive Switching”, Smart Systems Integration (SSI) 2016, Munich, Germany (20160309) <Poster>
5. J. Choi, S. Park, K. T. Nam and H. W. Jang, “Organolead Halide Perovskites for Low Operating Voltage Multilevel Resistive Switching”, The Korean Insititute of Electrical and Electronic Material Engineers (KIEEME) 2016, Gyeongju, Republic of Korea (20160624) <Oral>
6. J. Choi, S. Park, K. T. Nam and H. W. Jang, “Organolead Halide Perovskites for Multilevel Resistive Switching”, Materials Research Society (MRS) 2016, Boston, U.S (20161027) <Poster>
7. J. Choi, S. Park, K. T. Nam and H. W. Jang, “Memristive Behavior of Organometal Halide Perovskite Thin Films”, International Conference

on Electronic Materials and Nanotechnology for Green Environment (ENGE) 2016, Jeju, Republic of Korea (20161108) <Poster>

8. J. Choi, J. S. Han, and H. W. Jang, “Ultralow Electric Field Resistive Switching in Organometal Halide Perovskites”, The Korean Insititute of Electrical and Electronic Material Engineers (KIEEME) 2017, Pyeongchang, Republic of Korea (20170622) <Oral>
9. J. Choi, S. Park, K. T. Nam, and H. W. Jang, “Memristive Behavior of Organic-Inorganic hybrid Perovskite Thin Films”, NANOKOREA (2017), Goyang, Republic of Korea (20170624) <Oral>

Curriculum vitae

Department of Materials Science and Engineering

Seoul National Univerisity

1 Gwanak-ro, Gwanak-gu, Seoul 08826,

Republic of Korea

Office: +82-2-880-7092, Cell: +82-10-3260-6717

E-mail: choijh12@snu.ac.kr

Homepage: http://onnl.snu.ac.kr

Education

Sep/2013 - Aug/2018	Ph.D. Materials Science and Engineering, Seoul National University, Republic of Korea.
Mar/2006- Aug/2013	B.S. Information Display, Kyunghee University, Republic of Korea

Research interest

- Resistive switching based on halide perovskites
- Artificial synaptic devices with halide perovskites
- Synthesis of halide perovskite
- Low temperature solution processes
- Thin film deposition with vacuum process
- Analyzing electrical properties of materials

국문초록

할라이드 페로브스카이트 박막의 저항변화 특성 분석

정보화 시대의 발전에 따라 고용량, 고성능의 저장매체의 필요성이 꾸준히 제기되어 왔으며, 이에 따라 반도체식 저장매체들은 미세공정 개선을 통해 발전해 왔다. 그러나 이는 플로팅 게이트 또는 캐패시터 내부의 임계 전자 수와 패터닝 가능한 선폭의 한계 문제를 해결하지 못하고 있으며 이를 극복하기 위한 다양한 차세대 메모리들이 제시되어 왔다. 이들 중 가장 유력한 후보로 저항변화 메모리가 두각을 나타내었으며, 금속산화물을 절연층으로 하는 저항변화 메모리가 주로 연구되어 왔다. 그러나 금속산화물 기반의 저항변화 메모리들은 절연층의 전기적 특성제어가 어렵고 진공장비를 이용하므로 제작비용이 고가이며 유연성을 부여하기 어렵다는 단점이 존재한다. 이에 기존 금속산화물 기반 저항변화 메모리들의 단점을 극복할 수 있는 할라이드 페로브스카이트 소재 기반 저항변화 메모리가 큰 가능성을 보여주고 있다. 밴드갭의 조절과 다수 운반자 (majority carrier) 제어가 용이하고

높은 이온 이동도를 보이며 기계적으로 우수한 유연성을 보이는 할라이드 페로브스카이트는 차세대 반도체 소재로 주목받고 있으며, 이에 대한 연구가 최근 활발히 진행되고 있다.

이 졸업논문은 할라이드 페로브스카이트를 이용한 저항변화 메모리의 구현 및 전기적 특성 분석, 성능향상에 대해 4 개의 챕터에서 다루고 있다. 첫 번째 챕터는 할라이드 페로브스카이트 중 가장 대표적인 3 차원 결정구조를 가지는 $CH_3NH_3PbI_3$ 박막의 저항변화 특성 및 전도특성을 분석한 내용을 담고 있다. 두 번째 챕터는 기존의 용매-반용매법을 이용한 용액공정이 아닌 첨가제를 활용하는 용액공정을 이용하여 모폴로지가 개선된 박막의 저항변화 특성 및 전도특성을 분석하였으며, 향상된 용액공정을 이용하여 5 mm 의 매우 낮은 곡률반경에서도 구동 가능한 저항변화 메모리를 구현하였다. 세 번째 챕터는 앞의 두 챕터가 $MAPbI_3$ 를 절연층으로 사용한 반면, 2 차원 결정구조를 갖는 BA_2PbI_4 와 A 사이트에 BA 및 MA 를 혼합한 유사 2 차원 구조를 갖는 화합물을 절연층으로 사용하여 스위칭 신뢰성을 향상시키는 연구를 담고 있다. 네 번째 챕터는 기존에 절연층 소재로 사용된 $MAPbI_3$ 에 스위칭이 불가능한 사방정계

구조의 $RbPbI_3$를 첨가하여 $Rb_{1-x}MA_xPbI_3$ 혼합물을 활용, 스위칭 신뢰성을 향상시키고, 절연층으로 사용된 $Rb_{1-x}MA_xPbI_3$ 박막과 상부전극 사이에 PMMA 박막을 추가하여 절연층을 외부의 산소와 수분 및 상부전극과 의도하지 않은 화학적 반응을 방지하는 연구를 담고 있다.

첫 번째 챕터에서는 고성능의 할라이드 페로브스카이트 메모리를 구현하고자 하였다. 스핀코팅 중 반용매 (antisolvent)를 주사하는 기법을 활용하여 hydrophobic 한 Pt 박막 위에 균일한 $MAPbI_3$ 박막을 형성한 뒤, Ag, Ni, Au 세 종류의 상부전극을 전자 빔 증착기를 이용하여 증착하였다. 수직구조 Ag/$MAPbI_3$/Pt 소자는 별도의 포밍 과정이 필요하지 않으며 낮은 구동전압과 높은 on/off 저항비, 이를 바탕으로 하는 4 단계의 다중 저항 스위칭이 가능하였으며, Ni, Au 상부전극에서도 일부 스위칭이 가능하였다. 그러나 350 회의 낮은 반복기록수명이 단점으로 지적되었다. $MAPbI_3$ 박막은 C-AFM 측정을 통해 결정립계를 통하지 않고 $MAPbI_3$ 결정을 통해 직접적으로 박막의 저항이 변하는 특성을 보였다. 이를 바탕으로 저항변화 특성의 근원을 찾아내기 위하여 제일원리 계산을 수행한 결과, 기존 금속산화물 대비 점결함들의 이동을 위한 에너지가 약

10 %에 불과한 것으로 나타났다. 이는 낮은 구동전압을 보이는 Ag/$MAPbI_3$/Pt 소자의 특성과 일맥상통하는 부분으로, 요오드 계열 점결함들이 높은 전기전도도를 보이는 필라멘트를 형성하기 때문인 것으로 추정된다.

두 번째 챕터에서는 앞서 사용된 용매-반용매법의 단점으로 지적된 반용매의 확산속도에 따른 $MAPbI_3$ 박막의 균일도 저하 문제를 해결하기 위하여 $MAPbI_3$ 의 전구체가 혼합된 용액에 요오드산 용액을 소량 첨가하여 균일한 결정화 및 박막화가 이루어지도록 하였다. 해당 공정으로 제작된 $MAPbI_3$ 박막은 더 작은 결정립 크기를 가지며, 크기의 편차 또한 줄어들었다. 이를 바탕으로 기존 350 회에서 1330 회로 증대된 반복 기록수명을 보였으며, 유연성을 가지는 기판 위에서도 제작이 용이하고, 5 mm 의 매우 낮은 곡률반경에서도 기존 실리콘 기판에 제작된 메모리 소자와 동등한 저항변화 및 전기적 특성을 보였다. 또한 온도별 전류-전압 특성 측정을 통해 수직구조 Ag/$MAPbI_3$/Pt/SiO_2/Si 소자는 기존의 $MAPbI_3$ 의 전도모델로 알려진 space charge-limited current 가 아닌 thermally assisted hopping 임을 확인하였다.

세 번째 챕터에서는 2 차원 층상구조를 가지는 할라이드 페로브스카이트의 일종일 BA_2PbI_4 를 이용하여 신뢰성이 향상된 저항변화 메모리를 구현하였다. 기존 3 차원 결정구조를 가지는 $MAPbI_3$ 는 수많은 결정립계가 존재하며, 결정립의 크기 편차에 따라 저항변화 현상의 불균일이 발생하였다. 그러나 결정립계를 포함하지 않는 2 차원 층상구조 할라이드 페로브스카이트는 박막 전체에서 균일한 저항변화 특성을 보였으며, 지속적인 외부 전계 인가에도 결정구조가 안정적인 특성을 보였다. 특히 주목할만한 점은, 3 차원 또는 유사 2 차원 결정구조 소재 대비 2 차원 층상구조 소재를 이용한 저항변화 메모리는 각각 250 회의 반복기록시험에서 저항변화 실패가 나타나지 않아 높은 구동 신뢰성을 보였다. 우수한 신뢰성 및 균일한 박막구조를 바탕으로 4 인치 크기의 실리콘 웨이퍼에 용액공정을 통해 저항변화 메모리를 제작하였을 때에도 $1 \times 1\ cm^2$ 의 기판에 제작된 시편과 동등한 저항변화 특성을 보였다. 또한 87 ^{o}C 의 고온 환경에서도 정상적으로 구동이 가능하여 향후 차세대 메모리의 상용화 가능성을 보여주었다.

네 번째 챕터에서는 기존 저항변화 메모리의 열화 원인으로 지적되온 반복기록 과정에서의 전도성 필라멘트의 비정상적 성장을 근본적으로 해결하고자 기존 $MAPbI_3$ 에 저항변화 특성을 보이지 않는 $RbPbI_3$ 의 혼합물을 절연층으로 사용하여 반복기록 수명을 증대시킨 메모리를 설명하였다. 특히 $RbPbI_3$ 의 혼합농도가 증가할수록 반복기록수명이 최대 3 배가량 증가하는 것을 확인하였다. 또한 상부전극과 절연층 사이에 PMMA 보호층을 추가하여 절연층을 외부의 수분과 산소로부터 보호하고, 상부전극과 절연층 사이의 화학적 반응을 예방하였다. 저항변화 현상의 근원을 분석하기 위하여 C-AFM 을 이용하여 전계를 가한 후, FE-SEM 의 EDS 맵핑을 실시한 결과, C-AFM 을 이용하여 전계를 가한 영역에서 Ag 원자들이 두드러지게 검출되었으며, 이를 바탕으로 Ag 이온의 이동에 따라 저항변화 현상이 일어남을 유추할 수 있었다. 이를 바탕으로 향후 연구될 할라이드 페로브스카이트 기반 저항변화 메모리의 신뢰성을 확보 수 있을 것으로 기대된다.

키워드: 할라이드 페로브스카이트, 3차원 결정구조, 2차원 층상구조, 용액공정, 저항변화 메모리, 플렉시블 메모리, 저항변화 메커니즘, 전도 모델, 전도성 필라멘트, 제일원리계산, 신뢰성 향상

학번: 2013-23049

최 재 호